

# **Advanced Methods for Scanning Electrochemical Microscopy**

**Dissertation**

zur Erlangung des Doktorgrades der Naturwissenschaften

(Dr. rer. nat.)

der

Naturwissenschaftlichen Fakultät II

Chemie, Physik und Mathematik

der Martin-Luther-Universität

Halle-Wittenberg

vorgelegt von

**Matthias Steimecke**

geboren am 02.12.1985 in Wernigerode

Gutachter

Prof. Dr. Michael Bron

Prof. Dr. Wolfgang Schuhmann

Datum der Verteidigung: 18. April 2018

Halle/Saale, den 01. November 2017

## Danksagung

Ich danke **Prof. Dr. Michael Bron** für das Überlassen des spannenden Themas sowie die Möglichkeit und die Unterstützung es mit vielen eigenen Ideen umzusetzen, die Ergebnisse zu diskutieren und auf nationalen und internationalen Konferenzen vorzustellen.

Des Weiteren danke ich allen Mitgliedern und ehemaligen Mitgliedern der Arbeitsgruppe, die zum Gelingen dieser Arbeit beigetragen haben. Besonderer Dank gilt **Stefan Rümmler** für die Synthese und Charakterisierung funktionalisierter Kohlenstoff-Nanoröhrchen im Rahmen seiner Masterarbeit, für die Durchführung von XPS-Untersuchungen und die inspirierenden Diskussionen zur Redox-Flow-Batterie. Ein weiterer Dank gilt **Gerda Seiffarth** für die Durchführung von Messungen am Raman-SECM-Instrument sowie für die intensiven Diskussionen zu den Nickel-Katalysatoren für die Sauerstoffentwicklung. Auch möchte ich mich bei **Annett Quetschke** für die Durchführung von ESEM-, TEM- und TG-Messungen und bei **Eik Koslowski** für XRD- und Raman-Messungen bedanken. Ich danke **Mark Hartmann** und **Titus Lindenberg** für die Diskussionen zur Redox-Flow-Batterie sowie **Nils-Frederik Schumacher** für die Durchführung verschiedener elektrochemischer Messungen. **Dr. Sabine Schimpf** danke ich für die akribische Durchsicht der Arbeit, **Roland Schlosser** für die Fertigung der *in situ* Messzelle und **Martin Duft** für deren Visualisierung. **Jenny Bienias** danke ich für die Durchführung von Porositätsuntersuchungen und **Anke Hassi** für die schnelle und immer kompetente Hilfe in allen administrativen Belangen in der Arbeitsgruppe. Insgesamt danke ich der gesamten Arbeitsgruppe für die sehr angenehme Arbeitsatmosphäre.

Ich danke auch **Diana Becher** vom Institut für Geologie der Universität für die Durchführung der ICP-OES-Untersuchungen.

Bei einigen Mitgliedern der Fraunhofer Institute in Halle möchte ich mich ebenfalls bedanken, vor allem **Stefan Ackermann**, **Christian Morig** und **Dr. Uwe Spohn** für die Zusammenarbeit und die kritischen Diskussionen bei den Untersuchungen zum elektrochemischen Antifouling sowie **Ulrike Hirsch** und **Dr. Michael Krause** für die Durchführung von XPS-Untersuchungen.

Nicht zuletzt möchte ich mich bei meinen Freunden und meiner Familie bedanken, vor allem bei meiner Frau Anne und meiner Tochter sowie meinen Eltern und Schwiegereltern, die mich alle immer voll unterstützt haben. Ein ganz besonderer Dank gilt meinem Vater für seine fachlichen Ratschläge, Anregungen und Diskussionen.

## **Eigenständigkeitserklärung**

Ich bestätige, dass ich die vorliegende Arbeit selbstständig und ohne fremde Hilfe verfasst und sie nur unter Verwendung der angegebenen Quellen und Hilfsmittel angefertigt habe. Wörtlich oder inhaltlich Übernahmen aus den benutzten Werken sind als solche kenntlich gemacht. Diese Arbeit wurde bisher an keiner anderen Universität vorgelegt.

Halle/Saale, den 01.11.2017

## Curriculum vitae

### **MATTHIAS STEIMECKE**

geb. 02.12.1985 in Wernigerode

verheiratet, 1 Tochter

### **Ausbildung**

---

- 12/2011 – heute      **Martin-Luther-Universität Halle-Wittenberg**
- Promotionsstudium bei Michael Bron zum Thema:  
Methodenentwicklung für die elektrochemische Rastermikroskopie (SECM)
- 10/2006 – 11/2011      **Martin-Luther-Universität Halle-Wittenberg**  
11/2011
- Master of Science (M.Sc.)
    - Masterarbeit bei Michael Bron mit dem Titel:  
Untersuchungen zu Kohlenstoffnanoröhrchen-Metalloxid-Kompositen als  
Trägermaterialien in PEM-Brennstoffzellen-Katalysatoren
  - Masterstudium, Chemie 120 LP
    - Vertiefung: Technische Chemie erneuerbarer Energien
- 07/2009
- Bachelor of Science (B.Sc.)
    - Bachelorarbeit bei Carsten Tschierske mit dem Titel:  
Darstellung eines flüssigkristallinen Materials
  - Bachelorstudium, Chemie 180 LP
    - Vertiefung: Organische Chemie, Flüssigkristalle
- 06/2005
- Gerhart-Hauptmann-Gymnasium, Wernigerode**
- Abitur

### **Stipendien und Preise**

---

- 04/2018      **Metrohm Young Chemist Award 2018**
- 07/2012 – 07/2013      **DECHEMA – Max-Buchner-Stipendium**
- Thema: Schwefelreiche Übergangsmetallkomplexe für die Sauerstoffreduktion
- 11/2008 – 09/2011      **Stiftung der Deutschen Wirtschaft (SDW) – Studienförderung**
- Grundförderung
-

## Publikationen

***In situ* characterization of Ni and Ni/Fe thin film electrodes for oxygen evolution in alkaline media by a Raman-coupled scanning electrochemical microscope setup**

M. Steimecke, G. Seiffarth, M. Bron, Analytical chemistry **2017**, 89, 10679-10686.

**A complementary Raman and SECM study on electrically conductive coatings based on graphite sol-gel composite electrodes for the electrochemical antifouling**

S. Ackermann, M. Steimecke, C. Morig, U. Spohn, M. Bron, Journal of Electroanalytical Chemistry **2017**, 795, 68-74.

**A comparative study of functionalized high-purity carbon nanotubes towards the V(IV)/V(V) redox reaction using cyclic voltammetry and scanning electrochemical microscopy**

M. Steimecke, S. Rümmler, N.-F. Schuhmacher, T. Lindenberg, M. Hartmann, M. Bron, Electroanalysis **2017**, 29, 1056-1061.

**Mixed transition metal oxide supported on nitrogen doped carbon nanotubes – a simple bifunctional electrocatalyst studied with scanning electrochemical microscopy**

G. Seiffarth, M. Steimecke, T. Walther, M. Kühhirt, S. Rümmler, M. Bron, Electroanalysis **2016**, 28, 2335-2345.

**Spin-coating and characterization of multiferroic MFe<sub>2</sub>O<sub>4</sub> (M=Co, Ni) / BaTiO<sub>3</sub> bilayers**

N. Quandt, R. Roth, F. Syrowatka, M. Steimecke, S. G. Ebbinghaus, Journal of Solid State Chemistry **2016**, 233, 82-89.

**A linear sweep voltammetric procedure applied to scanning electrochemical microscopy for the characterization of carbon materials towards the vanadium(IV)/(V) redox system**

M. Steimecke, S. Rümmler, M. Kühhirt, M. Bron, ChemElectroChem **2016**, 2, 318-322.

**BaTiO<sub>3</sub>-CoFe<sub>2</sub>O<sub>4</sub>-BaTiO<sub>3</sub> trilayer composite thin films prepared by chemical solution deposition**

T. Walther, N. Quandt, R. Köferstein, R. Roth, M. Steimecke, S. G. Ebbinghaus, Journal of the European Ceramic Society **2016**, 3, 559-565.

**The effect of rapid functionalization on the structural and electrochemical properties of high-purity carbon nanotubes**

M. Steimecke, S. Rümmler, M. Bron, Electrochimica Acta **2015**, 163, 1-8.

## Konferenzbeiträge

- 08/2017      **9. SECM-Workshop, Warschau, PL**
- Vortrag:  
*In situ* characterization of Ni and Ni/Fe thin film electrodes for the oxygen evolution reaction in alkaline media using a Raman-coupled scanning electrochemical microscope
- 08/2016      **Jahrestreffen der Internationalen Gesellschaft für Elektrochemie (ISE), Den Haag, NL**
- Vortrag:  
Scanning electrochemical microscopy (SECM) as versatile tool for evaluation of carbon-based materials employed in all-vanadium redox flow batteries
- 03/2016      **Vernetzungstreffen „Redox-Flow“, DECHEMA, Frankfurt**
- Vortrag  
Vom Aktivmaterial zur Batterie – Methodenvielfalt der elektrochemischen Charakterisierung
- 03/2015      **Jahrestreffen Deutscher Katalytiker, Weimar**
- Posterbeitrag:  
Raman-coupled scanning electrochemical microscopy
- 03/2014      **556. Wilhelm und Else Heraeus Seminar: Analytische Tools für Brennstoffzellen und Batterien, Bad Honnef**
- Posterbeitrag:  
Raman-coupled scanning electrochemical microscopy
- 05/2013      **Materials for Energy, KIT Karlsruhe**
- Posterbeitrag:  
Modification of Carbon Materials as Supports in Electrocatalysis
- 03/2012      **Jahrestreffen Deutscher Katalytiker, Weimar**
- Posterbeitrag:  
Neue nanostrukturierte Materialien für die Elektrokatalyse

## Vorbemerkungen

Die vorliegende Arbeit wurde von Dezember 2011 bis Oktober 2017 am Lehrstuhl Technische Chemie erneuerbarer Energien des Instituts für Chemie der Martin-Luther-Universität Halle-Wittenberg angefertigt. Sie ist kumulativ gestaltet und fasst fünf einzelne Arbeiten, die als Zeitschriftenartikel erschienen sind, zusammen. Der im ersten Kapitel zusammengetragene Überblick zur elektrochemischen Rastermikroskopie erhebt keinen Anspruch auf Vollständigkeit, sondern stellt vielmehr knapp die relevantesten Arbeiten und Fragestellungen auf dem Gebiet heraus. An diesen Teil schließen sich die Aufgabenstellung sowie eine Zusammenfassung aller Ergebnisse und ein Ausblick an. Die Kapitel vier bis acht beinhalten die Manuskripte der fünf Zeitschriftenartikel.

Alle Abkürzungen sind an der ersten Stelle ihres Erscheinens erklärt, an geeigneten Positionen auch ein weiteres Mal. Die uneinheitliche Strukturierung der Kapitel sowie Abweichungen in der Formatierung resultiert aus den unterschiedlichen Vorgaben der Zeitschriften.

Aus aktuellem Anlass sei darauf verwiesen, dass sich angeführte Literaturzitate in den meisten Fällen auf Aussagen und Fakten an der jeweiligen Stelle beziehen, sie können sich aber auch in einigen Fällen auf vorherige und/oder später folgende Aussagen und Fakten im Text beziehen. Wortwörtliche Übernahmen sind als solche kenntlich gemacht.

## Kurzdarstellung

Seit ihrer ersten Beschreibung 1989 hat die elektrochemische Rastermikroskopie (SECM) sich zu einer der am vielfältig einsetzbarsten Rastersondentechniken überhaupt entwickelt. Neben ihrer Anwendung zur Oberflächendarstellung, die einen direkten Vergleich von einzelnen aktiven Regionen, Punkten oder kombinatorischen Materialbibliotheken erlaubt, ist sie besonders zur Untersuchung von Kinetiken, Reaktionspfaden und Oberflächenadsorbaten in der Elektrochemie geeignet. Darüber hinaus können SECM-Experimente so durchgeführt werden, dass die gewählten Bedingungen denen der eigentlichen elektrochemischen Wandler sehr ähnlich sind.

Ziel dieser Arbeit war die Entwicklung neuartiger SECM-Experimente, die zur Charakterisierung von Elektrodenmaterialien für unterschiedliche elektrochemische Umwandlungsprozesse verwendet werden können. Dazu wurde ein erweitertes spektro-elektrochemisches Setup aufgebaut, das SECM mit einer aussagekräftigen, ortsauflösenden Spektroskopiemethode, der Raman-Mikroskopie, kombiniert ohne die SECM-Geometrie zu verändern. Raman-Untersuchungen können parallel zum elektrochemischen Experiment von der Rückseite einer Transparentelektrode mittels eines inversen Mikroskops durchgeführt werden. In einer ersten grundlegenden Untersuchung wird das Instrument zur Untersuchung von Nickel- und Nickel/Eisen-Elektroden verwendet, die von besonderem Interesse für die Sauerstoffentwicklungsreaktion (OER), dem wichtigeren Teil der elektrochemischen Wasserspaltung, sind. Der tatsächliche Beginn der Sauerstoffentwicklung kann mittels SECM bestimmt werden, während *in situ* Raman-Untersuchungen die Entwicklung der  $\gamma$ -NiOOH Phase bei allen Proben zeigen.

Im zweiten Teil der Arbeit ist gezeigt, wie SECM und Raman-Mikroskopie als individuelle Techniken eingesetzt werden, um Elektroden für das elektrochemische Antifouling durch ortsauflösende Detektion von Molekülen und der Analyse von Komponentenverteilungen komplementär zu charakterisieren.

Die Charakterisierung Kohlenstoff-basierter Elektroden für den Einsatz in Vanadium Redox-Flow-Batterien unter Verwendung der SECM-Technik ist das Thema des dritten Teils dieser Arbeit. Dafür wurde eine Methode entwickelt, die den kompetitiven SECM-Modus nutzt, und an relevanten Kohlenstoffmaterialien überprüft. Schließlich wurde diese Methode verwendet, um hoch reine Kohlenstoff-Nanoröhrchen mit wohldefinierten Mengen sauerstoffhaltiger Oberflächengruppen auf die Fähigkeit  $\text{VO}_2^+$  zu  $\text{VO}^{2+}$  umzusetzen zu untersuchen. Im Ergebnis konnte kein Einfluss der Oberflächengruppen auf die elektrochemische Reaktion gefunden werden.



## Abstract

Since its publication in 1989, Scanning Electrochemical Microscopy (SECM) has become one of the most versatile scanning probe techniques at all. Beside its applicability for surface imaging which allows a direct comparison of individual active areas, spots or combinatorial material libraries, it is highly suited for the study of kinetics, reaction pathways and surface adsorbates in electrochemistry. Furthermore, SECM experiments can be designed in a way that the chosen conditions become quite similar to those in the real electrochemical converter device.

Designing new types of SECM experiments which can be used to characterize electrode materials for different kinds of electrochemical conversion processes was the scope of this thesis. For this purpose, an advanced spectroelectrochemical setup was built up which combines SECM with a powerful spatially resolving spectroscopic technique, namely Raman microscopy, without changing the SECM geometry. Raman probing is realized in parallel to the electrochemical experiment by an inverted microscope from the backside of a transparent electrode. In a first fundamental study this instrument is applied to nickel and nickel/iron thin film electrodes which are of particular interest for the oxygen evolution reaction (OER), the more important part of the electrochemical water splitting reaction. The apparent beginning of the oxygen evolution can be determined by SECM, whereas *in situ* Raman probing at the same time shows the development of the  $\gamma$ -NiOOH phase in all samples.

In the second part of the thesis, it is demonstrated how SECM and Raman microscopy can be used as individual techniques to complementarily characterize electrodes for the electrochemical antifouling by spatially resolved detection of active molecules and component distribution analysis.

Characterization of carbon-based electrodes to be used in all-vanadium redox flow batteries (VRFB) applying SECM is the topic of the third part of this thesis. A method using the competitive mode of SECM was developed and applied to relevant carbon materials. Finally, the method was used to study high-purity carbon nanotubes with well-defined amounts of oxygen-containing surface groups on their ability to convert  $\text{VO}_2^+$  to  $\text{VO}^{2+}$ . As a result, no influence of the surface groups on the electrochemical reaction was found.

## Table of contents

<b>1</b>	<b>Introduction and basic concepts</b> .....	4
1.1	State of technology in scanning electrochemical microscopy.....	6
1.1.1	Basic principles of scanning probe techniques.....	6
1.1.2	Instrumentation and electrodes.....	9
1.1.3	Common working modes.....	12
1.2	Advanced spectroscopic methods coupled to SECM.....	16
1.3	SECM in electrochemical research.....	18
1.3.1	Advantages and opportunities.....	18
1.3.2	Oxygen reduction and evolution reaction.....	19
1.3.3	Chlorine evolution reaction.....	24
1.4	Basic aspects of material characterization for all-vanadium redox flow batteries.....	26
1.5	References.....	31
<b>2</b>	<b>Scope of the thesis</b> .....	35
<b>3</b>	<b>Summary and outlook</b> .....	36
<b>4</b>	<b>A Raman-coupled scanning electrochemical microscope setup</b> .....	41
4.1	Introduction.....	42
4.2	Experimental section.....	45
4.2.1	Chemicals and materials.....	45
4.2.2	Preparation of Ni and Ni/Fe thin film electrodes and metal analysis.....	45
4.2.3	Scanning electron microscopy.....	46
4.2.4	Raman-SECM instrumentation.....	46
4.2.5	Electrochemical and spectroelectrochemical experiments.....	46
4.3	Results and discussion.....	49
4.3.1	System design.....	49
4.3.2	Ni and Ni/Fe thin film electrodes for the oxygen evolution reaction.....	50
4.4	Conclusion.....	57
4.5	References.....	58
4.6	Supporting information.....	60

<b>5</b>	<b>Raman microscopy and SECM as complementary techniques</b> .....	64
5.1	Introduction .....	65
5.2	Experimental .....	69
5.2.1	Preparation of the conductive coating samples .....	69
5.2.2	Determination of conductivity.....	69
5.2.3	Scanning electrochemical microscopy .....	70
5.2.4	Raman spectroscopy.....	71
5.3	Results and discussion.....	72
5.3.1	Specific conductivity and local conductivity.....	72
5.3.2	Comparison of the electrochemical topography and Raman microscopy .....	74
5.3.3	Correlating surface conductivity and electrocatalytic activity .....	76
5.4	Conclusion.....	78
5.5	References .....	80
<b>6</b>	<b>SECM for the characterization of carbon materials</b> .....	82
6.1	Introduction .....	83
6.2	Results and discussion.....	85
6.3	Conclusion.....	90
6.4	Experimental Section .....	91
6.4.1	Preparation of catalyst suspension.....	91
6.4.2	Electrochemical experiments.....	91
6.4.3	Scanning electrochemical microscopy .....	91
6.5	References .....	93
<b>7</b>	<b>Microwave-assisted functionalization of high-purity carbon nanotubes</b> .....	94
7.1	Introduction .....	95
7.2	Experimental .....	97
7.2.1	CNT functionalization .....	97
7.2.2	Physical characterization.....	97
7.3	Results and discussion.....	100
7.3.1	Comparison of different oxidation agents .....	100
7.3.2	Time and concentration dependence of nitric acid treatment.....	109
7.4	Conclusion.....	112
7.5	References .....	113

<b>8</b>	<b>SECM investigation of carbon nanotubes for the application in redox flow batteries .....</b>	<b>115</b>
8.1	Introduction .....	116
8.2	Experimental .....	118
8.2.1	Sample preparation.....	118
8.2.2	X-ray photoelectron spectroscopy .....	118
8.2.3	Electrochemical characterization.....	118
8.3	Results and discussion.....	120
8.4	Conclusion.....	125
8.5	References .....	126

## 1 Introduction and basic concepts

The growing global population and the increasing energy demand which are two sides of the same coin can be considered as one of the most important challenges of the 21<sup>th</sup> century. In particular, electrical energy which is mainly produced from fossil resources such as coal, oil and gas until today demands for new ways of supply. Beside the finite nature of fossil resources, its contribution to the CO<sub>2</sub> emission and related with it the global warming is undeniable. The results of the anthropogenic greenhouse effect can be found in various climate events all over the world such as heavy rainfall from El Niño in South America or extreme droughts in Africa. To counteract this development and to limit the global warming to an acceptable level (2 °C in 2050), it is necessary to significantly reduce the overall CO<sub>2</sub> emission by changing to renewable energy sources which can be realized by different technological approaches.

Wind turbines, photovoltaic (PV) systems and hydro power plants turned out to be the most promising candidates to fulfill all requirements. However, not all of them can be installed at any place. Hydro power is strictly connected to geological requirements which can only be found at certain regions in the world. In contrast, wind turbines and PV systems can be installed nearly anywhere although there are some preferable places such as off-shore wind parks at sea or solar panels on the roof of housings or integrated solutions in facades.

Germany has taken the role of a leader in the field of renewable energies with the aim of a full turnaround in energy policy. In 2015, more than 30 % of electrical energy were renewably generated mainly by wind and solar. But this great achievement is accompanied by new challenges. As wind and sun cannot provide energy continuously, electricity providers have to find ways how to ensure the supply even in a windless night. The electricity grid is a balance between electricity input and usage where the usage can be predicted with sufficient precision. To stabilize the electrical grid, load leveling is necessary which is typically realized by gas turbine plants that can increase or decrease their power output relatively fast. In future, when the amount of energy from renewable sources increases as expected for the turnaround of energy policy in Germany in some years, new types of storage and supply systems will be needed.

A promising way to solve this issue could be the reversible conversion of electrical to chemical energy. This process can be realized by various types of electrochemical devices. Secondary batteries form one group of conversion and storage devices realized via different technological solutions. Much attention is paid to the lithium ion battery that can be used as high-density

energy storage due to the low molecular mass and the high standard potential of lithium and has already become a state-of-the-art system for electronic devices and automotive applications. In this system the energy is stored in the electrodes where at the negative pole lithium metal is intercalated into a graphite structure during charging. At the positive pole a broad variety of redox systems are possible, such as lithium cobalt(III) oxide or manganese dioxide. Many researchers all over the world focus on developing new materials for electrodes, separators, (solid) electrolytes or solvents for this battery system to improve energy and power density, lifetime of the cells and costs of components. Another type of secondary batteries are redox flow systems where the energy is stored in molecules converted at the electrodes of an electrochemical cell and pumped into storage reservoirs. Redox flow batteries are discussed for stationary storage only due to their low energy density. Nevertheless, high energy efficiency and long lifetime make them interesting, in particular, for large storage facilities. The all-vanadium redox flow battery is the most promising system in this field and has also been commercialized by several companies yet.

The combination of water electrolyzers and fuel cell devices can be regarded as a further electrochemical storage system. Here, the energy is stored in the smallest molecule we know, hydrogen which can be compressed or liquefied and stored in tanks or transported in pipelines. Due to the high energy density of compressed or liquefied hydrogen, it can be used for automotive applications using fuel cells as well where many technological aspects are in common with battery vehicles, such as the electric engine. In contrast to the above-mentioned storage systems hydrogen as a basic chemical can also be used in various applications in chemical industry such as ammonia synthesis or hydrogenation reactions. Furthermore, it can be used for carbon capture by converting it together with CO<sub>2</sub> to methane as in case of power-to-gas systems. Methane, which is the main component of natural gas, is another important storage molecule which already today possesses an important storage infrastructure of pipelines, tanks and cavern storages as well as automotive application in combustion engines.

In conclusion, there are lots of possibilities for reversible energy storage by electrochemical converters that all have different advantages and disadvantages. It also seems to be clear that it will not be a single technology which will solve all future challenges. Finally, these technologies will help to promote renewable energies and can contribute to a sustainable energy usage in future.

## **1.1 State of technology in scanning electrochemical microscopy**

In order to satisfy the increasing worldwide electricity demand in the next decades the necessity to develop powerful devices for storage and conversion becomes clear. For this it is highly important to find suitable materials which can be used as electrocatalysts in the converter systems. These materials must be characterized with regard to three main parameters: activity, stability and selectivity. For this purpose, meaningful characterization techniques are necessary which analyze the materials under *ex situ*, *operand* or, in the best case, under *in situ* conditions. The results can contribute to understand structure-property relations which are necessary to optimize synthesis routs and to finally created materials with improved parameters. A deeper understanding of structure-property relations and the related electrochemical processes, which include adsorption/desorption steps, electron transfer and diffusion effects, can be provided by various techniques, not only on a macroscopic but also on a sub-micrometer or even atomic scale.

Scanning probe techniques are valuable tools that can help to enhance the understanding of processes and structures in mater to finally create tailored materials for energy storage and conversion purpose. This section shortly introduces the group of scanning probe techniques and their basic principles and highlights, for which kind of scientific questions scanning electrochemical microscopy can be employed. Furthermore, electrodes, instrumentations and basic working modes of SECM are explained.

### **1.1.1 Basic principles of scanning probe techniques**

Scanning probe microscopic techniques (SPM) comprise a large group of stand-alone methods which have relevant physical principles in common. In all cases, the interaction between a probe and a surface is used to obtain lateral-resolved information. The probe is in most cases significantly smaller than the probed surface and its size determines the achievable resolution which can be in the range of hundreds of micrometers down to several picometers. After bringing the probe to an appropriate working distance or in contact with the surface, it is moved laterally along the surface by motor or piezo actuators. The probe response is recorded in dependence of its position and can in the following be processed to an image. In many cases, scanning probe techniques are used as imaging technique which helps to study materials, to understand effects but also to visualize. However, advantages and disadvantages, instrumental

realization and information provided by the individual methods are drastically diverging. The most prominent techniques are discussed in the following.

The invention of scanning tunneling microscopy (STM) by Binnig and Rohrer in 1982 marks the very beginning of the development of all these techniques.<sup>[1]</sup> In STM, a sharp metallic needle with a tip of several atoms is lowered down to a conductive surface until a tunnel current is observed. The working distance is typically  $< 1$  nm and the height of the probe can be controlled by the tunnel current. With this technique, a single atom resolution is achievable; however, it is absolutely vital that the surface is conductive. This main disadvantage was overcome by the development of the (scanning) force microscopy by Binnig, Quate, and Gerber in 1986 which is better known as atomic force microscopy (AFM).<sup>[2]</sup> Here, the attractive and repulsive interactions between the probe and a conductive or non-conductive surface are used for characterization. The tip is mounted on a cantilever which works as a force sensor and can provide resolution below a single atom.

SPM comprises numerous methods where a large variety of interactions is used to probe the surface. When a tip with magnetic moment is used as probe, the technique is called magnetic force microscopy (MFM) which can also be seen as a special type of AFM as magnetic forces cause the interaction. Some of these techniques use conventional STM probes and measure the capacitance (SCM), the electric potential (SPotM), the influence of incoming light from laser (L-STM) or emitted radiation (STM-iP). Other tips equipped with an aperture can be used for scanning near-field optical microscopy (SNOM), photo electron microscopy with scanning aperture (PEMSA) or ion conductance microscopy (SICM).

Electrode surfaces and the study of electrochemical reactions also came into the focus of surface probing and imaging. This became particularly obvious when several STM *ex situ* studies of electrochemically treated electrodes were published<sup>[3]</sup> as metallic electrodes were highly suitable for this technique. The very first high resolution images from STM in electrolyte solution as *in situ* technique was shown by Sonnenfeld and Hansma who studied the deposition of gold on a graphite surface without removing the electrolyte.<sup>[4]</sup> In order to avoid unwanted electrochemical reactions, e.g. dissolution at the STM tip or the sample surface, the potentiostatic STM was developed by several groups which allows applying a constant potential at tip and/or surface versus an additional reference electrode.<sup>[5]</sup> This technique, called electrochemical scanning tunneling microscopy (EC-STM), remained important especially in the field of metal corrosion science.<sup>[6]</sup> Nevertheless, it was still the tunneling of electrons that



was used for imaging and not an electrochemical process. In parallel to the development of EC-STM, there was the work of Engstrom and coworkers who concentrated on understanding the processes at micrometer-sized metal electrodes and its interaction with large electrodes.<sup>[7]</sup> They found out that the observed faradic currents which were avoided in EC-STM can be used independently to characterize processes at a microelectrode as well as interaction with another surface. Finally, Bard as well as Engstrom presented a scanning electrochemical microscope (SECM) in 1989 which uses electrochemical reactions for surface probing and imaging.<sup>[8]</sup> In contrast to the other abovementioned scanning probe techniques, SECM used relatively large probes in the beginning. The metal diameter of the microelectrodes was magnitudes larger than the probes used in STM or AFM. However, the preparation of these defined large probes was highly reproducible<sup>[9]</sup> and its use also simplifies the instrumentation as well as the requirements for damping and enables modeling of the observed electrochemical processes. Additionally, know-how from electrochemistry at large electrodes could be transferred and new types of experiments were designed. It could be shown very rapidly which broad variety of research fields SECM technique can be applied to.<sup>[10]</sup> This variety of it becomes also clear looking at the number of electrochemical methods that were transferred from macroscopic to micrometer sized electrodes. SECM can be considered as a true chemical microscopy, where an electrochemical reaction at a nano- or microelectrode is used to obtain laterally resolved information from the surface in close distance.

As mentioned in the beginning, all SPM techniques have several issues in common, thus it is not surprising that instrumental aspects from different techniques as well as tips and preparation methods were exchanged or combined. In the following, some technological developments of SECM will be highlighted. One major problem of SECM was the necessity of relatively flat samples because most experiments were performed in constant height mode with height adjustment by an approach curve. In 2000, Hengstenberg *et al.* suggested a shearforce-based system for a constant distance mode of SECM. For this purpose, the SECM tip is vibrated resulting in a frequency spectrum with different resonance frequencies. Applying one of these frequencies (usually the one with the highest resonance amplitude), the tip is lowered to a substrate which damps the amplitude. This effect is caused by shearforce interactions and allows a reproducible repositioning of the microelectrode by monitoring the amplitude without influencing the current signal. Additionally the data from repositioning results in complementary topographic information.<sup>[11]</sup> Another major development was the integration of an microelectrode in an AFM cantilever by Kranz *et al.* This even allowed an probing of surface

topography and electrochemical information in parallel.<sup>[12]</sup> Another possibility was shown by the combination of an electrochemical tunneling microscope (EC-STM) and a scanning electrochemical microscope (SECM) where both data sets were obtained by the same tip in a subsequent experiment.<sup>[13]</sup>

In a more recent work, the group of Unwin showed that it is also possible to integrate the whole electrochemical cell into a multichannel glass pipette equipped with reference electrodes which serves as tip. In this case, the sample can be used as working electrode. This technique is named as scanning electrochemical cell microcopy (SECCM)<sup>[14]</sup> and can be used for high-speed electrochemical imaging.<sup>[15]</sup>

From this broad variety of technological improvements one can understand why SECM is a versatile technique which is applied to many research fields. Energy materials, corrosion processes, surface modification as well as biological systems, enzymes, living cells and all kinds of reaction kinetics were analyzed with this spatially resolving technique. The broad applicability explains why SECM has developed into one of the most important SPM techniques.

### **1.1.2 Instrumentation and electrodes**

The instrumentation which is used for SECM experiments can be divided into two parts: On the one hand the electrochemical equipment with potentiostat, reference, counter and working electrode (microelectrode), and on the other, the positioning system which is required for the microelectrode positioning. For electrochemical experiments, a three-electrode setup is used containing all the mentioned electrodes. The potentiostat is an electronic device which adjusts the potential of a working electrode relatively to a reference electrode where at the same time the current between working and counter electrode is measured. This setup using a reference electrode is necessary as potential and current cannot be measured independently, due to Ohm's law. Additionally, the reference electrode provides an exactly defined potential which allows for comparison of different measurements. Today's potentiostats can also work in a galvanostatic mode where the current is applied and the resulting potential measured. In SECM, the electrochemical setup is often extended by another working electrode, which is typically the substrate under investigation, to a four-electrode setup. In this case, a bi-potentiostat is necessary. However, for various experiments it is sufficient to use a three-electrode setup. For potentiometric SECM, actually a two-electrode setup is enough.

As in other SPM techniques, the preparation of the tip, in this case an (ultra)microelectrode<sup>1</sup>, is of particular importance. Standard disk-shaped microelectrodes<sup>[9]</sup> are prepared by bringing a short metal wire into the middle of a pulled glass capillary. A capillary is molten by a heat source and the ends are pulled outwardly. This procedure can be realized by a commercial laser puller system. Then, the metal wire is inserted and sealed by another heating. This leads to a homogeneous enclosing of the metal wire by the molten glass. The parameters during the pulling procedure decide upon the features of the microelectrode. The wire can later be contacted by a copper wire and conductive epoxy resin from the open end of the capillary. In commercially available microelectrodes, mainly platinum and gold are used as they have a similar expansion coefficient as glass. Not all metals can be used for the process described above. Accordingly, there is a broad variety of different preparation methods for numerous types of microelectrodes. An easy method is the deposition of the desired metal on a platinum microelectrode. Another possibility is the leaching of the wire metal of a microelectrode (e.g. via oxidation) leaving a cavity that can be filled by the material of interest. Carbon microelectrodes are prepared from carbon nanofibres (CNF) which are coated by glass. These conical microelectrodes are very sensitive and crashing into the surface may destroy them. Another possibility of fabricating carbon microelectrodes can be realized by carbonization of a gaseous carbon source (propane/butane) in a prior prepared micropipette under argon atmosphere. By choosing the right preparation technique, nearly every material that is used for normal sized electrodes (mm – cm) can also be used for a more or less easy microelectrode production. Most popular microelectrodes are made from Pt (74.0 %), C (10.8 %) Au (9.5 %), Hg (2.1 %) and Ag (1.7 %).<sup>[16]</sup>

To evaluate the response of a disk-shaped microelectrode, cyclic voltammetry is often used and its electrochemical behavior strongly differs from larger electrodes. As shown in **Figure 1a** and **b** the contributions of individual processes at micro- and bulk electrodes are different.

---

<sup>1</sup> The term “ultramicroelectrode” (UME) is frequently used for microelectrodes with metal diameter < 25  $\mu\text{m}$ .

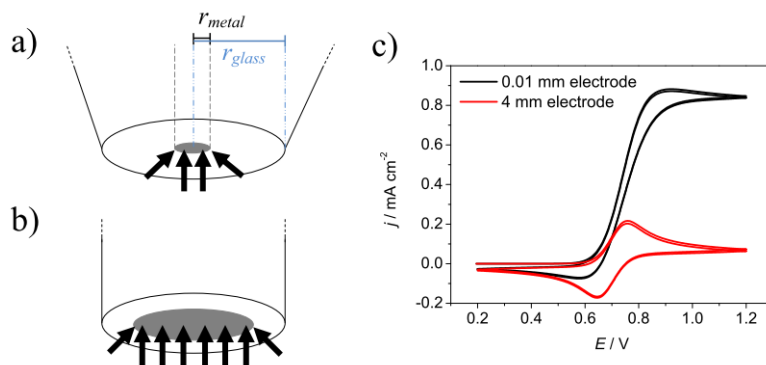


**Figure 1:** Schemes (not true to scale) of the diffusion profile of a microelectrode (arrows indicate planar and hemispherical diffusion) including the relevant characteristics (a) as well as a macroelectrode (b) and simulated CVs of spherical electrodes with different diameters (0.01 mm, 4 mm), with parameters: reaction  $A \rightarrow B + e$ ,  $E_0 = 0.7$  V,  $k_0 = 10^{-3}$  cm s $^{-1}$ ,  $a = 0.5$ ,  $[A] = 2$  mM,  $D_{A,B} = 10^{-6}$  cm $^2$  s $^{-1}$  (b), Figure follows the reference<sup>[17]</sup>.

At sufficient large overpotentials, the microelectrode response during an electrochemical reaction is dominated by a hemispherical diffusion profile of a redox active molecule whereas the contribution of planar diffusion is more dominant at large electrodes. The result of simulated cyclic voltammograms (CVs) can be found in **Figure 1c**. As hemispherical is more dominant than planar diffusion which is limited by the depletion of molecules, the current density ( $j$ , current with respect to the geometrical surface area) increases with decreasing electrode diameter. The main characteristics of a microelectrode are also marked in **Figure 1a**. From the radii of the metal and the insulating glass body, which are a result of the fabrication procedure, the important  $RG$  value can be determined for each planar microelectrodes by equation (1).

$$RG = \frac{r_{glass}}{r_{metal}} \quad (1)$$

In the positive potential region ( $E > 0.9$  V in **Figure 1**) a steady state current at the microelectrode ( $i_T$ ) can be found which is only related to the diffusion limitation and which can be approximated by equation (2)

$$i_T = g(RG) n F D c d \quad (2)$$

with  $g$  – geometrical constant,  $n$  – number of transferred electrons,  $F$  – Faraday constant,  $D$  – diffusion constant,  $c$  – concentration of the electroactive molecule and  $d$  – diameter of the microelectrode. According to the theory, the  $g(RG)$  value is 4 when the radius of the insulating glass is infinite. In most cases this value is taken when  $r_{glass}$  is at least ten times larger than  $r_{metal}$ .

From the instrumental point of view, it becomes clear that the microelectrode and its preparation are of particular importance. Also the quality of information as well as resolution is connected

with its features. Beside disk electrodes other types of microelectrodes were suggested, such as hemispherical,<sup>[18]</sup> conical<sup>[19]</sup> or ring-disk combination.<sup>[20]</sup> Even soft polymer/carbon microelectrodes which can work in contact mode are described.<sup>[21]</sup> A clearly different type of microelectrode is used in the field of potentiometric SECM. Here, micropipettes equipped with an ion-selective membrane are applied and the potential is measured against a reference electrode. This two-electrode setup is predominantly popular in corrosion studies and for local pH determination.<sup>[22]</sup>

Understanding the electrochemical behavior of microelectrode is essential to decide which type of SECM experiment can be applied and to interpret its results correctly.

### 1.1.3 Common working modes

Nearly all SECM experiments can be categorized into three main modes: the feedback, the generation collection and the competitive mode, which will be discussed in this section. There are some more, e.g. the direct mode which is mainly used for sample modification or micropatterning and will be left out here. The most prominent mode is the feedback mode which was fully described in the very beginning of the technology.<sup>[23]</sup> As already stated before, when applying the respective potential at a microelectrode a constant current can be measured resulting from the limited diffusion (**Figure 2a**).

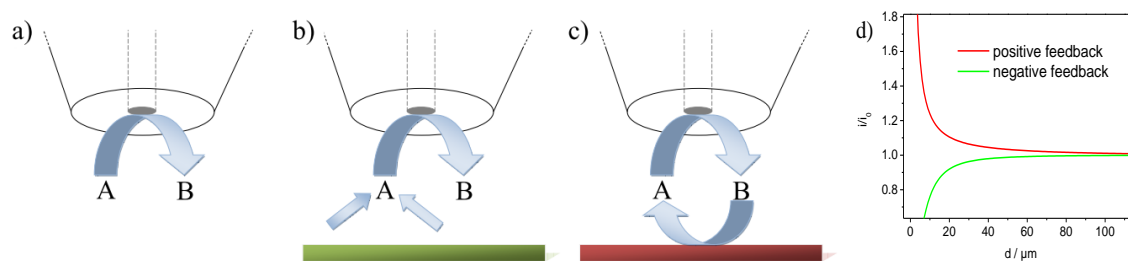


**Figure 2:** Schematic representation<sup>II</sup> of an electrochemical reaction ( $A \rightarrow B$ ) at the microelectrode (a) and the occurring effects when approaching to an insulating (b) or conductive substrate (c) as well as the theoretical current response of a 10  $\mu\text{m}$  microelectrode in dependence of the tip to substrate distance (d).

In **Figure 2b** and **c** the two limiting cases are displayed with the possible interactions between the appearing reaction at the microelectrode and a substrate surface. Approaching an insulating surface, it disturbs the hemispherical diffusion profile of the microelectrode. As a consequence,

<sup>II</sup> It should be noticed that schemes used in many works and also displayed in Figure 2 are only taken for the purpose of explanation and do not reflect the real working distance of the microelectrode which would be in the range of 0.5 to 2 times of the metal core diameter as it can also be concluded from Figure 2d.

the depletion of electroactive molecules leads to a decrease of the current which theoretically reaches zero amperes when the microelectrode is in full contact with the surface. This effect is called a negative feedback. When approaching to a conductive surface a current increase can be observed (positive feedback). The current increase is the result of accumulation of converted molecules within the gap between microelectrode and substrate. As all molecules are converted in the hemispherical diffusion area of the microelectrode, a concentration gradient between gap and the remaining electrolyte is created. This concentration gradient is equilibrated by electron transfer from the converted molecules to the conductive substrate which is considerably faster than diffusion. This effect can be compared to a concentration cell experiment.<sup>[24]</sup> As a consequence, the molecules in the gap remain available for another conversion at the microelectrode providing a current increase which is caused by a continuous loop of the redox reaction.

However, other factors also influence the positive feedback response at the microelectrode, e.g. the microelectrode diameter, the conductivity of the substrate and the electron transfer rate of the used mediator molecule.<sup>[25]</sup> For example, a low electron transfer rate of the back reaction which is necessary for the concentration equilibration can result in a positive feedback which suddenly changes into a negative when approaching the substrate.

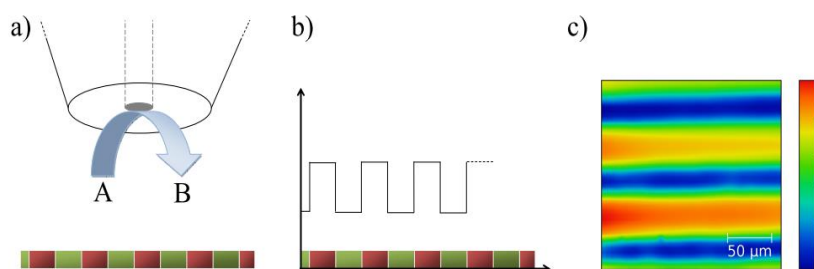


**Figure 3:** Scheme of an feedback experiment on a mixed conductive/insulating surface (a) and the resulting current with respect to the position (b) and an SECM image of 25  $\mu\text{m}$  gold ribbons on silicon giving different feedback response (c).

Positive and negative feedback response can be described by theoretical approximation which can be found for a 10  $\mu\text{m}$  microelectrode in **Figure 2d**. These theoretical curves can be used to determine the absolute tip to sample distance if all other parameters are known. With this constant distance, the microelectrode can be shifted to other positions along the sample (**Figure 3a**). At every position the feedback current will change depending on the substrate (**Figure 3b**) and can be combined to lines or arrays for imaging purpose (**Figure 3c**). The result is an electrochemical topography of the substrate reflecting surface reactivity or conductivity, with the restriction that the sample has to be flat. Both effects can be found at unbiased samples as

well as at biased ones. At non-flat samples, the SECM image can even be the result of changing tip to sample distances. To avoid this, the constant distance mode was suggested to obtain a surface topography.<sup>[11,26]</sup> A variant of the feedback SECM experiment is the surface interrogation mode (SI-SECM) which was introduced by Rodriguez-Lopéz in 2008. In this mode an adsorbate is formed at the substrate electrode by electrochemical reaction. The microelectrode in close proximity generates a titrant which can react with the adsorbed species resulting in a positive feedback at the microelectrode which lasts as long as adsorbate molecules are available. In a subsequent experiment the procedure is repeated without adsorbate. The difference of charge exchanged during the both titration experiments can be used for quantifying the adsorbate of the first experiment at the substrate electrode.<sup>[27]</sup>

Three other prominent modes of SECM will be discussed in the following which are often used in electrochemical research to characterize a substrate material. These modes can be found in **Figure 4** where “M” is an electroactive mediator molecule which can be either converted by the microelectrode, the substrate or both. The electroactive mediator may be ions, molecules, appearing intermediates or dissolved gases. Also in this case, the terms “positive” and “negative feedback” regarding the microelectrode or substrate response can be used when the observed current is divided by the initial current.

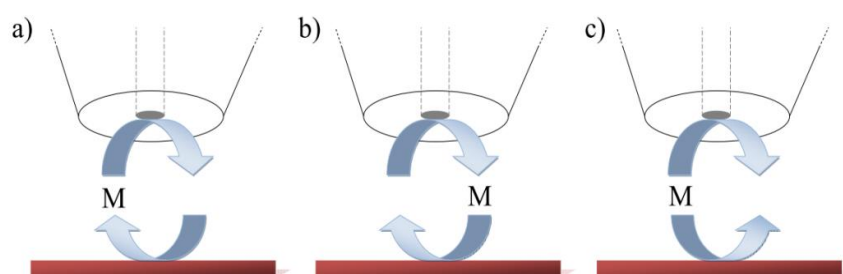


**Figure 4:** Modes of SECM experiments where M represents an electroactive mediator in solution: sample generation/tip collection (a) tip generation/sample collection (b) and competitive/shielding mode (c).

First, the sample generation/tip collection (SG/TC) mode (**Figure 4a**) can be used to probe a substrate towards its activity of evolving an electroactive molecule which can be detected at the microelectrode. This experiment leads to a positive feedback when the substrate is active. Second, the tip generation/sample collection (TG/SC) mode (**Figure 4b**) is used to analyze a substrate with regard to its activity towards consuming an electroactive molecule which is generated at the microelectrode. In this case, a positive feedback can be found by recording the substrate bias. Third, the competitive or shielding mode (**Figure 4c**) where substrate and microelectrode compete for the very same molecule. In case of an active substrate, a negative

feedback can be found at the microelectrode indicating the predominant consumption by the substrate. In all cases the described feedback has to be considered with respect to position and/or applied substrate potential.



## 1.2 Advanced spectroscopic methods coupled to SECM

Electrochemistry provides a number of dynamic or steady-state methods which allow for the characterization of an electrode material, an electroactive molecule in solution or a redox process. However, in most cases no information on structures or structural changes is obtained. To validate electrochemical results, it can be useful to record data by another technique in a subsequent or, which is more desirable, in a parallel experiment. Spectroscopic methods allow for the *in situ* determination of formed adsorbates, intermediates or active phases. Additionally, they may provide time-resolved information which allows conclusions about reaction kinetics and reaction pathways.

In the field of spectroelectrochemistry various *in situ* techniques can be found which can be coupled to an electrochemical experiment, such as X-ray diffraction (XRD) and synchrotron techniques, electron paramagnetic resonance (EPR), UV/Vis, IR and Raman spectroscopy.<sup>[28]</sup>

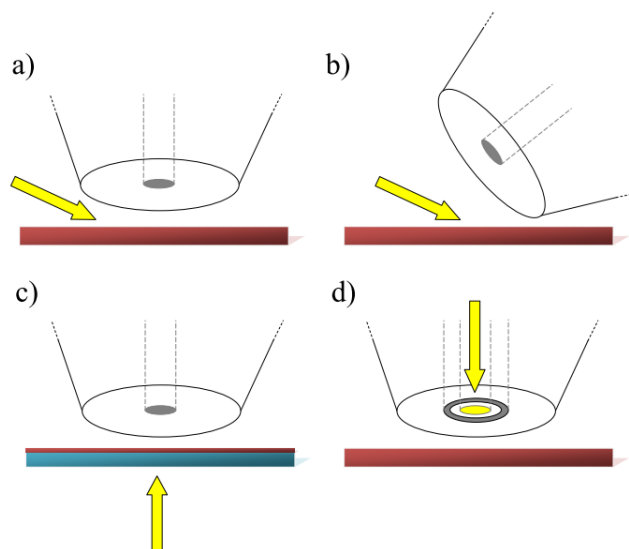


**Figure 5:** Possibilities of introducing a spectroscopic technique (yellow arrow) to a common SECM experiment.

For SECM, the addition of another complementary technique is of particular interest because the SECM experiment in a four-electrode setup (with biased sample) already generates two complementary data sets which can provide relevant electrochemical information. By adding another, preferably spatially resolved spectroscopic technique to the SECM experiment, three types of information can be obtained in parallel which provides a more comprehensive picture about the occurring electrochemical processes at the substrate electrode.

Coupling another technique to an SECM experiment brings in additional challenges which need to be solved. As SECM already uses a microelectrode as probe it has to be considered how a further substrate probing can be realized. As displayed in **Figure 5a** the microelectrode is

relatively large due to its large insulating shaft. In most cases the working distance is in the regime of metal core diameter of the microelectrode. To provide space for a parallel spectroscopic probing of the identical position from the very same side, it would be necessary to change the standard SECM experimental geometry. This can be realized by tilting the electrode to one side to free some space for the spectroscopic probing (**Figure 5b**). In this way, the combination of Raman microscopy and shearforce regulated SECM was shown by Etienne *et al.*<sup>[29]</sup> Shearforce regulation ensures a constant distance to the sample which makes this instrument applicable to samples with strong height deviations (> 10  $\mu\text{m}$ ). Another possibility of sample probing can be realized by using the backside of the sample electrode (**Figure 5c**). This setup needs a (conductive) substrate sample which is transparent for the relevant wavelength region. Wang and coworkers showed an ATR-IR SECM *in situ* instrument which allowed IR probing of a polymerization process on non-conductive ATR crystal induced by SECM feedback experiment.<sup>[30]</sup> In another work, ATR-IR was used to monitor the currentless microelectrode approaching to the ATR crystal which could be correlated to the electrochemical approaching.<sup>[31]</sup> A further possibility of coupling a spectroscopic method could be realized by a metal-coated optical fiber as displayed in **Figure 5d**. This fiber-ring microelectrode was already suggested for the determination of photoelectrochemical properties. For this purpose, a light source was connected to the optical fiber and the metal ring was used for product detection.<sup>[32]</sup>

## 1.3 SECM in electrochemical research

### 1.3.1 Advantages and opportunities

Similar to other scanning probe microscopic techniques, the main advantage of SECM is the possibility of imaging the distribution of physicochemical properties of a surface. But even more than that, in SECM it is not a single physical effect which can be used for illustration purpose.

Generally, a large number of molecules that are soluble in an aqueous or non-aqueous electrolyte can be used to design an experiment which characterize the reactivity of the sample surface to be investigated. Also the reactivity towards different molecules of interest could be studied in subsequent or parallel experiments by varying the respective potential region or in a potential pulse experiment. This approach also allows for the quantification of the educt as well as the product or even appearing intermediates in one experiment which may finally lead to a large number of SECM images of the very same sample surface. By careful preparation of samples containing more than one active spot, SECM is a suitable high-throughput technique that is capable of screening a large number of micrometer-sized spots in parallel. The results help to distinguish between different materials or material compositions and to identify the most reactive ones.

This emphasizes why SECM can support the search for new materials, especially in the field of electrochemical conversion. Beside the imaging purpose, SECM can be used to characterize the electrochemical processes occurring at the microelectrode and/or at the sample more in detail. Especially the feedback mode helps to determine rate constants by modeling the approach curve current or even diffusion constants. By using a defined substrate, the surface coverage of educts or intermediates can be quantified. All these advantages show why SECM became so popular in electrocatalysis research in the last decades.

However, there are some challenges concerning this technique. In particular, the electrochemical experiment has to be carefully evaluated ensuring that other effects such as from side reactions, deactivation of the electrode or precipitation processes are excluded. It is necessary to guarantee that only the desired electrochemical process is used for imaging purpose. Otherwise the SECM image can be falsified by various side effects. Concerning the enhanced resolution that is often desired, it should be clear that the microelectrode cannot be indefinitely small because a certain number of electrons must be transferred during a redox process to obtain an evaluable signal. As with all other electrochemical techniques which use

half-cell characterization methods, it has also to be carefully checked if and how the SECM results and conclusions actually can be used to understand the behavior of the targeted application, e.g. electrolyzers, fuel cell or battery systems.

### 1.3.2 Oxygen reduction and evolution reaction

This section dealing with the prominent electrochemical conversion of oxygen to water and its back reaction will briefly sum up the required systems and will show how SECM technique can help to understand appearing processes at different active materials for the respective reactions. The first part focuses on the oxygen reduction reaction (ORR), the second deals with the oxygen evolution reaction (OER) and the third part shows concepts of bifunctional materials combining activity for both electrochemical reactions.

As a vivid illustration, **Figure 6** shows how both reactions are involved in a sustainable and emission free energy storage process based on hydrogen as energy carrier. Although hydrogen is the storage molecule, the reduction or formation of oxygen is the bottleneck of the system which decreases the efficiency and which will be the focus of interest in the following.

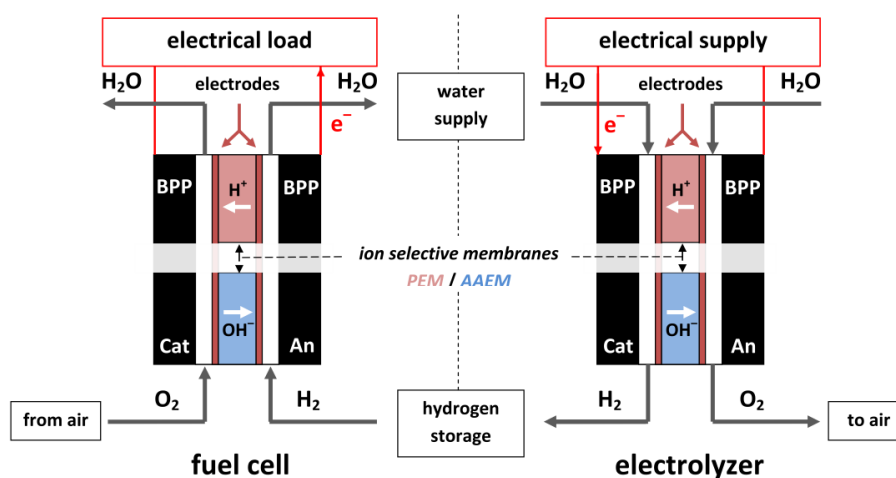
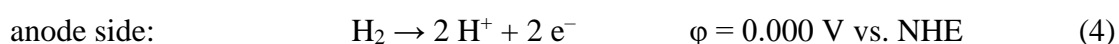
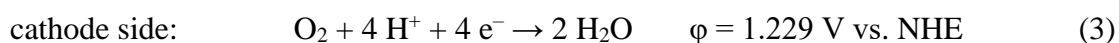


**Figure 6:** Scheme of a single fuel cell and electrolyzer cell operating with proton exchange (PEM), red, or alkaline anion exchange membrane (AAEM), blue, with relevant compartments providing an elegant approach for chemical energy storage (in form of hydrogen) and supply, BPP – bipolar plates, An – anode side, Cat – cathode side.

The oxygen reduction reaction (ORR) is probably one of the most essential reactions on earth. Beside the great importance for biological systems this reaction can be found in relevant energy conversion and storage systems, such as fuel cells (**Figure 6**, left) and metal-air batteries. In all types of fuel cells, this reaction is taking place at the cathode side of the electrochemical cell which is displayed in equation (3).



Here, oxygen is reduced to water using four protons and electrons. It acts as oxidation agent which is necessary to convert the fuel at the anode side. This may not necessarily be hydrogen as shown in equation (4) but can also be short-chain alcohols (methanol, ethanol) and higher oxidized derivatives, such as formic acid, ethylene glycol for low temperature fuel cells application as well as methane in high temperature fuel cells which is internally reformed to carbon monoxide and hydrogen before. However, the low temperature systems, such as proton exchange membrane (PEM) and direct-methanol fuel cells (DMFC) are of particular interest because of favorable thermodynamics and high theoretical efficiencies (~ 80 % at 100 °C). Working at lower temperatures (typically < 100 °C) requires electroactive materials that can catalyze each of the multistep, four electron reduction process which is necessary for obtaining water as product. The reasons can be found in the sluggish ORR kinetics which comprises a O–O bond cleavage and the formation of four O–H bonds. Electrochemical oxygen reduction in aqueous solution can be described by two different electron transfer pathways. On the one hand, the direct four-electron transfer pathway as described in equation (3) and on the other hand the indirect (consecutive) two-electron transfer pathway with hydrogen peroxide as appearing intermediate as summarized in equations (5) and (6) for acid solutions.<sup>[33]</sup>



As already stated, the slow ORR kinetic, including various reaction steps such as adsorption, desorption, protonation, O–O bonding cleavage or electron transfer where some of them are discussed to be the rate-determine step, require highly active materials depending on the respective media. In acidic media as in PEM fuel cells, Pt shows high activity for ORR. Further activity increase can be found at bimetallic alloys PtM with non-noble transition metals such as M = Co, Fe or Ni due to Pt d-band distortion.<sup>[34]</sup> The 111 facet of Pt<sub>3</sub>Ni was found to exhibit the highest ORR activity,<sup>[35]</sup> however, stability issues of such materials containing non-noble transition metals which can be leached out during electrochemical stress are still unsolved. In basic media, a broad variety of materials can be used. Beside only-carbon electrodes which show slight activity for ORR, the addition of heteroatoms and transition metals followed by a temperature treatment can enhance activity. Although it seems favorable to focus on alkaline fuel cells which can work with relatively cheap cathode materials, other disadvantages such as

low ion conductivity of the alkaline membrane impede the application up to now. Alkaline membranes degraded<sup>[36]</sup> and instability of various types of alkyl ammonium polymers has been shown.<sup>[37]</sup> New approaches using Spiro-ionene polybenzimidazole mixtures may overcome ion conductivity and stability issues.<sup>[38]</sup> In future, these developments may substitute the classic alkaline electrolyzer systems that still use 30 % KOH solution as liquid electrolyte.

Scanning electrochemical microscopy was used to study a broad variety of materials towards their ORR activity whereby a large amount of research was contributed by the group of Bard. In an early experiment they showed how the feedback mode can be used to determine heterogeneous rate constants of the ORR on biased Pt substrate in alkaline solution by approach curves and their theoretical evaluation.<sup>[39]</sup> Later on, they suggested the TG/SC mode with constant current at the microelectrode which continuously produces oxygen by means of a 9 V battery.<sup>[40]</sup> This experimental setup was used to study ORR kinetics in acidic media<sup>[41]</sup> and to characterize bi-<sup>[42]</sup> or tri-metallic catalysts<sup>[43]</sup> in combinatorial studies. In all these experiments the substrate current, which increased when the microelectrode reaches an active spot, was used as relevant parameter which was a main disadvantage, due to the limited signal-to-noise ratio at large substrate samples. In 2006 the group of Schuhmann suggested the redox competition mode (RC-SECM)<sup>[44]</sup> which uses the current at the microelectrode to analyze substrate activity. Here, a pulse profile is applied at the microelectrode where in the first step oxygen is generated which is reduced in the second step immediately afterwards. Active materials in close proximity to the microelectrode can, depending on the applied potential, consume some of the generated oxygen which then cannot be reduced at the microelectrode. This competitive experiments allows conclusions about the studied materials in terms of ORR activity. In a further work, it was also shown that formed hydrogen peroxide can be detected by the addition of another pulse step.<sup>[45]</sup> As a consequence, the evaluation of the currents derived from oxygen reduction and peroxide oxidation at the microelectrode could be used to determine the number of transferred electrons similar to rotating ring disk electrode (RRDE) experiments. This method was used to analyze non-noble metal electrocatalysts<sup>[46]</sup> as well as the influence of the ionomer amount at noble metal catalysts.<sup>[47]</sup> Hydrogen peroxide as main ORR intermediate came also into the focus of research. The group of Wittstock showed the quantification of hydrogen peroxide during ORR by a transient SG/TC mode of SECM and was able to model the microelectrode response and the related rate constants of the relevant pathways for electrode materials with moderate (PtCo alloy) or high hydrogen peroxide formation activity (Au).<sup>[48]</sup> For the case of Pd they could show that also morphology influences the result.<sup>[49]</sup> In contrast to the transient SG/TC mode of

SECM, Sánchez-Sánchez showed steady-state SG/TC experiments with well-defined substrate electrodes even at electrodes with high hydrogen peroxide formation activity (Au, Hg). By evaluating the collector efficiency a determination of the hydrogen peroxide amount as well as the number of transferred electrons was possible.<sup>[50]</sup> In a further study, relevant electrode materials which may act as ORR catalyst were analyzed. It was shown that Hg electrodes reduce oxygen taking the two-electron pathway, whereas Pt and Pd<sub>80</sub>Co<sub>20</sub> show a predominant four-electron pathway.<sup>[51]</sup> To summarize the examples mentioned above, SECM was used on the one hand to analyze large catalyst libraries and on the other to study the mechanism of ORR electrocatalysis at different materials which presents a helpful contribution to fuel cell catalyst development.

As shown in **Figure 6**, to create a storage system where hydrogen acts as energy storage molecule it is necessary to produce this hydrogen in a different approach than today. Instead of steam reforming, which is still the main route for hydrogen production, powerful and efficient water electrolysis systems are required. As in fuel cell technology also here the process can be realized in acid or alkaline media which both have different advantages and disadvantages.<sup>[52]</sup> Both have in common that the oxygen evolution reaction (OER) is the critical part of electrochemical water splitting which arises from different stabilities of M–O, M–OH and M–OOH intermediates on the metal oxide surface.<sup>[53]</sup> From the catalyst point of view, acid media require noble metal oxide catalyst such as IrO<sub>2</sub> and RuO<sub>2</sub>, whereas in alkaline media various transition metals oxides, especially NiO, Co<sub>3</sub>O<sub>4</sub> and Mn<sub>3</sub>O<sub>4</sub> show highest activity. Not surprisingly also the oxygen evolution reaction was investigated by SECM. However, the number of studies is far smaller compared to ORR. Also in this case, the SG/TC mode of SECM is of particular interest because oxygen can be evolved from a substrate electrode and detected by electrochemical reduction at the microelectrode. Snook *et al.* presented linear sweep voltammetry of NiO-containing substrates while the microelectrode with constant reduction potential was placed in close distance to the film. This allowed for the determination of the *onset* potential, the apparent beginning of the OER.<sup>[54]</sup> In another work, array electrodes from mixed SnO<sub>2</sub>/IrO<sub>2</sub> were studied by a shielding SG/TC mode towards OER activity. Shielding was realized by a gold layer on the glass body of the microelectrode where oxygen was permanently reduced. This was necessary to lower the effect of an overall oxygen concentration increase over a longer period.<sup>[55]</sup> In a more recent work, the same group suggested a double-pulse method to avoid increasing background current from neighboring spots.<sup>[56]</sup> Schmachtel *et al.* determined proton, oxygen and hydrogen peroxide concentration at MnO<sub>2</sub> catalyst during

OER and were able to model the experimental data.<sup>[57]</sup> Näslund and coworkers showed the effect of TiO<sub>2</sub> doping on RuO<sub>2</sub> electrodes (DSA-type) and found a more evenly distribution of OER activity at the doped part of the electrode as well as enhanced activity of cracks in the film.<sup>[58]</sup> In another work the group of Schuhmann showed an approach equal to the work of Snook for determination of the *onset* potential by stepwise potential increase for perovskite and RuO<sub>2</sub> catalysts.<sup>[59]</sup> In a more recent work, they studied OER activity of perovskite catalysts using a double cavity electrode where one was always filled with RuO<sub>2</sub> catalysts as internal reference. This setup allowed for a more precise determination of the *onset* potential by decoupling interfering reactions.<sup>[60]</sup> As summarized here, SECM was used to analyze OER catalysts with comparable approaches as in ORR catalyst research. Oxygen diffusion which can pretend higher OER activity of an individual catalyst spot was identified as a notable problem when catalysts spot arrays or libraries are scanned.

As it can be concluded from **Figure 6**, fuel cells and electrolyzers have many compartments in common. So, it is not surprising that it was also suggested to merge both devices to one electrochemical cell. For this device, bifunctional catalysts which exhibit high ORR and OER activity would be necessary. This is mainly realized by mixing of active materials of the respective reactions. Different materials were already studied towards both reactions. Typically, ORR is probed by RC-mode of SECM, whereas for OER the SG/TC mode is used.<sup>[61]</sup>



### 1.3.3 Chlorine evolution reaction

Regarding energy storage application the  $\text{Cl}_2/\text{Cl}^-$  redox couple was suggested to substitute the sluggish  $\text{O}_2/\text{H}_2\text{O}$  redox system at the positive side of a regenerative fuel cell-electrolyzer system<sup>[62]</sup> as mentioned in **Figure 6**. In laboratory scale, this system shows high efficiencies due to the fast electrode kinetics of the highly reversible reaction.<sup>[63]</sup> However, some drawbacks should be taken into consideration. In the fuel cell part, corrosion is described as a serious disadvantage which demands for highly resistant materials as well as improvements of water management to obtain stable operation.<sup>[64]</sup> So far, there is no commercial application of a hydrogen-chlorine energy storage system which may also be attributed to the harmful chlorine as one of the storage molecules.

Nevertheless, the  $\text{Cl}_2/\text{Cl}^-$  redox couple is still of particular importance concerning one of the most important electrochemical processes in industry. The production of chlorine in Europe has reached 12.3 million t per year in 2016.<sup>[65]</sup> So far, the produced amount is still a measure of the countries' economic performance although it was decided to curtail the worldwide production in the middle of the 1990<sup>th</sup>. Chlorine is one of the most important chemical commodities used in a variety of industrial processes. It is produced by the Chlor-Alkali process where the electrochemical cell is the main component. Up to now, there are three types of cells in use that differ in applicable current density, educt and product grade as well as in environmental aspects. In Europe, the membrane process has developed to the technology of choice and reached more than 50% of the overall capacity.<sup>[66]</sup>

Electrodes used for the chlorine evolution reaction (CER) taking place at the anode side of the electrochemical cell must meet relevant criteria, such as high catalytic activity and related to this a low overpotential, stability towards oxidation at harsh conditions as well as good conductivity. In the beginning, anodes made out of platinum, magnetite or carbon were used but none of them could fulfilled all the needs. Especially graphite, which was the mainly used material over decades, had many disadvantages, such as total oxidation to  $\text{CO}_2$  or product impurities from chlorinated hydrocarbons unavoidably generated as side products during the oxidation process. The breakthrough came in the 1960<sup>th</sup> when Cotton and Beer discovered the excellent features of  $\text{RuO}_2/\text{TiO}_2$  coating on titanium plates towards CER. These electrodes were named as dimensionally stable anodes (DSA<sup>®</sup> electrodes) stressing stability as their prominent feature. Even the catalytic activity was found to be magnitudes higher than that of the materials used before.<sup>[67]</sup> The development of DSA electrodes is considered as “one of the greatest

technological breakthrough of the past 50 years of electrochemistry”.<sup>[68]</sup> This underlines why this material also came into the focus of SECM research.

In 2011, SECM was proposed as analytical method to study the electrocatalytic activity of a commercial DSA for chlorine evolution by Zeradjanin *et al.* The SG/TC mode was applied to visualize electrochemically active areas on an inactive support at low polarization potentials. As shown in **Figure 4a**, chlorine as a mediator molecule is evolved by the DSA sample in dependence of the applied potential and detected by a Pt microelectrode in close proximity. In addition, it was also shown that it might be more beneficial to apply the redox competition (RC) mode of SECM (**Figure 4c**) to avoid the contribution of accumulated chlorine in the solution. In this case the consumption of chloride ions by the DSA is probed by a Pt microelectrode with a CER potential applied which finally allows to draw conclusions about the local CER activity.<sup>[69]</sup> However, in a following work again the SG/TC mode was used to study  $\text{Ru}_{0.3}\text{Sn}_{0.7}\text{O}_2$  coatings towards CER activity at low polarization potentials. SECM images of these coatings showed enhanced CER active in comparison to the commercial DSA material and the formation of CER active areas of several tens of micrometers within the apparently homogeneous coatings.<sup>[70]</sup> In the same way, these active areas were detected by SECM at Ti-Ru-Ir mixed metal oxides which showed enhanced CER activity and, in particular, selectivity.<sup>[71]</sup>

## 1.4 Basic aspects of material characterization for all-vanadium redox flow batteries

Redox flow batteries that can reversibly convert electrical into chemical energy are considered as one important contribution for the turnaround in energy policy in Germany. Several approaches have been demonstrated until now using a variety of elements and molecules in aqueous or non-aqueous solution as active mass for storage but only a limited number has achieved lab-scale or commercialization.<sup>[72]</sup> In contrast to other secondary batteries, redox flow systems consist of tanks containing electroactive molecules in aqueous or non-aqueous solution that must be transported, in most cases pumped, into an electrochemical cell where the redox reactions take place at electrodes in a membrane-separated electrochemical cell consisting of two half-cells. By connecting the half-cells to an electrical load or an energy source and realizing sufficient ion exchange for charge compensation through the membrane, these systems can show high reversibility and efficiency during charge-discharge cycling. The energy and power density is only limited by the size of the tanks which makes the system freely scalable.

Redox flow batteries can mainly be divided into two different groups based on the type of electroactive component, organic and inorganic, whereby the importance of the inorganic systems is considerably higher at the moment. Organic redox flow battery concepts still suffer from problems with stability and reversibility. A promising approach in this field using soluble organic polymers in aqueous solution was shown by Janoschka *et al.* in 2015.<sup>[73]</sup> A far greater focus was placed on the inorganic systems where beside the chromium-iron, the zinc-brome or the sulfur-brome, the vanadium-vanadium system caught much attention. The main advantage of the system developed and patented by Skyllas-Kaszacos and coworkers<sup>[74,75]</sup> in the middle of the 1980<sup>th</sup> was the less problematic cross contamination that is occurring in all redox flow cells using an ion selective membrane. Here, the cross contamination only results in a loss of efficiency in the charge-discharge cycling but not in a total breakdown as it can be found in systems with a non-homogeneous redox couple. Even the advantages of the VRFB as storage system for fluctuating energy from wind turbines or PV systems were highlighted early.<sup>[76]</sup> Nevertheless, it took several decades until the VRFB came into the focus again. Today many researchers try to improve different parts of the flow battery, on the one hand to improve efficiencies by minimizing occurring losses and on the other to understand the details of the occurring processes.

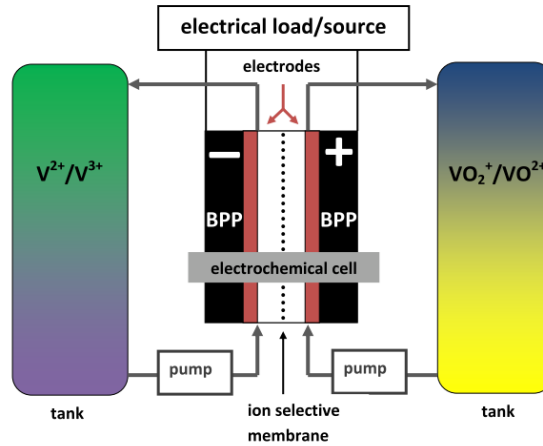
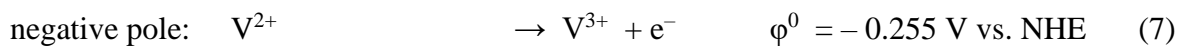


**Figure 7:** Schematic representation of an all-vanadium redox flow battery with all relevant compartments.

The setup of an all-vanadium redox flow battery (VRFB) is displayed in **Figure 7**. The most important part is the electrochemical cell consisting of an ion selective membrane, electrodes and bipolar plates (BPP) as well as current collectors (not displayed). The respective solution containing either the sulfate compounds of V(II)/V(III) or V(IV)/V(V) is continuously pumped into the cell while the system is charging or discharging. The reactions at the electrodes can be summarized for the discharge process as follows:



During charging both half-cell reactions run in opposite direction. At the negative pole<sup>III</sup> V(II) is oxidized to V(III) and at the positive pole V(V) is reduced to V(IV). As supporting electrolyte half-concentrated sulfuric acid is used with respect to the stability and solubility of the oxovanadium compounds. As shown in equation (8) at the positive pole protons are needed when the battery is discharged which have to be additionally delivered from the other half-cell through the ion selective membrane. Proton exchange membranes (PEM, e.g. Nafion<sup>®</sup> 117) can be used to realize charge compensation but also anion exchanging membranes, such as a sulfate exchanging membrane are possible. From both half-cell potentials determined against the normal hydrogen electrode (NHE) a currentless cell voltage ( $E_0$ ) of 1.255 V can be derived. During discharging while the load is operating  $E(I) < E_0$  and during charging  $E(I) > E_0$ . The contributions of losses during discharging at the positive half-cell ( $\varphi_{loss,+}$ ), at the negative half-

<sup>III</sup> In secondary batteries only the term “pole” should be used to avoid confusion because the frequently used terms “cathode” and “anode” strictly depend on the direction of the respective reaction during charge or discharge.

cell ( $\varphi_{loss,-}$ ) and additional losses, such as electrolyte, membrane and transport resistance as well as conductivity are summarized in the following equation:

$$E(I) = E_0 - \varphi_{loss,+} - \varphi_{loss,-} - IR \quad (9)$$

All losses which are also named as overpotentials can be minimized by optimizing individual components of the battery. The most important role is played by the electrodes where the respective electrochemical reaction takes place including diffusion and adsorption of the educts, charge transfer as well as desorption and diffusion of the products. Here, many researchers focus on understanding the occurring processes and improving the electrode material by modifying the carbon material itself, introducing heteroatoms or addition of other molecular compounds. In contrast to other electrochemical energy converters, such as fuel cells or electrolyzers using noble metal-based electrocatalysts, the VRFB works with carbon-based electrodes. In the very beginning bulk graphite plates<sup>[74]</sup> were used which were expeditiously exchanged by graphite felt and chemically modified graphite felt electrodes<sup>[77]</sup> providing much higher inner surface area for high current densities. Even new carbon allotropes that were found to be stable, such as fullerenes, carbon nanotubes or graphene were found to be promising materials to be used in VRFB in the last decades. In the following part some of the materials will be discussed more in detail.

Highly ordered carbon structures as they can be found in single- or multi-walled carbon nanotubes (SW-/MWCNT) are promising because they combine both, high surface area as well as fast electron transport along the axis of the tube. CNTs were studied as electrode material, in particular, for the positive side of the battery<sup>[78]</sup> and a positive effect of a chemical or electrochemical introduction of oxygen containing surface groups was found. In some work, however, contrary results concerning the effect of surface functionalization at MWCNTs were reported.<sup>[79]</sup> Battery experiments with nitrogen-doped carbon nanotubes (NCNT) on graphite felt showed improved charge-discharge cycling in comparison to the non-treated reference resulting in higher efficiencies.<sup>[80]</sup> Recently graphene and graphene oxide<sup>IV</sup> (GO) were also studied for the use in VRFB as another promising carbon material.<sup>[81,82]</sup> Oxygen-containing functional groups comparable to those in CNTs were brought into the material to verify the influence and the already suggested reaction mechanisms were confirmed.<sup>[82]</sup> Beside

---

<sup>IV</sup> As graphene is a single atom layer of graphite by definition, most of the publications overuse this term and finally utilize nanocrystalline or few layer graphite or graphite oxide. Up to now there is no successful large scale production of “single-layered” graphene established which limits the usability for industrial application.

introducing nitrogen atoms<sup>[83]</sup> also an effect from halogens at the GO surface was found.<sup>[84]</sup> Composite materials from GO and CNTs were also discussed.<sup>[85]</sup> Almost all studies describe a positive impact of introducing foreign atoms into carbon materials on the efficiency of VRFB. CNTs and graphite/graphene is often synthesized in form of a powder. Possibilities to bind them to a support material, e.g. graphite felt or carbon non-woven, were discussed. Examples are MWCNTs linked to carbon felt by chemical vapor deposition (CVD)<sup>[86]</sup> as well as nanocrystalline graphite at a polyacrylonitrile (PAN) fiber support.<sup>[87]</sup> Beside carbon-carbon also carbon-polymer composites were studied giving the possibility to combine BPP and electrode to one compartment.<sup>[88]</sup> Today, carbon felt<sup>[89]</sup> and carbon paper electrodes<sup>[90]</sup> are used as state-of-the-art material in VRFB. In addition to electrode materials based on carbon only, also metals,<sup>[91]</sup> metal alloys,<sup>[92]</sup> noble metals<sup>[93]</sup> and metal oxides<sup>[94]</sup> were intensively studied. Nevertheless, all these materials do not seem to form promising alternatives in terms of battery efficiency and costs in comparison to carbon-based electrodes up to now.<sup>[95]</sup>

Battery experiments often include charge-discharge cycles for determination of the voltage, charge and power efficiency. But by this method, the individual influence of modification of the electrode in the respective half-cell can hardly be separated. In consequence, different electrochemical characterization techniques are applied to quantify the influence of individual material modifications. In many studies, cyclic voltammetry (CV) is applied as main technique to characterize the electrochemical behavior of the V(II)/V(III) and V(IV)/V(V) conversion in an obviously faster and more simple way. Even the sample amount used for each experiment is substantially lower than in a battery setup. From CV analysis a number of parameters, such as peak potential and height, peak-to-peak distance as well as kinetic information can be extracted from the curves in order to characterize the electrode and compare them to others. In particular, the peak-to-peak distance ( $\Delta E$ ), i.e. the difference of the peak potentials at maximum current of the oxidation and reduction is applied as a mean of reversibility of the respective redox reaction. This procedure is based on a theory by Nicholson from the middle of the 1960<sup>th</sup> showing a relation between the kinetic parameter and the peak separation  $\Delta E$  for planar electrodes.<sup>[96]</sup> However, as in other cases this approach is wrongly used in VRFB research for porous electrodes although it is known that porosity is contributing to the results of CV measurements as well.<sup>[97]</sup> Hence, extracted kinetic data may be falsified resulting in a variety of derived kinetic parameters that strongly differ even at quite similar electrodes and electrolyte conditions.<sup>[98]</sup>

To overcome these problems and to improve the way of material characterization, steady-state polarization curves are suggested as the most suitable way. Additionally, the dynamic of a flow cell must be respected during the electrochemical characterization. Goulet and coworkers showed a small-scale, microfluidic half-cell which allowed the determination of kinetic data by applying different flow rates.<sup>[99]</sup> A half-cell setup for carbon felt electrodes in a flow-through configuration was realized by Becker *et al.* who could fit the data to Butler-Volmer behavior for states of charge (SOC) between 25 % and 75 %.<sup>[100]</sup> Beside half-cell measurements it can also be useful to equip the RFB with additional reference electrodes for *in situ* characterization of the electrode materials and to identify individual losses. For a microfluidic cell this was shown with integrated reference electrodes in the electrolyte reservoirs.<sup>[101]</sup> Aaron *et al.* integrated Pt wires as direct hydrogen electrode between two Nafion membranes to obtain kinetic information from polarization curves.<sup>[102]</sup> With the same setup, additional information can be gained from impedance spectroscopy.<sup>[103]</sup>

Different methods employing conditions close to the application of VRFB are necessary to study the individual processes in more detail and to understand observed material effects. Electrochemical experiments under steady-state conditions with defined mass transport, as also the case in SECM experiments seems to be the more favorable methods to extract relevant data. The development of such advanced (*in situ*) techniques may even be useful for other redox flow systems in future.

## 1.5 References

- [1] H. Rohrer, G. Binnig, *Helv. Phys. Acta* **1982**, *55*, 726.
- [2] G. Binnig, C. F. Quate, C. Gerber, *Phys. Rev. Lett.* **1986**, *56*, 930.
- [3] a) J. Gomez, L. Vazquez, A. M. Bar, N. Garcia, C. L. Perdriel, W. E. Triaca, A. J. Arvia, *Nature* **1986**, *323*, 612; b) L. Vazquez, J. Gomez, A. M. Baro, N. Garcia, M. L. Marcos, J. Gonzalez Velasco, J. M. Vara, A. J. Arvia, J. Presa, *J. Am. Chem. Soc.* **1987**, *109*, 1730.
- [4] B. Drake, R. Sonnenfeld, J. Schneir, P. K. Hansma, *Surf. Sci.* **1987**, *181*, 92.
- [5] a) O. Lev, F. R. F. Fan, A. J. Bard, *J. Electrochem. Soc.* **1988**, *135*, 783; b) P. Lustenberger, H. Rohrer, R. Christoph, H. Siegenthaler, *J. Electroanal. Chem. Interfacial Electrochem.* **1988**, *243*, 225; c) J. Wiechers, T. Twomey, D. M. Kolb, R. J. Behm, *J. Electroanal. Chem. Interfacial Electrochem.* **1988**, *248*, 451.
- [6] R. E. Lindstrom, *The use of electrochemical scanning tunnel microscopy (EC-STM) in corrosion analysis. Reference material and procedural guidelines*, Woodhead Pub, Cambridge, England, **2007**.
- [7] R. C. Engstrom, M. Weber, D. J. Wunder, R. Burgess, S. Winqvist, *Anal. Chem.* **1986**, *58*, 844.
- [8] a) A. J. Bard, F. R. F. Fan, J. Kwak, O. Lev, *Anal. Chem.* **1989**, *61*, 132; b) R. C. Engstrom, C. M. Pharr, *Anal. Chem.* **1989**, *61*, 1099A.
- [9] L. Danis, D. Polcari, A. Kwan, S. M. Gateman, J. Mauzeroll, *Anal. Chem.* **2015**, *87*, 2565.
- [10] a) C. Lee, J. Kwak, A. J. Bard, *Proc. Nat. Acad. Sci. USA* **1990**, *87*, 1740; b) A. J. Bard, F.-R. Fan, D. T. Pierce, P. R. Unwin, D. O. Wipf, F. Zhou, *Science* **1991**, *254*, 68.
- [11] A. Hengstenberg, C. Kranz, W. Schuhmann, *Chem. Eur. J.* **2000**, *6*, 1547.
- [12] C. Kranz, G. Friedbacher, B. Mizaiakoff, A. Lugstein, J. Smoliner, E. Bertagnolli, *Anal. Chem.* **2001**, *73*, 2491.
- [13] T. H. Treutler, G. Wittstock, *Electrochim. Acta* **2003**, *48*, 2923.
- [14] N. Ebejer, M. Schnippering, A. W. Colburn, M. A. Edwards, P. R. Unwin, *Anal. Chem.* **2010**, *82*, 9141.
- [15] D. Momotenko, J. C. Byers, K. McKelvey, M. Kang, P. R. Unwin, *ACS Nano* **2015**, *9*, 8942.
- [16] D. Polcari, P. Dauphin-Ducharme, J. Mauzeroll, *Chem. Rev.* **2016**, *116*, 13234.
- [17] F. Marken, A. Neudeck, A. M. Bond in *Electroanalytical Methods. Guide to experiments and applications* (Ed.: F. Scholz), Springer, Berlin, **2010**, pp. 57–106.
- [18] J. Mauzeroll, E. A. Hueske, A. J. Bard, *Anal. Chem.* **2003**, *75*, 3880.
- [19] H. Xiong, J. Guo, K. Kurihara, S. Amemiya, *Electrochem. Commun.* **2004**, *6*, 615.
- [20] P. Liljeroth, C. Johans, C. J. Slevin, B. M. Quinn, K. Kontturi, *Anal. Chem.* **2002**, *74*, 1972.
- [21] F. Cortés-Salazar, M. Träuble, F. Li, J.-M. Busnel, A.-L. Gassner, M. Hojeij, G. Wittstock, H. H. Girault, *Anal. Chem.* **2009**, *81*, 6889.
- [22] C. Wei, A. J. Bard, G. Nagy, K. Toth, *Anal. Chem.* **1995**, *67*, 1346.
- [23] J. Kwak, A. J. Bard, *Anal. Chem.* **1989**, *61*, 1221.
- [24] D. O. Wipf, *J. Electrochem. Soc.* **1991**, *138*, 469.
- [25] a) K. B. Holt, A. J. Bard, Y. Show, G. M. Swain, *J. Phys. Chem. B* **2004**, *108*, 15117; b) A. K. Neufeld, A. P. O'Mullane, *J. Solid State Electrochem.* **2006**, *10*, 808.
- [26] B. Ballesteros Katemann, A. Schulte, W. Schuhmann, *Chem. Eur. J.* **2003**, *9*, 2025.
- [27] J. Rodríguez-López, M. A. Alpuche-Avilés, A. J. Bard, *J. Am. Chem. Soc.* **2008**, *130*, 16985.



- [28] A. Neudeck, F. Marken, R. G. Compton in *Electroanalytical Methods. Guide to experiments and applications* (Ed.: F. Scholz), Springer Berlin, **2010**, pp. 179–200.
- [29] M. Etienne, M. Dossot, J. Grausem, G. Herzog, *Anal. Chem.* **2014**, *86*, 11203.
- [30] L. Wang, J. Kowalik, B. Mizaikoff, C. Kranz, *Anal. Chem.* **2010**, *82*, 3139.
- [31] L. Wang, C. Kranz, B. Mizaikoff, *Anal. Chem.* **2010**, *82*, 3132.
- [32] H. Ye, J. Lee, J. S. Jang, A. J. Bard, *J. Phys. Chem. C* **2010**, *114*, 13322.
- [33] E. Yeager, *Electrochim. Acta* **1984**, *29*, 1527.
- [34] V. R. Stamenkovic, B. S. Mun, M. Arenz, K. J. J. Mayrhofer, C. A. Lucas, G. Wang, P. N. Ross, N. M. Markovic, *Nat. mater.* **2007**, *6*, 241.
- [35] V. R. Stamenkovic, B. Fowler, B. S. Mun, G. Wang, P. N. Ross, C. A. Lucas, N. M. Markovic, *Science* **2007**, *315*, 493.
- [36] S. Chempath, B. R. Einsla, L. R. Pratt, C. S. Macomber, J. M. Boncella, J. A. Rau, B. S. Pivovar, *J. Phys. Chem. C* **2008**, *112*, 3179.
- [37] M. G. Marino, K. D. Kreuer, *ChemSusChem* **2015**, *8*, 513.
- [38] T. H. Pham, J. S. Olsson, P. Jannasch, *J. Am. Chem. Soc.* **2017**, *139*, 2888.
- [39] B. Liu, A. J. Bard, *J. Phys. Chem. B* **2002**, *106*, 12801.
- [40] J. L. Fernández, A. J. Bard, *Anal. Chem.* **2003**, *75*, 2967.
- [41] J. L. Fernández, A. J. Bard, *Anal. Chem.* **2004**, *76*, 2281.
- [42] a) J. L. Fernández, D. A. Walsh, A. J. Bard, *J. Am. Chem. Soc.* **2005**, *127*, 357; b) J. L. Fernández, J. M. White, Y. Sun, W. Tang, G. Henkelman, A. J. Bard, *Langmuir* **2006**, *22*, 10426; c) D. A. Walsh, J. L. Fernández, A. J. Bard, *J. Electrochem. Soc.* **2006**, *153*, E99.
- [43] J. L. Fernández, V. Raghuvier, A. Manthiram, A. J. Bard, *J. Am. Chem. Soc.* **2005**, *127*, 13100.
- [44] K. Eckhard, X. Chen, F. Turcu, W. Schuhmann, *Phys. Chem. Chem. Phys.* **2006**, *8*, 5359.
- [45] K. Eckhard, W. Schuhmann, *Electrochim. Acta* **2007**, *53*, 1164.
- [46] a) A. O. Okunola, T. C. Nagaiah, X. Chen, K. Eckhard, W. Schuhmann, M. Bron, *Electrochim. Acta* **2009**, *54*, 4971; b) A. Dobrzeniecka, A. Zeradjanin, J. Masa, A. Puschhof, J. Stroka, P. J. Kulesza, W. Schuhmann, *Catal. Today* **2013**, *202*, 55; c) A. Dobrzeniecka, A. R. Zeradjanin, J. Masa, M. Blicharska, D. Wintrich, P. J. Kulesza, W. Schuhmann, *Catal. Today* **2016**, *262*, 74.
- [47] A. Kishi, M. Inoue, M. Umeda, *J. Phys. Chem. C* **2010**, *114*, 1110.
- [48] Y. Shen, M. Träuble, G. Wittstock, *Anal. Chem.* **2008**, *80*, 750.
- [49] Y. Shen, M. Träuble, G. Wittstock, *Phys. Chem. Chem. Phys.* **2008**, *10*, 3635.
- [50] C. M. Sánchez-Sánchez, J. Rodríguez-López, A. J. Bard, *Anal. Chem.* **2008**, *80*, 3254.
- [51] C. M. Sánchez-Sánchez, A. J. Bard, *Anal. Chem.* **2009**, *81*, 8094.
- [52] M. Carmo, D. L. Fritz, J. Mergel, D. Stolten, *Int. J. Hydrogen Energy* **2013**, *38*, 4901.
- [53] I. C. Man, H.-Y. Su, F. Calle-Vallejo, H. A. Hansen, J. I. Martínez, N. G. Inoglu, J. Kitchin, T. F. Jaramillo, J. K. Nørskov, J. Rossmeisl, *ChemCatChem* **2011**, *3*, 1159.
- [54] G. A. Snook, N. W. Duffy, A. G. Pandolfo, *J. Electrochem. Soc.* **2008**, *155*, A262.
- [55] A. Minguzzi, M. A. Alpuche-Aviles, J. R. López, S. Rondinini, A. J. Bard, *Anal. Chem.* **2008**, *80*, 4055.
- [56] A. Minguzzi, D. Battistel, J. Rodríguez-López, A. Vertova, S. Rondinini, A. J. Bard, S. Daniele, *J. Phys. Chem. C* **2015**, *119*, 2941.
- [57] S. Schmachtel, S. E. Pust, K. Kontturi, O. Forsén, G. Wittstock, *J. Appl. Electrochem.* **2010**, *40*, 581.
- [58] L.-Å. Näslund, C. M. Sánchez-Sánchez, Á. S. Ingason, J. Bäckström, E. Herrero, J. Rosen, S. Holmin, *J. Phys. Chem. C* **2013**, *117*, 6126.

- [59] A. Maljusch, E. Ventosa, R. A. Rincón, A. S. Bandarenka, W. Schuhmann, *Electrochem. Commun.* **2014**, *38*, 142.
- [60] A. J. Botz, M. Nebel, R. A. Rincón, E. Ventosa, W. Schuhmann, *Electrochim. Acta* **2015**, *179*, 38.
- [61] a) X. Chen, A. J. R. Botz, J. Masa, W. Schuhmann, *J. Solid State Electrochem.* **2016**, *20*, 1019; b) G. Seiffarth, M. Steimecke, T. Walther, M. Kühhirt, S. Rümmler, M. Bron, *Electroanalysis* **2016**, *28*, 2335.
- [62] E. Gileadi, S. Srinivasan, F. J. Salzano, C. Braun, A. Beaufriere, S. Gottesfeld, L. J. Nuttall, A. B. Laconti, *J. Power Sources* **1977**, *2*, 191.
- [63] R. S. Yeo, J. McBreen, A. C. C. Tseung, S. Srinivasan, J. McElroy, *J. Appl. Electrochem.* **1980**, *10*, 393.
- [64] M. Thomassen, E. Sandnes, B. Børresen, R. Tunold, *J. Appl. Electrochem.* **2006**, *36*, 813.
- [65] Euro Chlor, *Installed chlorine production capacities*, **2016**.  
www.eurochlor.org/media/110998/capacities\_1-1-2016-for\_information\_sheet.pdf, retrieved on 26-10-2017.
- [66] T. O'Brien in *Handbook of industrial chemistry and biotechnology. Volume 1 and 2* (Ed.: J. A. Kent), Springer, New York, **2012**, pp. 1017–1038.
- [67] T. O'Brien, T. V. Bommaraju, F. Hine, *Handbook of chlor-alkali technology*, Springer, New York, **2005**.
- [68] S. Trasatti, *Electrochim. Acta* **2000**, *45*, 2377.
- [69] A. R. Zeradjanin, T. Schilling, S. Seisel, M. Bron, W. Schuhmann, *Anal. Chem.* **2011**, *83*, 7645.
- [70] R. Chen, V. Trieu, A. R. Zeradjanin, H. Natter, D. Teschner, J. Kintrup, A. Bulan, W. Schuhmann, R. Hempelmann, *Phys. Chem. Chem. Phys.* **2012**, *14*, 7392.
- [71] A. R. Zeradjanin, N. Menzel, W. Schuhmann, P. Strasser, *Phys. Chem. Chem. Phys.* **2014**, *16*, 13741.
- [72] J. Noack, N. Roznyatovskaya, T. Herr, P. Fischer, *Angew. Chem. Int. Ed.* **2015**, *54*, 9776.
- [73] T. Janoschka, N. Martin, U. Martin, C. Friebe, S. Morgenstern, H. Hiller, M. D. Hager, U. S. Schubert, *Nature* **2015**, *527*, 78.
- [74] M. Skyllas-Kazacos, *J. Electrochem. Soc.* **1986**, *133*, 1057.
- [75] M. Skyllas-Kazacos, US patent 4786567, **1988**.
- [76] M. Rychcik, M. Skyllas-Kazacos, *J. Power Sources* **1988**, *22*, 59.
- [77] a) B. Sun, M. Skyllas-Kazacos, *Electrochim. Acta* **1992**, *37*, 2459; b) B. Sun, M. Skyllas-Kazacos, *Electrochim. Acta* **1992**, *37*, 1253.
- [78] a) W. Li, J. Liu, C. Yan, *Carbon* **2011**, *49*, 3463; b) W. Li, J. Liu, C. Yan, *Electrochim. Acta* **2012**, *79*, 102; c) Z. González, P. Álvarez, C. Blanco, S. Vega-Díaz, F. Tristán-López, L. P. Rajukumar, R. Cruz-Silva, A. L. Elías, M. Terrones, R. Menéndez, *Sustainable Energy Technol. Assess.* **2015**, *9*, 105.
- [79] J. Friedl, C. M. Bauer, A. Rinaldi, U. Stimming, *Carbon* **2013**, *63*, 228.
- [80] S. Wang, X. Zhao, T. Cochell, A. Manthiram, *J. Phys. Chem. Lett.* **2012**, *3*, 2164.
- [81] a) P. Han, H. Wang, Z. Liu, X. Chen, W. Ma, J. Yao, Y. Zhu, G. Cui, *Carbon* **2011**, *49*, 693; b) Z. González, C. Botas, P. Álvarez, S. Roldán, C. Blanco, R. Santamaría, M. Granda, R. Menéndez, *Carbon* **2012**, *50*, 828.
- [82] M. Park, I.-Y. Jeon, J. Ryu, J.-B. Baek, J. Cho, *Adv. Energy Mater.* **2015**, *5*, 1401550.
- [83] J. Jin, X. Fu, Q. Liu, Y. Liu, Z. Wei, K. Niu, J. Zhang, *ACS Nano* **2013**, *7*, 4764.
- [84] M. Park, I.-Y. Jeon, J. Ryu, H. Jang, J.-B. Back, J. Cho, *Nano Energy* **2016**, *26*, 233.
- [85] P. Han, Y. Yue, Z. Liu, W. Xu, L. Zhang, H. Xu, S. Dong, G. Cui, *Energy Environ. Sci.* **2011**, *4*, 4710.

- [86] G. Wei, C. Jia, J. Liu, C. Yan, *J. Power Sources* **2012**, 220, 185.
- [87] G. Wei, M. Jing, X. Fan, J. Liu, C. Yan, *J. Power Sources* **2015**, 287, 81.
- [88] C. Hagg, M. Skyllas-Kazacos, *J. Appl. Electrochem.* **2002**, 32, 1063.
- [89] K. J. Kim, Y.-J. Kim, J.-H. Kim, M.-S. Park, *Mater. Chem. Phys.* **2011**, 131, 547.
- [90] D. Aaron, Q. Liu, Z. Tang, G. Grim, A. Papandrew, A. Turhan, T. Zawodzinski, M. Mench, *J. Power Sources* **2012**, 206, 450.
- [91] B. Li, M. Gu, Z. Nie, Y. Shao, Q. Luo, X. Wei, X. Li, J. Xiao, C. Wang, V. Sprenkle et al., *Nano Lett.* **2013**, 13, 1330.
- [92] C. Flox, M. Skoumal, J. Rubio-Garcia, T. Andreu, J. R. Morante, *Appl. Energy* **2013**, 109, 344.
- [93] a) H.-M. Tsai, S.-J. Yang, C.-C. M. Ma, X. Xie, *Electrochim. Acta* **2012**, 77, 232; b) S. Jeong, S. Kim, Y. Kwon, *Electrochim. Acta* **2013**, 114, 439; c) T.-M. Tseng, R.-H. Huang, C.-Y. Huang, K.-L. Hsueh, F.-S. Shieu, *J. Electrochem. Soc.* **2013**, 160, A690.
- [94] a) K. J. Kim, M.-S. Park, J.-H. Kim, U. Hwang, N. J. Lee, G. Jeong, Y.-J. Kim, *Chem. Commun.* **2012**, 48, 5455; b) B. Li, M. Gu, Z. Nie, X. Wei, C. Wang, V. Sprenkle, W. Wang, *Nano Lett.* **2014**, 14, 158.
- [95] M. Park, J. Ryu, J. Cho, *Chem. Asian J.* **2015**, 10, 2096.
- [96] R. S. Nicholson, *Anal. Chem.* **1965**, 37, 1351.
- [97] a) D. Menshykau, R. G. Compton, *Electroanalysis* **2008**, 20, 2387; b) C. Punckt, M. A. Pope, I. A. Aksay, *J. Phys. Chem. C* **2013**, 117, 16076.
- [98] L. Cao, M. Skyllas-Kazacos, D.-W. Wang, *J. Electrochem. Soc.* **2016**, 163, A1164.
- [99] M.-A. Goulet, M. Eikerling, E. Kjeang, *Electrochem. Commun.* **2015**, 57, 14.
- [100] M. Becker, N. Bredemeyer, N. Tenhumberg, T. Turek, *Electrochim. Acta* **2017**, 252, 12.
- [101] E. Kjeang, R. Michel, D. A. Harrington, N. Djilali, D. Sinton, *J. Am. Chem. Soc.* **2008**, 130, 4000.
- [102] D. Aaron, C.-N. Sun, M. Bright, A. B. Papandrew, M. M. Mench, T. A. Zawodzinski, *ECS Electrochem. Lett.* **2012**, 2, A29.
- [103] C.-N. Sun, F. M. Delnick, D. S. Aaron, A. B. Papandrew, M. M. Mench, T. A. Zawodzinski, *ECS Electrochem. Lett.* **2013**, 2, A43.

## 2 Scope of the thesis

The main objective of this thesis was the development of new methods for the characterization of materials, which can be used as electrodes in prominent electrochemical converter systems. The developed methods should help to understand electrode processes, identify relevant structures or morphological issues as well as structural changes in detail and should finally contribute to the search for new materials with enhanced properties towards selected electrochemical reactions. Among a broad variety of electrochemical methods, the scanning electrochemical microscopy (SECM) was chosen since it is the one and only technique which allows for spatially resolved electrochemical information of an electrode. Additionally, a complementary spectroscopic technique or a coupling to realize an *in situ* probing in parallel was of particular interest in this work. Here, Raman microscopy was chosen, which yields information on structures and structural changes and can be preferably applied to electrochemical systems. In order to gain deeper insights into materials structures and processes, the developed methods shall be applied to relevant electrochemical reactions and materials which occur in electrochemical energy storage processes.

Two main issues turned out regarding the challenge of electrochemical energy storage question: On the one hand, the oxygen evolution reaction (OER) which can be found at the anode of water electrolyzer systems but also in metal-air batteries. This reaction is of particular importance when hydrogen should be used as storage molecule. Here, reaction steps, pathways and adsorbates are not fully understood up to now which explains the need for advanced characterization techniques. Especially in alkaline media, transition metal oxides are in the focus of research because they are relatively cheap, exhibit high OER activity and can be synthesized in various structures and morphologies. On the other hand, redox flow batteries are discussed as an important storage system for fluctuating wind and photovoltaic energy. In this type of electrochemical converters, the reaction at the positive pole of the accumulator is supposed to be the limiting reaction of the system. Carbon-based electrodes with well-known structural, morphological and electrochemical properties may solve this issue and can help to improve the efficiency of the battery system.

### 3 Summary and outlook

The development of advanced methods for a spatially resolved electrochemical technique, the scanning electrochemical microscopy, and its application towards energy materials which may be analyzed towards electrochemical activity, stability and selectivity was the scope of the thesis. The results of the present work can be divided into three main parts where the first part deals with the setup and the application of an instrument which combines SECM with Raman microscopy as a micro-spectroelectrochemical tool. The second part shows how the combination of complementary surface characterization techniques can help to explain macroscopic behavior of graphite containing sol-gel electrodes for the antifouling purpose in marine application. Finally, the third part which contains three individual studies shows the development of a SECM procedure for the characterization of electrocatalysts towards vanadium(IV) oxidation. Functionalized high-purity carbon nanotubes were comprehensively characterized and studied with the prior developed SECM method.

In the first part, an instrumental coupling of SECM and Raman microscopy is shown which can be used for *in situ* spectroelectrochemical studies. For this purpose, an SECM instrument was mounted on an inverted Raman microscope which allows for SECM experiments from the top and Raman probing from the backside of the electrochemical cell in parallel. This instrumental arrangement requires a transparent conductive substrate electrode as for example indium-doped tin oxide (ITO) on quartz glass. In a first study, nickel and nickel/iron thin films were analyzed towards oxygen evolution reaction (OER) in alkaline media (pH = 13). Nickel thin film electrodes with iron contents ranging from 0 % to 30 % were prepared onto the optical transparent electrode by electrodeposition from pure or mixed metal salt solutions. These thin films of 20 to 50 nm in thickness were investigated by a chrono amperometric procedure with increasing potential steps starting from 0.1 V vs. Hg|HgO|1 M KOH up to potentials in the oxygen evolution region (> 0.55 V). During each potential step the platinum microelectrode probes the oxygen evolution by reducing evolved oxygen (SG/TC mode) and a Raman spectrum was recorded in parallel at the very same position. Regarding the electrochemical results, the thin film electrodes with iron content < 22 % showed Ni(II) to Ni(III) oxidation which merges inseparably with the OER. The additional microelectrode probing from SECM allows to distinguish between both and enables to determine the OER *onset* potentials which reflect the apparent beginning of the gas evolution. The lowest one was found at the 15 % iron containing sample. The additional spectroscopic data shows that the Ni(II) to Ni(III) oxidation is connected with the formation of a  $\gamma$ -Ni<sup>III</sup>OOH which can be concluded from the appearance of two

prominent bands at 475 and 557  $\text{cm}^{-1}$ . The appearance of both bands shifts to higher potentials with increased iron content which is in accordance to the electrochemical peak shift. The intensity ratio ( $I_{475}/I_{557}$ ) of both bands decreases with increasing iron content as a result of a disturbed lattice by disorder introduced from iron atoms. From the complementary data it can be concluded that  $\gamma\text{-Ni}^{\text{III}}\text{OOH}$  always has to be present before the OER *onset* potential is reached but its presence alone is not sufficient. Further linear sweep voltammetric experiments ( $1 \text{ mV s}^{-1}$ ) obtained in the very same experimental configuration suggest that even during NiOOH formation oxygen species might be evolved which is concluded from slight reduction currents at the microelectrode in the respective potential region.

In the second part, SECM and Raman microscopy are used as individual techniques to characterize the surface of graphite sol-gel composite electrodes with a possible application in electrochemical antifouling. These electrodes were prepared by mixing a commercial sol-gel lacquer with conductive graphite particles to form a paintable conductive coating. An optimum composition was found in the sample with 20 wt.% graphite in the coating that offers a good balance between sufficient conductivity, stability and surface morphology. This sample was examined by Raman microscopy to analyze the surface structure and composition. As expected, graphite components were identified by a weak D and a strong G band at 1352 and 1584  $\text{cm}^{-1}$  in the Raman spectrum. A mapping experiment shows the distribution of graphite in the coating. The lacquer component only contributed with fluorescence signals in the respective wavenumber region. Evaluating this mapping data, it can be concluded that the graphite forms agglomerates ranging from a few micrometers up to several tens of micrometers in size which is in accordance with results from light microscopy. In a subsequent experiment, the very same region of the sample was examined by SECM using a feedback experiment with a 10  $\mu\text{m}$  platinum microelectrode and ferricyanide ions as redox mediator. The SECM image shows a surface conductivity map with a few regions of positive feedback which can be attributed to the conductive graphite agglomerates and many regions with negative or mixed feedback response which is the result of the insulating lacquer. Different behavior of individual positions on the sample were also found in approach curve experiments. Comparing the conductivity map to the prior obtained component distribution map, it can be stated that not all regions where graphite particles or agglomerates that were detected by the Raman mapping experiment contribute equally to the surface conductivity. Individual particles seem to be insulated by thin lacquer layers or exhibit a low electron transfer rate in the feedback experiment which results in a negative feedback. To approach conditions which comes close to the later technical use of the

electrodes, another SECM experiment of the very same region of the sample in 1 M KCl (pH = 8), which was used to mimic seawater, was carried out. In this SECM experiment (SG/TC mode), the sample was polarized to high positive potentials where gas evolution reactions for chlorine (CER) and oxygen (OER) can be observed. The microelectrode was scanned along the sample with an applied potential detecting either chlorine or both, chlorine and oxygen. All potentials were evaluated by cyclic voltammetry (CV) under identical conditions prior to the SECM experiment. These experiments again resulted in SECM images which show the spatially resolved evolution of the gases at the sample surface. Sharp and highly reproducible contours in the images indicate active regions of both gas evolution reactions which can be correlated to positions with high graphite content detected in the first set of experiments. They also show that the gases diffuse along the surface which act as antifouling agents and may hinder the settlement of microorganisms in technical use.

In the third part, a competitive mode of SECM was developed by applying a linear sweep voltammetric (LSV) procedure to the microelectrode which may help to understand the vanadium(IV)/(V) redox reaction at the positive pole of the all-vanadium redox flow battery (VRFB). A model solution consisting of 10 mM  $\text{VO}^{2+}$  as vanadium(IV) source and a 0.5 M  $\text{HSO}_4^-/\text{SO}_4^{2-}$  buffer (pH = 2) was used and the suggested procedure was evaluated using a glassy carbon substrate (GC) as sample. A linear sweep between 0.8 and 1.4 V vs.  $\text{Ag}|\text{AgCl}|\text{KCl}_{\text{sat.}}$  at the microelectrode results in an oxidative current which cannot be found in a  $\text{VO}^{2+}$  free solution. This procedure was chosen as detection sweep to probe  $\text{VO}^{2+}$  ions because constant potentials or potential pulse experiments showed strong deactivation behavior of the microelectrode response. Conversely, the linear sweep procedure results in a constant response after several equilibration sweeps. The microelectrode in close distance to the GC substrate can be used to set up a competitive experiment. Increasing the potential at the substrate results in a decrease of the current during the LSV at the microelectrode if the substrate consumes the  $\text{VO}^{2+}$  ions by oxidation. Using small potential steps (10 mV  $\text{step}^{-1}$ ) a consumption curve of the  $\text{VO}^{2+}$  ions by the substrate electrode can be obtained. In this curve an *onset* potential, the apparent beginning of ion conversion, becomes determinable. This method provides an alternative to other often used methods (i.e. CV) for the comparison of different materials with respect to  $\text{VO}^{2+}$  oxidation activity. To demonstrate this, well-defined high-purity carbon nanotubes (CNT) were synthesized and intensively characterized by various means of surface and bulk characterization techniques. Different oxidation means together with a microwave-assisted treatment were used to introduce different amounts of oxygen containing functional groups into the CNT material.

X-ray photoelectron spectroscopy (XPS) analysis showed oxygen contents from 0.4 at.% in the raw material up to 8.0 at.% as well as the contribution of single and double C-O bonds by evaluating the O 1s peak which can be assigned to different types of surface groups. Surface area determination showed an increase of the mass specific surface area with increasing oxygen content. Electrochemical characterization by CV showed increased double layer capacity (DLC) with increased oxygen content as well as the appearance of redox peaks from pseudo capacities attributed to quinone-type surface groups. These well-defined CNT samples were analyzed by the competitive SECM procedure to evaluate the contribution of oxygen-containing surface groups towards the  $\text{VO}^{2+}$  oxidation. Here, again the *onset* potential was used as a kinetic parameter to compare all samples. From this experiment it can be concluded that from 0.4 at% to 3.2 at.% oxygen the *onset* potential of the  $\text{VO}^{2+}$  oxidation strongly shifts (~200 mV) to lower potentials which indicates an improved electrochemical reaction. From 3.2 at.% to 8.0 at.% oxygen in the sample surface the improvement is considerably smaller (~30 mV). In this model solution, oxygen containing surface groups obviously do not contribute to the electrochemical  $\text{VO}^{2+}$  oxidation. The strong effect at the low-oxygen samples seems to be more or less a result of surface availability by wetting. A certain amount of oxygen functional groups are necessary so that the aqueous solution can access the whole porous carbon structure.

From all these results, lots of experiments for a further continuation of this work may be suggested. In the following, some ideas will be put forward which can be categorized into instrumental and material aspects. The Raman-SECM instrument can be used to study a variety of materials in terms of structural changes and related electrochemical activity. As Raman spectroscopy may be used as surfaces sensitive technique as in SERS, it would be necessary to introduce samples which contain metal particles that provide high SERS enhancement (Ag, Au). These materials can be added by dropcasting onto the transparent electrode or even by co-deposition from mixed metal salt solutions. Electrochemically inert substrates can be achieved by addition of Au particles with a thin insulating silica shell (SHINERS). Beside the addition of a SERS active substrate, the enhancement of a single tip with a curved half sphere can also be used to create surface sensitivity (TERS). Here, the instrumentation already allows the installation of a TERS-tip instead of the microelectrode. The development of a TERS-tip which also serves as microelectrode would create a powerful surface sensitive *in situ* instrument. Indium-doped tin oxide (ITO) on quartz glass is used as a transparent electrode material in a broad variety of applications. However, graphene on glass which is still sufficiently transparent is a possibility to avoid ITO and would extend the usability to harsher conditions. Concerning the



material aspects, it can be stated that especially in case of OER of nickel oxide not all aspects of structure, phases and electrochemical activity are fully understood up to now. The influence of impurities and the introduction of structural defects needs to be studied in more detail with further surface and bulk characterization techniques. Finally, carbon materials still offer a broad suitability and application potential in electrochemistry. Synthesizing well-defined materials with controlled structure and surface morphology must be a long-term goal in this field.

## 4 A Raman-coupled scanning electrochemical microscope setup

*The content of this part has been published as*

***In situ* characterization of Ni and Ni/Fe thin film electrodes for oxygen evolution in alkaline media by a Raman-coupled scanning electrochemical microscope setup**

*Reprinted with permission from M. Steimecke, G. Seiffarth, M. Bron, Analytical chemistry 2017, 89, 10679-10686. Copyright 2017 American Chemical Society.*

**DOI: 10.1021/acs.analchem.7b01060**

Abstract

We present a spectroelectrochemical setup, in which Raman microscopy is combined with scanning electrochemical microscopy (SECM) in order to provide both spectroscopic and electrochemical information on the very same location of an electrode at the same time. The setup is applied to a subject of high academic and practical interest, namely, the oxygen evolution reaction at Ni and Ni/Fe electrodes. It comprises a transparent substrate electrode, onto which Ni and Ni/Fe thin films are deposited. An ultramicroelectrode (UME) is placed closely above the substrate to obtain electrochemical information, while a Raman microscope probes the same sample spot from below. To obtain information on oxygen evolution activity and structural changes, increasingly positive potentials from 0.1 up to 0.7 V vs Hg|HgO|1 M KOH were applied to the Ni/Fe-electrodes in 0.1 M KOH solution. Evolved oxygen is detected by reduction at a Pt UME, allowing for the determination of *onset* potentials, while the substrate current, which is recorded in parallel, is due to both overlapping oxygen evolution and the oxidation of Ni(OH)<sub>2</sub> to NiOOH. An optimum of 15 % Fe in Ni/Fe films with respect to oxygen evolution activity was determined. At the same time, the potential dependent formation of  $\gamma$ -NiOOH characterized by the Raman double band at 475 and 557 cm<sup>-1</sup> allows for the conclusion that a certain amount of disorder introduced by Fe atoms is necessary to obtain high oxygen evolution reaction (OER) activity.

## 4.1 Introduction

The growing need for suitable systems for energy storage has triggered substantial research and development efforts in the field of electrochemical energy conversion and in particular in electrocatalysis, for instance for fuel cell and electrolyzer systems. One important issue is to develop highly active, stable and preferably cheap catalyst materials, and tremendous progress has been achieved in this field during the last decade.<sup>1-4</sup> While practical approaches to this subject often rely on phenomenological descriptions, more sophisticated strategies try to establish structure-activity relationships based on a thorough spectroscopic and electrochemical characterization of a series of materials. However, it is a well-known fact from catalysis and electrocatalysis research that catalyst materials change during operation.<sup>5,6</sup> Thus, to fully understand the behavior of electrocatalysts, *in situ* studies are necessary to unravel structural changes and concomitant changes in activity of the material under investigation to complement the above-mentioned approaches. Indeed, a broad variety of techniques, including X-ray diffraction,<sup>7</sup> X-ray absorption,<sup>8,9</sup> X-ray photoelectron,<sup>10</sup> infrared (IR),<sup>11</sup> and Raman spectroscopy,<sup>12</sup> were successfully applied to the *in situ* study of electrocatalysts. Although these techniques provide indispensable information on structure, structural changes and resulting electrochemical performance of catalysts, it might be considered a drawback that spectroscopic information is typically obtained from a certain location of the electrode, while the electrochemical experiment probes the whole sample.

One important technique to obtain localized (electro)chemical information is scanning electrochemical microscopy (SECM)<sup>13</sup> which can be considered a true chemical microscopy. SECM has been applied to a variety of research fields such as material science, corrosion, biology, electrocatalysis, and fuel cells.<sup>14-16</sup> Micrometer and sub-micrometer electrodes allow for spatially resolved electrochemical experiments at surfaces of a broad variety of materials. In catalysis research SECM may be used as a fast method to screen the activity of a number of samples with different compositions while varying selected parameters such as applied potential, electrolyte or reactants, which finally allows for an easy evaluation and comparison of the investigated materials.<sup>17</sup> SECM as a spatially resolving technique is typically used to probe larger electrocatalyst surfaces towards activity distribution and may for instance unravel “hot spots” in activity of an apparently homogeneous film.<sup>18,19</sup>

In the sense, combining an *in situ* spectroscopic method with SECM may provide information on material changes, intermediates or oxidation states together with *local* electrochemical

performance of an electrode under operation at the same time. A broad variety of techniques has been combined with SECM, e.g., atomic force microscopy<sup>20-22</sup> or scanning tunneling microscopy.<sup>23</sup> Furthermore, SECM combined with attenuated total reflection-IR spectroscopy was described<sup>24</sup> as well as Raman microscopy with shearforce regulated SECM.<sup>25</sup>

In this study we present a *in situ* Raman-SECM instrument which combines the advantages of SECM towards localized electrochemical and electrocatalytic characterization of microstructures with the potential of Raman microscopy to provide a simultaneous spectroscopic characterization at the very same electrode spot. Raman spectroscopy as a non-invasive, non-destructive technique is used in a wide range of research areas to obtain structural information about single molecules, polymers, rocks, metal oxides, etc. In particular, it is not impeded by water as solvent. As a result Raman spectroscopy can be used as an *in situ* technique in electrochemistry research. Among the various approaches, surface enhanced Raman spectroscopy (SERS) using the coinage metals as substrate electrodes has been used for studying metal-molecule interactions such as adsorption/desorption processes, bonding states, or reaction intermediates.<sup>12,26</sup> Kurouski *et al.* demonstrated electrochemical-tip enhanced Raman spectroscopy (TERS), where the TERS tip providing Raman enhancement is used as electrode in an electrochemical experiment at the same time.<sup>27</sup>

In contrast to published setups, our approach uses a classical and well established SECM experiment, which is however extended by an inverted Raman microscope coupled into the cell from the backside of a transparent electrode. To highlight the performance of the developed coupled system electrochemically deposited Ni and Ni/Fe thin film electrodes on an ITO-coated quartz glass substrate were investigated towards their activity for oxygen evolution reaction (OER) in alkaline media and concomitantly occurring structural changes.

Ni/Fe electrodes are known as cheap and long term stable materials with reasonable activity for OER to be used in alkaline electrolysis.<sup>1,28</sup> A wide range of methods were applied to study Ni<sup>29</sup> and Ni/Fe<sup>30</sup> OER catalysts focusing on a better understanding of structural properties and related catalytic activities. Raman spectroscopy was used for Ni<sup>31-33</sup> and Ni/Fe<sup>34</sup> based systems in order to determine the active phase during the catalytic process including effects of material aging. The appearance of NiOOH was found to be essential for high activity towards the OER at these materials which was often attributed to its  $\beta$ -phase.<sup>31,33</sup> However, recent results suggests that Fe impurities (often from the electrolyte) are the reason of enhanced OER activity of nickel oxide/hydroxide films.<sup>35,36</sup> In low iron samples (< 25%) the presence of Fe<sup>3+</sup> in  $\gamma$ -Ni<sub>1-x</sub>Fe<sub>x</sub>OOH

seems to be important to obtain low overpotentials,<sup>37</sup> *operando* Mössbauer spectroscopic studies even suggest the presence of Fe<sup>4+</sup> in the active Fe-doped NiOOH.<sup>38</sup>

When studying Ni-based catalysts for their OER activity, classical electrochemical methods such as linear sweep (LSV) or cyclic voltammetry (CV) often do not allow reliable differentiation between the oxidation of Ni<sup>II</sup> to Ni<sup>III</sup> and the *apparent* beginning of the OER (commonly named as *onset* potential) especially at bare Ni or highly Ni-containing compounds. Using an UME in the close distance of a catalytically active film and employing the sample generation/tip collection mode (SG/TC) of SECM can improve the determination of this often-used parameter.<sup>39,40</sup> For iridium, ruthenium oxide, and perovskite based systems, this experimental approach was successfully applied to determine the real *onset* potential (in the sense mentioned above) of the catalyst films.<sup>41,42</sup> SECM can also be used to determine the *onset* potential of bifunctional catalyst for both OER and ORR in one experiment<sup>39,43</sup> as well as for other important electrochemical reactions.<sup>44</sup>

This paper will show that the developed Raman-SECM instrument is capable of both resolving the structure of the nickel oxide/hydroxide in Ni or Ni/Fe thin film electrodes by *in situ* Raman spectroscopy as well as determining the apparent *onset* of OER using the SG/TC mode of SECM at the same time and at the same location of the electrode. The setup however is not restricted to this or similar problems but may in the future be extended to other relevant challenges in electrocatalysis research.

## 4.2 Experimental section

### 4.2.1 Chemicals and materials

Commercially available indium-doped tin oxide (ITO) coated on quartz glass with a resistance of  $20 \Omega \text{ cm}^{-1}$  (PräzisionsGlas&Optik, pgo Iserlohn, Germany) was used as the optical transparent electrode substrate (OTE) for Ni and Fe/Ni thin film preparation. Prior to use, the OTE was cleaned with water, ethanol, and acetone and dried in air. Nickel sulfate (99.99%) and iron sulfate (99.99%, both Carl Roth GmbH, Karlsruhe, Germany) were used as metal sources for the electrochemical deposition. Potassium hydroxide (ROTI@METRIC, 99.98%, batch: 404218656, Carl Roth GmbH, Germany) containing  $< 2 \text{ ppm Fe}$  was used to prepare 0.1 M KOH. In addition, a nickel film electrode was also studied in 0.1 M KOH purified by a procedure to remove any residual Fe traces as reported in the reference.<sup>36</sup> Deionized water ( $< 0.055 \mu\text{S cm}^{-1}$ ) supplied by a system from SGWater was used for the preparation of all solutions and for cleaning of materials.

### 4.2.2 Preparation of Ni and Ni/Fe thin film electrodes and metal analysis

After cleaning as described above, most of the conductive substrate of the OTE was covered with transparent tape ( $\sim 50 \mu\text{m}$  in thickness) and only a hole of 5 mm in diameter ( $0.196 \text{ cm}^2$ ) remained open. For thin film electrodeposition a chrono-potentiometric method was used as described in the reference.<sup>34</sup> Briefly, a 10 mM metal sulfate solution either containing Ni or Ni/Fe in the respective composition was used and a cathodic current of  $50 \mu\text{A cm}^{-2}$  was applied for a period of 1000 s to the substrate. The compositions of the respective thin films were determined after the electrochemical experiments described later using inductively coupled plasma with optical emission spectrometry (ICP-OES, Plasmaquant 110). For this purpose, all samples on the OTE were dissolved in 5 mL of concentrated  $\text{HNO}_3$  (Carl Roth GmbH) by treatment in an ultrasonification bath (Sonorex) for 30 min. The OTE made from ITO on quartz glass and partly covered with a Ni or Ni/Fe thin film will be labeled as a thin film electrode in the following.

### **4.2.3 Scanning electron microscopy (SEM)**

Scanning electron micrographs were obtained with a Versa 3D microscope (SEI). To determine the thickness of the films a Pt layer was deposited on top of the sample. Afterwards, the layers were cut with a focused ion beam (FIB) and the individual layer thickness was analyzed.

### **4.2.4 Raman-SECM instrumentation**

A modified scanning electrochemical microscope (Sensolytics, Bochum, Germany) consisting of a stepper motor and a piezo cube for z positioning (position resolution 10 nm) and manual steppers for x,y positioning is installed on top of an inverted confocal microscope DM 2500 (Leica, Wetzlar, Germany). The microscope is equipped with a x,y stage (Prior Scientific) and a MS-10 stage controller (Renishaw) providing a position resolution of 0.5  $\mu\text{m}$  and connected to an InVia Raman spectrometer (Renishaw). Laser excitation was 532 nm with a grating of 1800  $\text{l mm}^{-1}$ . Long working distance objectives (Leica, Wetzlar, Germany) were used with a magnification of x50. The scattered light was collected by the objective and directed to a tuneable grating and then to a Peltier cooled charge coupled device (CCD). Prior to use, the Raman spectrometer was calibrated to a silicon reference band and the signal adjusted to 520.4  $\text{cm}^{-1}$ . Further details on this setup and its application can be found in the results and discussion section.

### **4.2.5 Electrochemical and spectroelectrochemical experiments**

Electrochemical measurements were performed using an in-house constructed cell with an Hg|HgO|1M KOH reference electrode (RE, Forschungsinstitut Meinsberg, Germany), a Pt wire (Goodfellow) as counter (CE), and a 25  $\mu\text{m}$  Pt ultramicroelectrode (UME,  $R_G = 10$ , Sensolytics) as one working electrode. The thin film electrode was electrically contacted by a flat silver ring realizing a homogeneous conductivity over the substrate and was used as a further working electrode (WE 1) during the experiments. The term “WE 1” refers to the connection port of an Autolab bipotentiostat PGSTAT 128N (Metrohm) which was employed to perform all electrochemical experiments. The UME always served as a second working electrode.

Coupling between bipotentiostat and WiRE 3.3 Raman instrument software (Renishaw) was realized by scripted SECM software (Sensolytics) or Nova 1.9 software (Metrohm) allowing for stage position controlling and changing, Raman single measurement execution, and data

saving at each potential. Combination of the single point measurement data sets to lines or arrays would be possible as well.

The electrochemical cell was filled with 0.1 M KOH electrolyte and equipped with the thin film electrode at the bottom as well as with the RE, CE, and UME. CVs of the UME were recorded between -0.6 and 0.4 V vs. Hg|HgO|1 M KOH until a stable response was observed. Then a potential of -0.6 V was applied until a constant current response resulting from the reduction of dissolved oxygen from air was observed, which was usually the case after 10 min. With this potential applied to the UME, an approach curve was performed towards the thin film electrode to establish the suitable working distance, which was set as the distance where the UME current decreases by about 25 % of its initial value. This UME approach was monitored with the inverted microscope and absolute distances of 20 – 30  $\mu\text{m}$  between thin film electrode and UME were determined.

Afterwards chrono-amperometry (CA) with discrete potential steps from 0.1 to 0.7 V vs. Hg|HgO|1 M KOH was applied to the thin film electrode (WE 1) with 100  $\text{mV step}^{-1}$  between 0.1 and 0.4 and 10  $\text{mV step}^{-1}$  between 0.4 and 0.7 V vs. Hg|HgO|1 M KOH while the potential of -0.6 V was still applied to the UME. Each potential was held for 30 s for equilibration and the current at both the thin film electrode and UME were recorded simultaneously. For data evaluation, the last current values of the equilibration time were taken. The execution of the single Raman measurement followed while all potentials were still applied. During this time, the current changes were negligibly small. After finishing the Raman measurement, the next potential was applied to the thin film electrode. In some cases the experiment had to be stopped before reaching 0.7 V because of the observed high current density at the UME and concomitant bubble formation (presumably oxygen) at the thin film electrode that impedes the continuation of the experiment. The obtained Raman spectra were background corrected by subtracting the spectrum recorded at OCP at the very same position of the thin film. In a control experiment, a bare ITO-coated quartz glass electrode was exposed to the same experimental conditions and no changes in the obtained spectra were observed while the electrochemical procedure was applied.

Subsequently to the described spectroelectrochemical procedure, linear sweep voltammograms (LSV) were recorded from 0.1 to 0.7 V vs. Hg|HgO|1 M KOH with a scan rate of 1  $\text{mV s}^{-1}$  whereby again a potential of -0.6 V was applied to the UME. CV was further used to



characterize the thin film electrodes between 0.0 and 0.65 V with scan rates of 5, 10, 20, and 50 mV s<sup>-1</sup> without recording the UME response.

## 4.3 Results and discussion

### 4.3.1 System design

While the technical description of the novel setup was given in the experimental part, the following section will highlight the general thoughts behind the development. As mentioned, one important aspect is that we chose a geometry where an opposite arrangement of UME and Raman microscopy is used to probe a sample deposited onto a transparent electrode employing SECM and Raman microscopy. This arrangement allows keeping the typical SECM geometry unchanged. In particular, the limited space around the UME may hinder the simultaneous probing with a second (e.g., spectroscopic) technique due to the geometry of the insulating glass body around the UME and the low sample to UME distance which is in the order of the UME metal diameter. This advantage certainly comes at the disadvantage that optically transparent electrodes have to be used to be able to couple in the Raman laser light from below the sample.

The setup is designed in a way that the electrochemical microscope is mounted on top of an inverted microscope (i.e., at a position which is usually used for the installation of a light source). The inverted microscope may simply be used as an optical microscope, as shown in our previous work.<sup>43,44</sup> However, when coupled to a Raman spectrometer, the resulting Raman microscope may be used to obtain spectroscopic information of the sample under investigation (Figures 1a and 2a).

Although standard SECM measurements are possible with this setup, certainly for the simultaneous spectroelectrochemical measurements the focus of the Raman microscope and the position of the UME should be fixed to each other. The manual stepper screws at the SECM allow an easy and precise positioning of the UME in x and y direction into the desired position, which is typically above the sample spot which is in the focus of the Raman microscope. On the other hand, the electrochemical cell is placed on the 2D-moveable stage of the Raman microscope, allowing for position change via software control. Thus, mapping experiments would in principle be possible; however, different to classical SECM experiments, it is not the UME which is moved across the sample, but the substrate would be moved in x and y direction while keeping the focus of the Raman microscope and the UME at the same position. Figure 1a represents the schematic setup of the electrochemical cell with UME above the focus area of the microscope, reference (RE) and counter (CE) as well as the working electrode (WE1), which is the transparent thin film electrode at the bottom of the cell. Figure 1b shows a picture of the installed system mounted onto the inverted microscope.

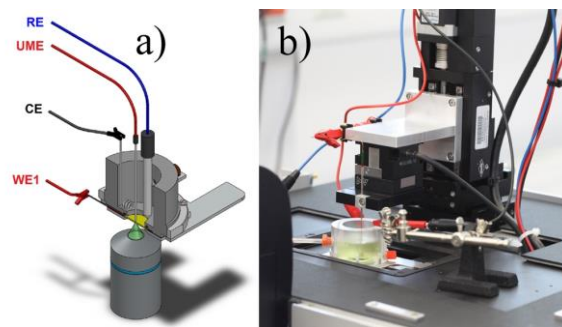


Figure 1: Developed setup for the *in situ* measurements. Schematic representation with UME, ultramicroelectrode; WE 1, working electrode (here: thin film electrode); RE, reference electrode; CE, counter electrode; and Raman microscope from below (a) and a picture of the installed SECM instrument (b).

### 4.3.2 Ni and Ni/Fe thin film electrodes for the oxygen evolution reaction (OER)

Ni and Ni/Fe thin film electrodes were prepared by electrodeposition. A constant cathodic current of  $50 \mu\text{A cm}^{-2}$  was applied to the ITO-coated transparent electrodes in the respective 10 mM metal salt solutions for a defined time. Deposition curves of all samples can be found in Figure S1a of the supporting information together with their cyclic voltammograms (Figure S1b). The Ni/Fe ratio of the mixed thin film electrodes depends on the concentration ratio of the used metal salts in the deposition solution. However, the exact composition of the films differs strongly from that in solution as also reported by Louie *et al.*<sup>34</sup> To determine the composition of the deposited films ICP-OES analysis was carried out for all samples after the spectroelectrochemical experiments. As summarized in Table S1 the amounts of Fe are 3-7 times higher than the composition of the deposition solution. The ICP-OES analyses were carried out after all electrochemical experiments in 2 ppm Fe-containing KOH, which provides an additional contribution to the overall Fe content in the samples. This becomes particularly obvious for the Ni-only film in which 6% Fe was found although there was no Fe added to the deposition solution. To study the effect of Fe, nickel electrodes with Fe contents between 0 and 30% were used for the experiments. Note that these and all following values for the Fe content refer to the experimentally determined ones (see above). It was excluded that the OTE material itself contributes to the amount of Fe. Further morphological characterization by scanning electron microscopy showed film thicknesses  $< 50 \text{ nm}$  for all samples (Figure S2).

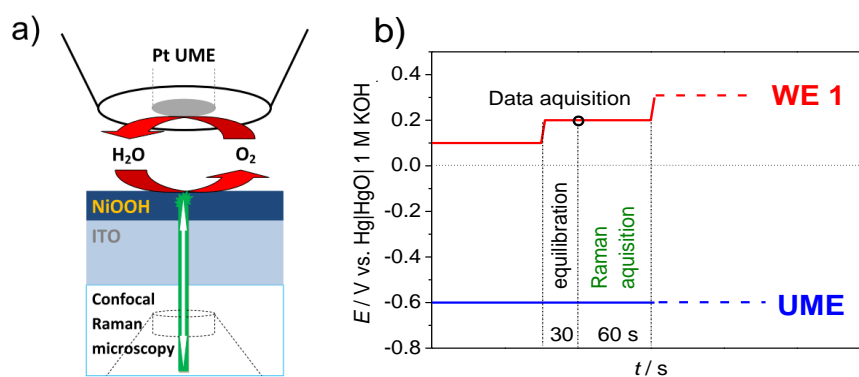


Figure 2: Scheme of the sample generation-tip collection (SG/TC) mode of SECM with additional Raman data acquisition (a) and the potential profile where the UME is held at a constant potential (-0.6 V) while the sample electrode (WE1) is modulated with discrete potential steps in positive direction (b).

For the determination of oxygen evolution activity, the sample generation/tip collection (SG/TC) mode was chosen. Here, the Pt ultramicroelectrode is working to the thin film electrode and is polarized to a potential of -0.6 V. A constant cathodic current is observed, which results from air/oxygen dissolved in the potassium hydroxide solution. The current at the UME will increase as soon as additional oxygen is evolved by the thin film. The thin film electrode potential is increased stepwise, while a Raman spectrum is recorded at every potential together with the UME and thin film electrode current. The scheme of the experimental setup can be found in Figure 2a while the potential profile applied to UME and thin film electrode (WE1) is shown in Figure 2b.

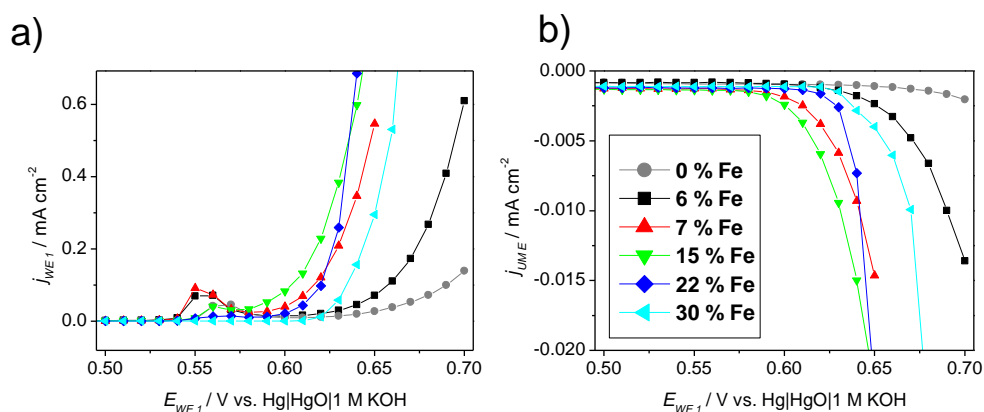


Figure 3: Current densities measured at the thin film electrodes (a) and corresponding UME response at -0.6 V for oxygen detection (b) during chrono-amperometric experiments in 0.1 M KOH; the data represents the last value after holding the respective substrate potential for 30 s as displayed in Figure 2a. All measurements were performed in solutions of commercial KOH with the exception of the Ni-only thin film electrode (0% Fe) measured in purified KOH solution; lines connecting the data points are intended as a help for the eye.

The electrochemical results obtained during spectroelectrochemical measurements are summarized in Figure 3. In Figure 3a the currents measured at the thin film electrodes in dependence of the applied substrate potential ( $E_{WE1}$ ) are displayed. The corresponding currents

measured at the UME are shown in Figure 3b. By increasing the substrate potential in the positive direction, an anodic current between 0.53 and 0.6 V can be observed at those samples containing a low iron amount (6 and 7% Fe). This current is lower at the 15% Fe sample and vanishes at the 22 and 30% samples. The observed current results from the Ni(OH)<sub>2</sub> to NiOOH oxidation<sup>45,46</sup> that is known to shift to more positive potentials with higher iron content.<sup>47,29</sup> In the literature, electrochemical and iodometric analysis of the NiOOH showed oxidation states  $> 3.67^{48}$  which indicates a number of transferred electrons  $> 1$  during the redox process.<sup>34</sup> In general, the area of the redox peaks decrease with increasing iron content, as also visible in CVs (cf. Figure S1b). At more positive potentials the evolution of oxygen starts, indicated by a strong increase of the current at  $E_{WEI} > 0.57$  V. Obviously both the oxygen evolution and the Ni<sup>II</sup> oxidation overlap each other, impeding the determination of *onset* potentials. However, at more positive potentials, a differentiation between the samples is possible and the samples with 7, 15, and 22% Fe showing the highest currents at 0.63 V, while the lowest current can be found at the nickel-only electrode in iron-free KOH solution which is in accordance with the literature.<sup>36</sup> The results of the corresponding measurements at the microelectrode in a close distance to the electrode thin film illustrate that the chosen setup can provide additional information about the OER while not being affected by redox transitions at the thin film electrode (Figure 3b). In all cases, a negative current appears depending on the applied potential which is caused by the reduction of oxygen evolved at the thin film electrode. From these corresponding curves the *onset* potentials for the OER can be determined with higher precision. The *onset* potential was defined as the potential where the current density at the microelectrode changes by more than 20% compared to the preceding quasi-linear region ( $< 0.59$  V) and are displayed in Table 1.

Table 1: Onset potentials from Figure 3<sup>a</sup>.

<b>sample</b>	<b><math>E_{onset} / \text{V}</math></b>
Ni (Fe free)	0.68
6 % Fe	0.63
7 % Fe	0.60
15 % Fe	0.59
22 % Fe	0.62
30 % Fe	0.63

<sup>a</sup>Potentials are referred to a Hg|HgO|1 M KOH reference electrode.

Raman spectra were recorded at each potential, at which the electrochemical data displayed in Figure 3 were obtained. Background corrected *in situ* Raman spectra of selected thin film

samples (6% and 22% Fe) in dependence of the applied potential are shown in Figure 4. Spectra of the other samples are summarized in Figure S4 in the supporting information. Reference experiments demonstrating the negligible influence of the ITO on the current responses as well as on the Raman spectrum can be found in Figure S3a and S5 and in the supporting information text.

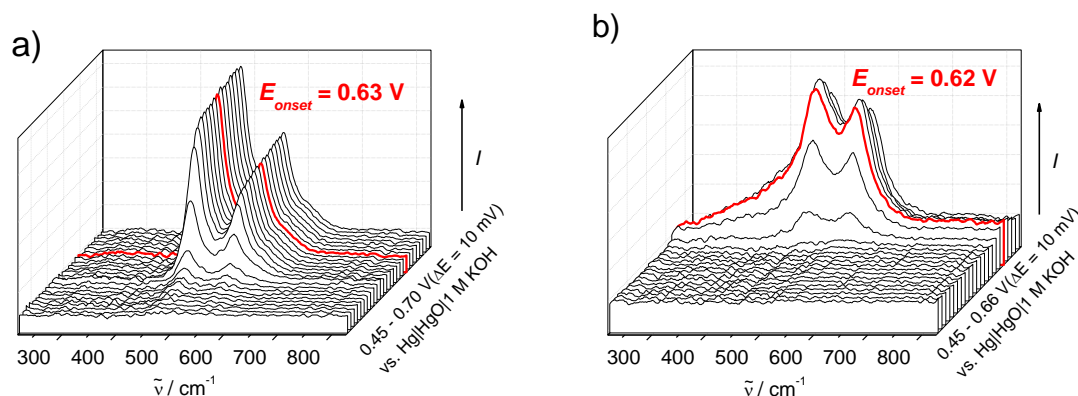


Figure 4: *In situ* Raman spectra of Ni thin film electrodes containing 6% (a) and 22% Fe (b) in dependence of the applied potential. All spectra are background corrected by subtracting the initial spectrum at OCP, and the determined *onset* potentials are highlighted.

In both series of spectra (Figure 4a and b) as well as in all other (Figure S4 in the supporting information) two pronounced bands appear at 475 and 557  $\text{cm}^{-1}$  with increasing potential which can be assigned to Ni-O vibrations in  $\gamma$ -NiOOH<sup>49,33</sup> and which are known to have a high cross section.<sup>50</sup> Only for the 30% Fe sample, the band at higher wavenumbers is significantly shifted to lower value (550  $\text{cm}^{-1}$ ). For enhanced clarity the respective Raman spectra of all samples at 0.63 V are displayed in Figure 5a. With increased Fe content the band intensity at 475  $\text{cm}^{-1}$  decreases stronger in comparison to the 557  $\text{cm}^{-1}$  band. For quantification, the ratio of the absolute band intensities ( $I_{475}/I_{557}$ ) was calculated for all samples and plotted against the applied potential (Figure 5b). It is known that with increased Fe content the band ratio decreases which is a result of introduced disorder by iron atoms.<sup>34,51</sup> Accordingly, the highest ratio can be found in the Fe free sample. However, for the low Fe samples ( $\leq 7\%$  Fe) a potential dependency of the band ratio can even be found. After reaching a maximum (0.57 – 0.6 V), the ratio decreases with increasing potential which might be due to structural changes during electrochemical stress. Furthermore, the potential at which both bands indicate beginning  $\gamma$ -NiOOH formation is shifted to more positive values with increased Fe content (Figure 5b) which is in accordance with the electrochemical characterization (Figure 3a and S1b).

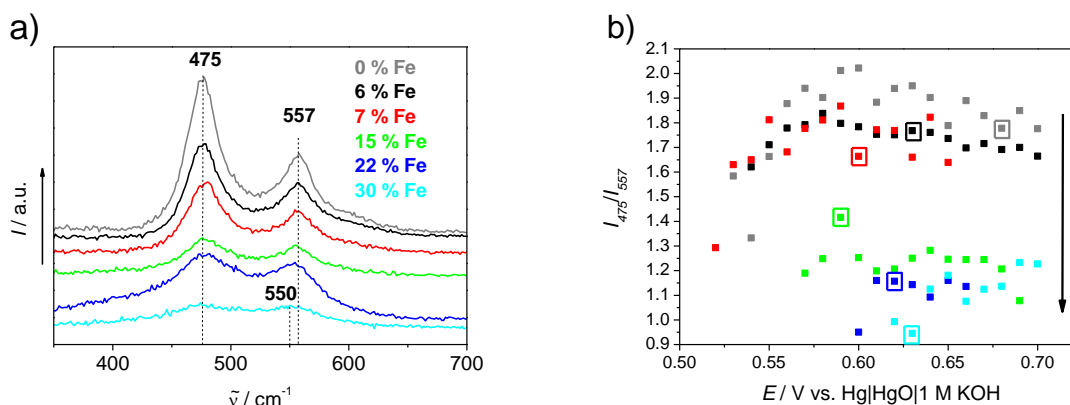


Figure 5: Raman spectra of all Ni and Ni/Fe samples at 0.63 V (a) and the band intensity ratio in dependence of the applied potential (b). The *onset* potential of oxygen evolution determined by SECM (Figure 3) is highlighted for each sample by a square frame in the respective color, and the arrow indicate the effect of increased Fe content on the  $I_{475}/I_{557}$  band ratio.

In order to discuss the SECM results obtained in the Raman-coupled experiment, the *onset* potential as an important kinetic parameter reflecting the apparent beginning of the OER is marked red in all spectra (Figure 4 and S4) as well as in the band ratio evaluation (square frames in Figure 5b). In all cases  $\gamma$ -NiOOH is present before oxygen evolution is observed. However, introducing small amounts of Fe introduces disorder into the  $\gamma$ -NiOOH phase as concluded from the decrease of  $I_{475}/I_{557}$  band ratio. Additionally, the *onset* potential shifts to considerably lower values. Introducing a certain amount of disorder (15% Fe in the present case) results in strongly enhanced OER activity, while a further increase of Fe content ( $> 15\%$ ) might be unfavorable. Thus, the general conclusion may be drawn that while  $\gamma$ -NiOOH seems to be necessary to obtain OER activity, its presence is not sufficient and additional changes in the structure occur which in this case is the disorder from introduced Fe atoms.

In order to verify in a dynamic voltammetric manner, the electrochemical results obtained potentiostatically with the *in situ* setup and to gain further insight into the electrocatalytic behavior of the Ni and Ni/Fe thin film electrodes, linear sweep voltammetry with low scan rates as a quite common electrochemical method to characterize electrocatalytically active materials towards a gas evolution reaction was performed (Figure 6a).

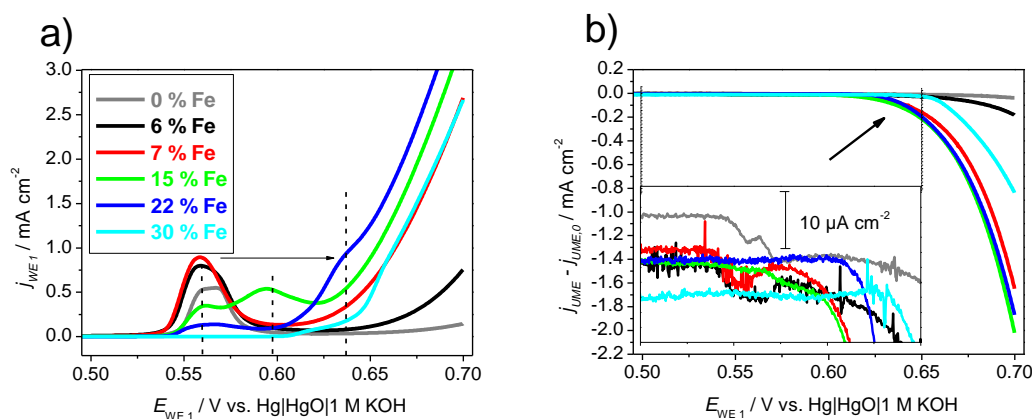


Figure 6: Linear sweep voltammograms (scan rate:  $1 \text{ mV s}^{-1}$ ) of the thin film electrodes; the arrow indicates the shift of the oxidation peak with increasing Fe content (a), and the simultaneously recorded currents at the UME in  $0.1 \text{ M KOH}$  (b); the arrow indicates the region of *onset* potentials for the OER as determined with this method, and the inset shows the enlarged  $0.5 - 0.65 \text{ V}$  region.

Again, the strong overlap of currents due to  $\text{Ni}^{\text{II}}$  oxidation with those due to oxygen evolution is apparent, influencing a Tafel analysis of the kinetic region. Thus, in addition, the UME currents were recorded where again the UME was held at constant potential ( $-0.6 \text{ V}$ ) to monitor oxygen evolution (Figure 6b). Clearly the LSV curves of the thin film electrodes strongly change with increasing Fe content. The well pronounced oxidation peak of  $\text{Ni}(\text{OH})_2$  to  $\text{NiOOH}$  at the bare nickel film vanishes with increasing iron content, and the peak position shifts from  $0.56 \text{ V}$  to  $\sim 0.63 \text{ V}$  in the 22% Fe sample and disappears with 30% Fe. The 15% Fe sample shows the formation of a double peak at  $0.56 \text{ V}$  and  $0.6 \text{ V}$ , which might be a result of the formation of different structures. This redox behavior is also visible in CV experiments (Figure S1b). The *onset* potentials for oxygen evolution might be determined in the same way as in the spectroelectrochemical experiment, and although there are slight differences to the steady-state experiments, the order of OER activity of the samples is the same. It can be concluded that the potentiostatic approach required for the spectroelectrochemical experiments is justified since it yields electrochemical results comparable to the classical LSV approach.

The inset of the  $0.5 - 0.65 \text{ V}$  region in Figure 6b showing the UME response provides further information about the processes taking place during the structural changes of the Ni and Ni/Fe thin film electrodes. Beside oxygen detection that dominates the current response of the UME other noticeably weaker effects can be observed before reaching the OER *onset*. At those potentials where the  $\text{Ni}^{\text{II}}$  oxidation in the LS voltammogram of the thin film electrodes (Figure 6a) appears, an increase of the cathodic current of  $\sim 5 \mu\text{A cm}^{-2}$  at the UME can be found, which was not observed during the potentiostatic experiments. This additional cathodic current can only be found in the pure Ni thin film and in the samples with a Fe content up to 15%. With



increased Fe content it either vanishes or merges inseparably with the OER potential region. The observation of additional currents is in contrast to Chen *et al.*, who found decreased UME currents right before reaching the *onset* potential at a  $\text{Ni}_x\text{O}_y$  electrode;<sup>39</sup> these differences might be attributed to the lower LSV scan rate used in our experiment. The most likely explanation of this unexpected feature is the release of “active” oxygen or peroxide species that evolve during the  $\gamma$ -NiOOH formation as suggested based on spectroscopic findings.<sup>52</sup> Recently amorphous  $\text{NiO}_x$  films were studied by rotating ring disk electrode (RRDE) measurements to determine the reaction pathway of the OER. A slow catalytic OER within the first anodic peak (NiOOH formation as confirmed by our *in situ* spectroscopic experiments) during dynamic voltammetric experiments was supposed which may be a result of the decomposition of peroxide ions.<sup>53</sup> As this phenomenon could only be observed in dynamic voltammetric experiments (CV, LSV) and not during steady-state (cf. Figure 3) this would be in accordance to the observations in the literature. As known from ORR catalysis research, SECM may help to identify intermediates, e.g., peroxide with higher collection efficiency than in RRDE experiments.<sup>54,55</sup> This collection efficiency might be the reason why the additional oxygen formation is visible in the LSV experiments with oxygen detection at the UME. In addition, the prepared thin film electrodes are non-porous which minimizes reabsorption of released molecules. Our results may substantiate the suggestions by Smith and Berlinguette<sup>53</sup> on another active center evolving oxygen, albeit slowly, at significantly lower overpotentials resulting in the observed current response of the UME during  $\gamma$ -NiOOH formation.

## 4.4 Conclusion

In this study, we demonstrated the realization of a setup combining Raman and SECM measurements as an advanced tool of spectroelectrochemical research bringing the benefits of the individual techniques together while leaving the classical SECM geometry undisturbed. To highlight the applicability of this setup, Ni and Ni/Fe thin films deposited onto transparent ITO electrodes were studied towards the OER. The potential-dependent electrochemical responses of the respective film and the ultramicroelectrode were recorded and the *onset* potential as an important kinetic parameter was determined by evaluating the microelectrode currents. The lowest OER *onset* potential ( $\sim 0.59$  V) was found for the Ni/Fe film containing 15% Fe. From the Raman spectra recorded simultaneously the development of a  $\gamma$ -NiOOH phase was observed where the band ratio of the prominent double band at 475 and 557  $\text{cm}^{-1}$  decreases with increasing Fe content which is attributed to introduced disorder. Furthermore, it is demonstrated that although the presence of the  $\gamma$ -NiOOH phase is necessary to obtain high activity for OER, its presence is not sufficient and other structural changes (i.e. introduced disorder by Fe atoms) must occur. Further LSVs with oxygen detection at the UME surprisingly showed additional very weak reductive currents before the OER *onset* potential is reached, especially at those thin films with low Fe content. The currents are observed in the same potential region where the transition of  $\text{Ni}(\text{OH})_2$  to  $\gamma$ -NiOOH is found electrochemically and spectroscopically and might be a result of a weak oxygen or peroxide evolution at low overpotentials at a different catalytically active site. In general, with the application of our novel *in situ* spectroelectrochemical setup we were able to provide novel insight into structure, structural changes and resulting activity of NiFe oxides/hydroxides, correlating a certain disorder induced by Fe with high activity as well as the formation of  $\gamma$ -NiOOH with the appearance of weak oxygen/peroxide evolution activity.

## 4.5 References

- (1) Carmo, M.; Fritz, D. L.; Mergel, J.; Stolten, D. *Int. J. Hydrogen Energy* **2013**, *38*, 4901–4934.
- (2) Chen, Z.; Higgins, D.; Yu, A.; Zhang, L.; Zhang, J. *Energy Environ. Sci.* **2011**, *4*, 3167.
- (3) Debe, M. K. *Nature* **2012**, *486*, 43–51.
- (4) Dionigi, F.; Strasser, P. *Adv. Energy Mater.* **2016**, 1600621.
- (5) Borup, R.; Meyers, J.; Pivovar, B.; Kim, Y. S.; Mukundan, R.; Garland, N.; Myers, D.; Wilson, M.; Garzon, F.; Wood, D.; Zelenay, P.; More, K.; Stroh, K.; Zawodzinski, T.; Boncella, J.; McGrath, J. E.; Inaba, M.; Miyatake, K.; Hori, M.; Ota, K.; Ogumi, Z.; Miyata, S.; Nishikata, A.; Siroma, Z.; Uchimoto, Y.; Yasuda, K.; Kimijima, K.-I.; Iwashita, N. *Chem. Rev.* **2007**, *107*, 3904–3951.
- (6) Wu, J.; Yuan, X. Z.; Martin, J. J.; Wang, H.; Zhang, J.; Shen, J.; Wu, S.; Merida, W. *J. Power Sources* **2008**, *184*, 104–119.
- (7) Smith, M. C.; Gilbert, J. A.; Mawdsley, J. R.; Seifert, S.; Myers, D. J. *J. Am. Chem. Soc.* **2008**, *130*, 8112–8113.
- (8) Petrova, O.; Kulp, C.; van den Berg, M. W. E.; Klementiev, K. V.; Otto, B.; Otto, H.; Lopez, M.; Bron, M.; Grunert, W. *Rev. Sci. Instrum.* **2011**, *82*, 44101.
- (9) Russell, A. E.; Rose, A. *Chem. Rev.* **2004**, *104*, 4613–4636.
- (10) Ali-Löyty, H.; Louie, M. W.; Singh, M. R.; Li, L.; Sanchez Casalongue, H. G.; Ogasawara, H.; Crumlin, E. J.; Liu, Z.; Bell, A. T.; Nilsson, A.; Friebel, D. *J. Phys. Chem. C* **2016**, *120*, 2247–2253.
- (11) Nesselberger, M.; Arenz, M. *ChemCatChem* **2016**, *8*, 1125–1131.
- (12) Tian, Z.-Q.; Ren, B. *Annu. Rev. Phys. Chem.* **2004**, *55*, 197–229.
- (13) Bard, A. J.; Mirkin, M. V., Eds. *Scanning electrochemical microscopy*, 2nd edn.; CRC Press: Boca Raton, Fla, 2012.
- (14) Bertonecello, P. *Energy Environ. Sci.* **2010**, *3*, 1620.
- (15) Schuhmann, W.; Bron, M., Scanning electrochemical microscopy (SECM) in proton exchange membrane fuel cell research and development. In *In Situ Characterisation Techniques for Low Temperature Fuel Cells*; Hartnig, C.; Roth, C., Eds.; Woodhead Pub: Cambridge, U.K., 2012.
- (16) Zoski, C. G. *J. Electrochem. Soc.* **2015**, *163*, H3088-H3100.
- (17) Wain, A. J. *Electrochem. Commun.* **2014**, *46*, 9–12.
- (18) Ackermann, S.; Steimecke, M.; Morig, C.; Spohn, U.; Bron, M. *J. Electroanal. Chem.* **2017**, *795*, 68–74.
- (19) Zeradjanin, A. R.; Menzel, N.; Schuhmann, W.; Strasser, P. *Phys. Chem. Chem. Phys.* **2014**, *16*, 13741–13747.
- (20) Knittel, P.; Higgins, M. J.; Kranz, C. *Nanoscale* **2014**, *6*, 2255.
- (21) Kranz, C.; Friedbacher, G.; Mizaikoff, B.; Lugstein, A.; Smoliner, J.; Bertagnolli, E. *Anal. Chem.* **2001**, *73*, 2491–2500.
- (22) Macpherson, J. V.; Unwin, P. R.; Hillier, A. C.; Bard, A. J. *J. Am. Chem. Soc.* **1996**, *118*, 6445–6452.
- (23) Treutler, T. H.; Wittstock, G. *Electrochim. Acta* **2003**, *48*, 2923–2932.
- (24) Wang, L.; Kowalik, J.; Mizaikoff, B.; Kranz, C. *Anal. Chem.* **2010**, *82*, 3139–3145.
- (25) Etienne, M.; Dossot, M.; Grausem, J.; Herzog, G. *Anal. Chem.* **2014**, *86*, 11203–11210.
- (26) Schlücker, S. *Angew. Chem. Int. Ed.* **2014**, *53*, 4756–4795.
- (27) Kourouski, D.; Mattei, M.; van Duyne, R. P. *Nano Lett.* **2015**, *15*, 7956–7962.
- (28) Lyons, M. E.; Brandon, M. P. *J. Electroanal. Chem.* **2010**, *641*, 119–130.
- (29) Li, X.; Walsh, F. C.; Pletcher, D. *Phys. Chem. Chem. Phys.* **2010**, *13*, 1162.

- (30) Trotochaud, L.; Ranney, J. K.; Williams, K. N.; Boettcher, S. W. *J. Am. Chem. Soc.* **2012**, *134*, 17253–17261.
- (31) Cappadonia, M.; Divisek, J.; Heyden, T. von der; Stimming, U. *Electrochim. Acta* **1994**, *39*, 1559–1564.
- (32) Kostecki, R.; McLarnon, F. *J. Electrochem. Soc.* **1997**, *144*, 485–493.
- (33) Yeo, B. S.; Bell, A. T. *J. Phys. Chem. C* **2012**, *116*, 8394–8400.
- (34) Louie, M. W.; Bell, A. T. *J. Am. Chem. Soc.* **2013**, *135*, 12329–12337.
- (35) Klaus, S.; Cai, Y.; Louie, M. W.; Trotochaud, L.; Bell, A. T. *J. Phys. Chem. C* **2015**, *119*, 7243–7254.
- (36) Trotochaud, L.; Young, S. L.; Ranney, J. K.; Boettcher, S. W. *J. Am. Chem. Soc.* **2014**, *136*, 6744–6753.
- (37) Friebel, D.; Louie, M. W.; Bajdich, M.; Sanwald, K. E.; Cai, Y.; Wise, A. M.; Cheng, M.-J.; Sokaras, D.; Weng, T.-C.; Alonso-Mori, R.; Davis, R. C.; Bargar, J. R.; Nørskov, J. K.; Nilsson, A.; Bell, A. T. *J. Am. Chem. Soc.* **2015**, *137*, 1305–1313.
- (38) Chen, J. Y. C.; Dang, L.; Liang, H.; Bi, W.; Gerken, J. B.; Jin, S.; Alp, E. E.; Stahl, S. S. *J. Am. Chem. Soc.* **2015**, *137*, 15090–15093.
- (39) Chen, X.; Botz, A. J. R.; Masa, J.; Schuhmann, W. *J. Solid State Electrochem.* **2016**, *20*, 1019–1027.
- (40) Snook, G. A.; Duffy, N. W.; Pandolfo, A. G. *J. Electrochem. Soc.* **2008**, *155*, A262.
- (41) Botz, A. J.; Nebel, M.; Rincón, R. A.; Ventosa, E.; Schuhmann, W. *Electrochim. Acta* **2015**, *179*, 38–44.
- (42) Maljusch, A.; Ventosa, E.; Rincón, R. A.; Bandarenka, A. S.; Schuhmann, W. *Electrochem. Commun.* **2014**, *38*, 142–145.
- (43) Seiffarth, G.; Steimecke, M.; Walther, T.; Kühhirt, M.; Rümmler, S.; Bron, M. *Electroanalysis* **2016**, *28*, 2335–2345.
- (44) Steimecke, M.; Rümmler, S.; Kühhirt, M.; Bron, M. *ChemElectroChem* **2016**, *3*, 318–322.
- (45) Bode, H.; Dehmelt, K.; Witte, J. *Electrochim. Acta* **1966**, *11*, 1079–1087.
- (46) Lyons, M. E.; Cakara, A.; O'Brien, P.; Godwin, I.; Doyle, R. L. *Int. J. Electrochem. Sci.* **2012**, *7*, 11768–11795.
- (47) Corrigan, D. A. *J. Electrochem. Soc.* **1989**, *136*, 723.
- (48) Corrigan, D. A. *J. Electrochem. Soc.* **1989**, *136*, 613.
- (49) Cornilsen, B. C.; Shan, X.; Loyselle, P. L. *J. Power Sources* **1990**, *29*, 453–466.
- (50) Desilvestro, J. *J. Electrochem. Soc.* **1988**, *135*, 885.
- (51) Lu, Z.; Xu, W.; Zhu, W.; Yang, Q.; Lei, X.; Liu, J.; Li, Y.; Sun, X.; Duan, X. *Chem. Commun.* **2014**, *50*, 6479–6482.
- (52) Trzesniewski, B. J.; Diaz-Morales, O.; Vermaas, D. A.; Longo, A.; Bras, W.; Koper, M. T. M.; Smith, W. A. *J. Am. Chem. Soc.* **2015**, *137*, 15112–15121.
- (53) Smith, R. D. L.; Berlinguette, C. P. *J. Am. Chem. Soc.* **2016**, *138*, 1561–1567.
- (54) Dobrzeniecka, A.; Zeradjanin, A.; Masa, J.; Puschhof, A.; Stroka, J.; Kulesza, P. J.; Schuhmann, W. *Catal. Today* **2013**, *202*, 55–62.
- (55) Okunola, A. O.; Nagaiah, T. C.; Chen, X.; Eckhard, K.; Schuhmann, W.; Bron, M. *Electrochim. Acta* **2009**, *54*, 4971–4978.

## 4.6 Supporting information

To demonstrate the essential features of the Raman-coupled scanning electrochemical microscope, Ni and Ni/Fe thin film electrodes were prepared by chrono-potentiometric electrodeposition. A cathodic current of  $50 \mu\text{A cm}^{-2}$  was applied over a period of 1000 s. The corresponding E/t-curves are displayed in Figure S1a. The atomic ratio of the respective metal sulfates (10 mM deposition solution) were adjusted as shown in Table S1.

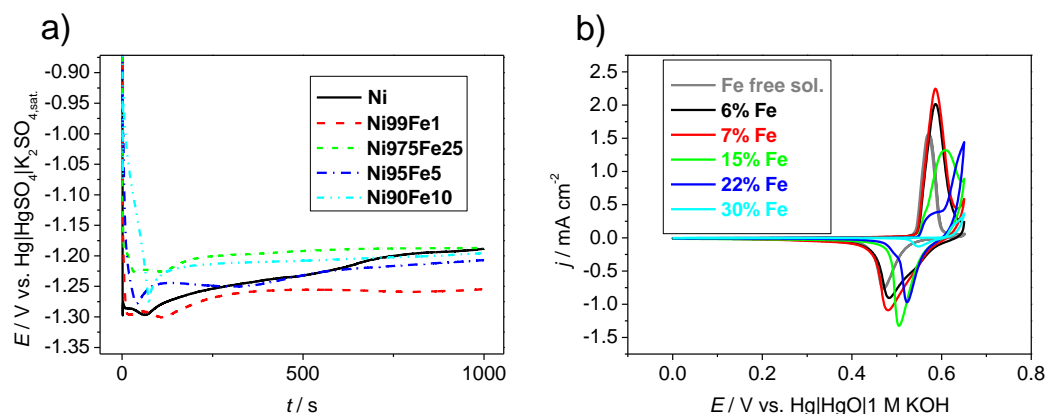


Figure S1: Chrono-potentiometric curves of the deposition in the respective metal salt solution (a) and cyclic voltammograms of all prepared thin film electrodes in 0.1 M KOH, scan rate  $5 \text{ mV s}^{-1}$  (b).

The composition of the thin film electrodes determined via ICP-OES (Table S1) showed high amounts of Fe in all samples which (in accordance to other work, see main text) is in all cases higher than the relative proportion in the deposition solution. Additional Fe introduced into the films is likely caused by the presence of Fe in the 0.1 M KOH solution.

Table S1: Composition of the deposition solutions and the ICP-OES results of the composition of the Ni and Ni/Fe thin film electrodes determined after dissolving them in 5 ml concentrated  $\text{HNO}_3$ .

atomic ratio of the deposition solution	[Fe] / $\text{mg L}^{-1}$	[Ni] / $\text{mg L}^{-1}$	wt% Fe
Ni*	< LOD	0.284	0
Ni**	0.032	0.496	6.1
Ni99Fe1	0.036	0.503	6.7
Ni975Fe25	0.063	0.345	15.4
Ni95Fe5	0.121	0.433	21.8
Ni90Fe10	0.133	0.316	29.6

\*used in Fe free solution, \*\*Additionally, in this solution  $1.89 \text{ mg L}^{-1}$  indium and  $0.223 \text{ mg L}^{-1}$  tin were found resulting in 10.6 wt% Sn in Sn/In (m/m).

To exclude an influence of the substrate on the Fe content, X-ray photoelectron spectroscopy (not displayed) of the bare indium-doped tin oxide (ITO) electrode was performed without

finding any traces of Fe. The surface composition was found to be 10.3 wt% Sn in Sn/In (evaluating the areas of In 3p<sup>3/2</sup> and Sn 3p<sup>1/2</sup> peaks). This value correlates to the bulk composition of Sn/In that was additionally determined using ICP-OES (Table S1).

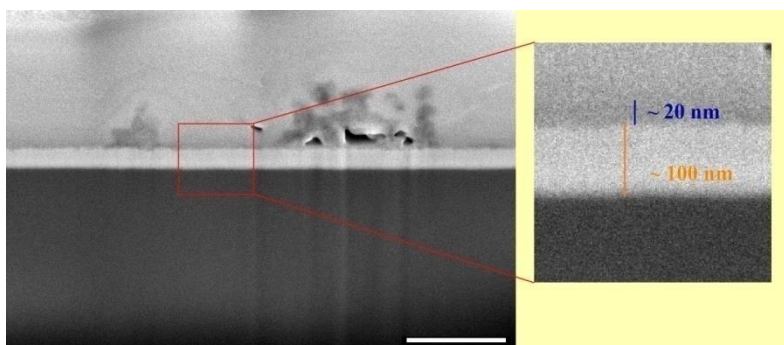


Figure S2: Electron microscopy image of the sample containing 30 % Fe sample after the electrochemical characterization procedure, the thin film is visible with dark shadow-like appearance above the bright ITO layer, the white scale bar represents 500 nm.

To get an impression of the morphology of the prepared thin films individual samples were studied with scanning electron microscopy. As displayed in Figure S2, on top of the non-conductive quartz substrate (dark) a bright layer of ~100 nm thickness can be found. This layer is likely composed of ITO and the thickness is in accordance to the manufacturer information. An additional darker region on top of the ITO with a thickness of 20 – 50 nm on the average is attributed to the deposited thin film layer containing also larger agglomerates.

Raman spectra were corrected by subtracting the initial spectrum at OCP potential. As shown in Figure S3a broad Raman features at ~500, 600 and 800 cm<sup>-1</sup> can be observed that are attributed to the conductive indium-doped tin oxide layer.

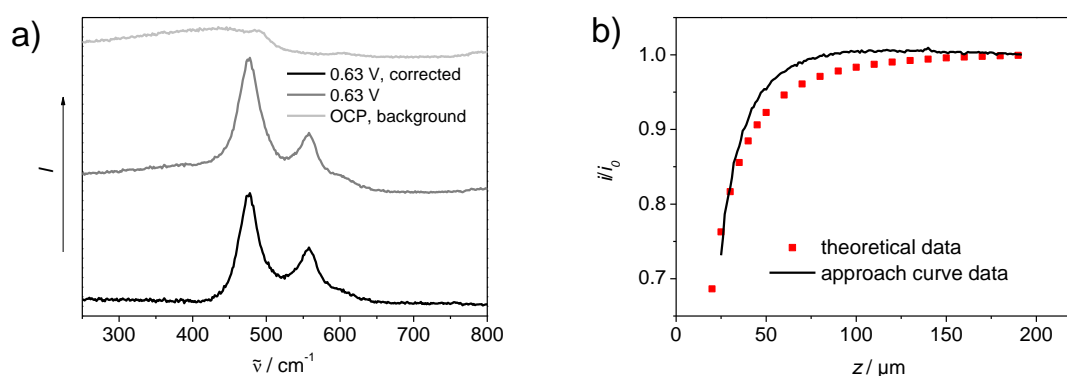


Figure S3: *In situ* Raman spectra of the Fe free Ni sample in 0.1 M KOH at OCP and at 0.63 V and the resulting corrected spectrum (a) and an example of an approach curve to the ITO substrate as well as theoretical approach data of a 25 μm microelectrode (b).

As mentioned in the experimental part, the UME was positioned by an approach curve measurement bringing the UME to the ITO substrate while a constant reductive potential (-0.6 V) was applied. This experiment could even be controlled by the inverted microscope. An example of such an approach curve which is representative for all other curves can be found in Figure S3b showing the normalized current ( $i/i_0$ ) plotted against the relative tip-to-sample distance. Comparing the obtained curve with theoretical data of a negative feedback a sufficient accordance can be found.

The *in situ* Raman spectra of the 6% and 22% Fe containing samples are displayed in the main text (Figure 4). All the other spectra which were obtained during the coupled experiments are shown in Figure S4. As stated in the main text, the 30% Fe sample shows a shift of the  $557\text{ cm}^{-1}$  band to lower wavenumbers ( $550\text{ cm}^{-1}$ ). Additionally in this sample, a third weak band can be found as a shoulder of the  $475\text{ cm}^{-1}$  band at  $\sim 500\text{ cm}^{-1}$ .

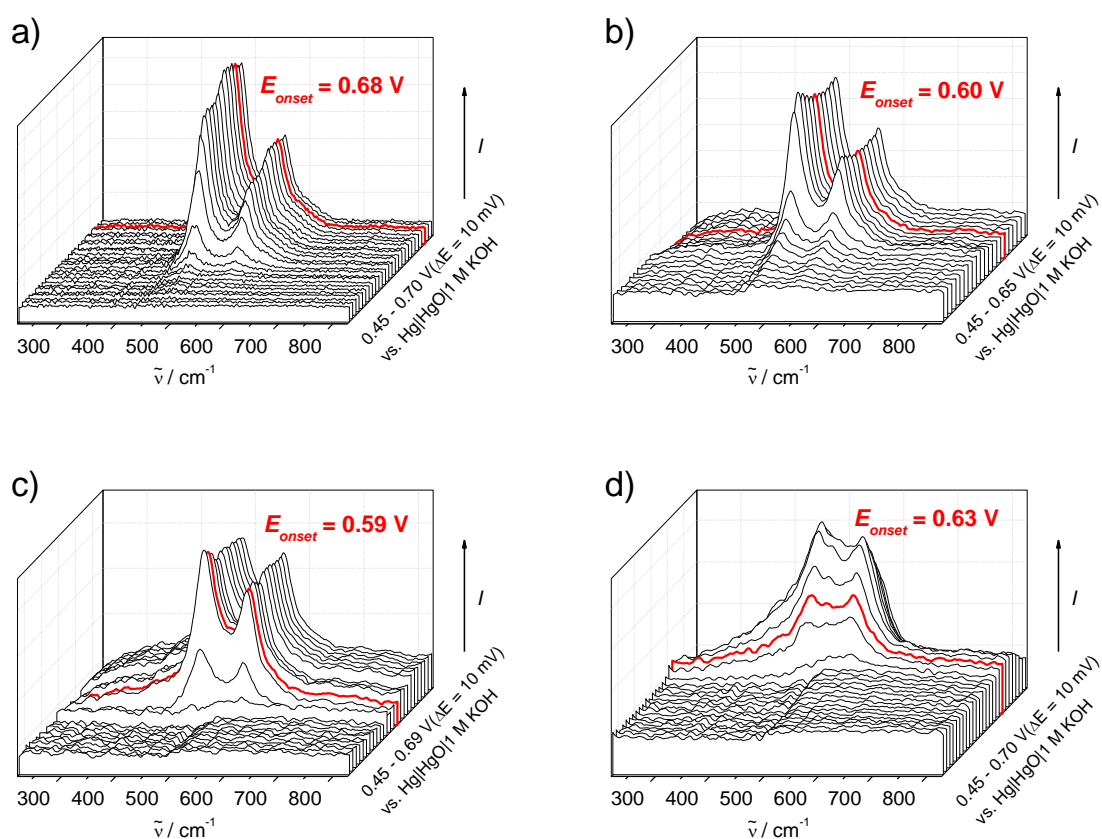


Figure S4: *In situ* Raman spectra of Ni thin film electrodes in Fe-free solution (a) and with 7 % (b), 15 % (c) and 30 % Fe content (d) in dependence of the applied potential, the *onset* potential detected by the UME is highlighted for every sample; all spectra are background corrected by subtracting the initial spectrum at OCP.

To exclude any effects from the transparent conductive substrate, the bare ITO electrode was even examined by the very same procedure as the Ni and Ni/Fe thin film electrodes. The results

can be found in Figure S5a where the current densities of the electrode and the UME response are plotted against the applied potential. Here, the UME response shows a starting oxygen evolution at potentials  $> 0.69$  V, but the current density increase of the electrode as well as the UME response are magnitudes lower than in Figure 3. It can be concluded that the activity for the OER of the bare ITO is significantly lower than those of the Ni and Ni/Fe films. Also the Raman spectra are not affected by the ITO substrate which can be concluded from Figure S5b. The substrate shows Raman bands as already mentioned at  $\sim 300$ ,  $600$  and  $800$   $\text{cm}^{-1}$  which do not change during potential modulation. By subtracting the initial spectrum at  $0.1$  V as in Figure S3a these peaks can be removed. As a result, other raising bands are only attributed to the structural changes in the Ni and Ni/Fe thin film electrodes.

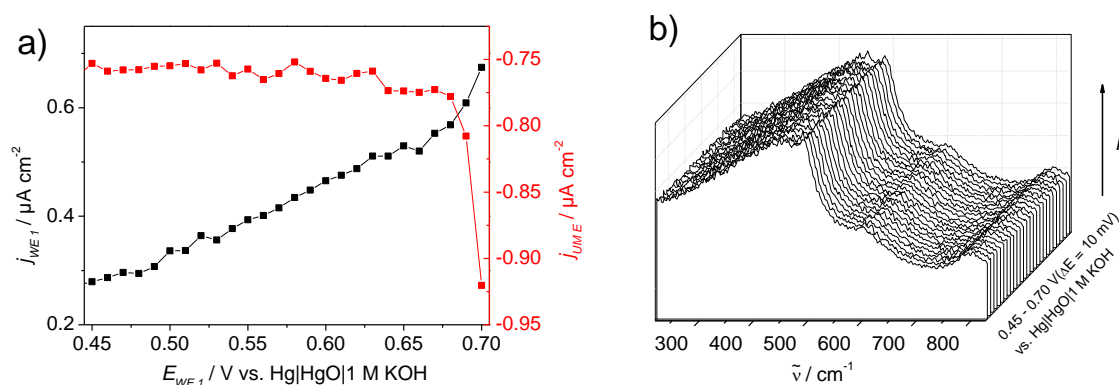


Figure S5: Current densities measured at the bare ITO electrode as well as the UME response (red) at  $-0.6$  V for oxygen detection (a) and corresponding *in situ* Raman spectra in  $0.1$  M KOH (b), please notice that the current densities are magnified by a factor of 1000 in comparison to the results in Figure 3 showing Ni and Ni/Fe thin film electrodes, lines connecting the data points are intended as a help for the eye.

Thus, indium-doped tin oxide on quartz glass can be used as adequate transparent and conductive material, which can be applied as electrode in such *in situ* experiments.



## 5 Raman microscopy and SECM as complementary techniques

*The content of this part has been published as*

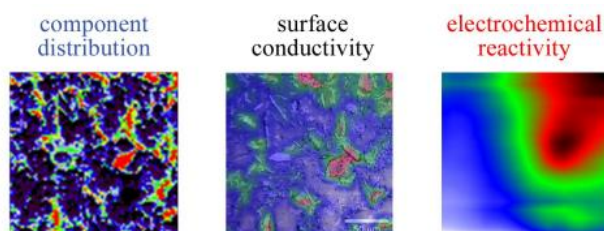
### **A complementary Raman and SECM study on electrically conductive coatings based on graphite sol-gel composite electrodes for the electrochemical antifouling**

*Reprinted from S. Ackermann, M. Steimecke, C. Morig, U., M. Bron, Journal of the Electroanalytical Chemistry 2017, 795, 68-74 with permission from Elsevier, Copyright © 2017.*

**DOI: 10.1016/j.jelechem.2017.04.029**

#### Abstract

The surface of electrically conductive coatings based on a sol-gel lacquer with graphite as conductive additive that were developed for the use in marine antifouling technology was examined with two powerful surface characterization techniques, namely Raman microscopy and scanning electrochemical microscopy (SECM). These two methods provide information about the distribution of compounds as well as conductivity. A correlation of these two techniques reveals that not all conductive material contributes equally to the overall conductivity. Furthermore, the coating was examined with respect to its spatially resolved electrocatalytic activity towards the evolution of chlorine and oxygen which are the main active molecules generated during electrochemical stress. The comparison of the very same area showed electrocatalytically active hot spots with higher rate of generation of these species compared to the value averaged over the electrode area, and the results could be correlated to conductivity and graphite particle distribution.



## 5.1 Introduction

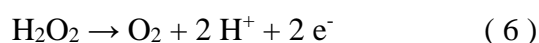
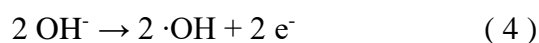
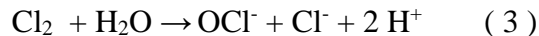
In the presence of water, biofouling, which is the undesired growth and adhesion of micro- and other small organisms, is ubiquitously occurring on all surfaces. The process of biofouling is known as the adsorption of biopolymers followed by the adhesion and growth of micro- or multicellular organisms on a surface. Caused by nutrient deficiency and inflow, microorganisms such as bacteria or algae form a strongly pronounced extracellular matrix that can adsorb irreversibly at a surface [1–3]. Biofouling is a cost-intensive problem providing the basis of a billion dollar industry producing chemicals for biocides, cleaners and antifouling materials [4].

In seawater, simultaneously to this process, multicellular marine organisms such as macro algae, fungi, barnacles and mussels start growing inhomogeneously into the water phase [3,5,6]. Thereby the surface roughness and in consequence the flow properties of the respective compartment change unfavorably. For example, on underwater ship hulls this phenomenon can increase the hydrodynamic drag causing an increase of more than 80 % of fuel consumption at a pre-adjusted velocity of the ship. The blocking of cooling water pipes and ballast tanks are other unwanted consequences. Up to now, no universally acting antifouling coating is known and should not be expected, since the conditions and the biotopes dependent on the marine nutrients, their different composition and concentration, temperature and salt concentration. Therefore, there is great demand for a long-term stable and universally operating surface modification to prevent biofouling. The state of the art is determined by continuously improved antifouling paints grouped in two categories: biocide containing coatings consisting of copper containing [6] and copper-free polymeric lacquers, and fouling release coatings, which are slippery or have impenetrable glassy surfaces such that fouling organisms have an extremely weak grip on it [7]. Electrically conductive coatings for the electrochemical removal of biofilms are a promising alternative in this field but require cheap and easily processible conductive coating materials. Conductive coatings based on carbon as conductive additive [8], modified carbon [9] as well as metals, e.g. titanium [10], steel [11] or semiconductors [12] have already been studied for the electrochemical removal of biofilms in various applications and can be possibly applied as electrode material at the hull or other relevant parts such as heat exchanger and pipes of a ship and prevent them from marine biofouling. Cathodic [13,14] or anodic currents [8,10] as well as alternating currents [15] can be applied to the conductive coatings working as electrodes in a way that the applied voltages are higher than the decomposition voltage of water which finally creates a pH stress in a thin water layer around [16].

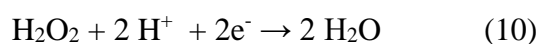
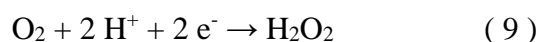
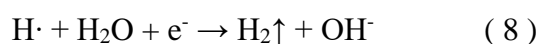
Thus, actively controllable antifouling surfaces could be an alternative approach in the near future. Sandrock and Scharf proposed the application of electrochemically generated pH stress by alternating adjustment of alkaline and acid pH values at the surface of electrically conductive surfaces [17,18]. Spohn *et al.* [19,20] developed large area and paintable electrodes consisting of a highly conductive paint layer over coated by an outer, electrochemically stable layer with much lower conductivity to achieve a homogenous distribution of electrolysis current density. These electrodes are based on inexpensive and easily processable conducting paints and were deposited onto steel plates by roller coating. Seawater was electrolyzed by those alternatingly polarized large area electrodes to achieve a controlled electrochemical antifouling at the electrode surfaces. Up to now, the marine application of such electrochemical antifouling systems is limited by the electrochemical stability of the outer coating layer [20].

However, this principle is inherently combined with the electrochemical oxidation and reduction of seawater according to the following reactions:

At the anode:



and at the cathode:



Thus, the electrochemically generated pH stress is inherently combined with a redoxchemical stress [16,21]. The generation of the highly reactive species, the oxidative  $\cdot\text{Cl}$  and  $\cdot\text{OH}$ , and the reductive  $\text{H}\cdot$  is assumed to be limiting for the electrochemical stability of the electrodes consisting of graphite particles embedded in a polymer matrix. If the  $\cdot\text{OH}$  radicals do not recombine fast enough, they will attack the graphite, likely starting at edges with hydroxylation followed by formation of carboxylate groups, ring opening and release of carbon dioxide. Similarly, the highly reactive chlorine atoms will attack the electrode surface, preferably the

polymer matrix. The H $\cdot$  radical is a highly reactive reductant, which can donate electrons to aromatic systems inducing the addition of protons and resulting in a hydrogenation. At least in highly acidic electrolytes hydrogen atoms can be intercalate and hydrogenate graphite destabilizing it [22].

In this contribution it is shown how the application of complimentary surface characterization techniques can improve our understanding of structural features and electrochemical processes at the surface of polymer graphite composites and how they are connected. Raman microscopy as a non-contacting, non-destructive and non-invasive technique can provide spatially resolved information about components, their chemical structure and distribution on a surface (Raman mapping). In surface and corrosion science the method is, for example, used for product determination and distribution in corrosion experiments of metals [23] or protection agents [24], as well as locally introduced stress in materials [25]. The evaluation of all obtained Raman spectra at the respective position leads to a distribution (often displayed in form of a topography map) of single or multiple components. Hence, in the presented study this technique allows to differentiate between conductive and isolating zones formed by graphite and the polymeric lacquer matrix, respectively, on a micrometer scale based on the D and G Raman bands of graphite.

Scanning electrochemical microscopy (SECM) [26,27] is a laterally highly resolving method to determine the distribution of (electro)chemical processes occurring on a substrate, typically an electrode. Beside many other research fields, this technique is applicable to investigations of corrosion processes [28–30]. In all cases of SECM imaging, an ultramicroelectrode (UME) is moved stepwise in a short distance over the sample surface. After each step, an electrochemical experiment is carried out at the UME to provide information about the underlying substrate or (electro)chemical properties at the respective location. Thus, SECM can be named a true “chemical microscopy”. In this work two different modes of SECM are used for surface characterization. As the most straightforward mode the feedback mode, where an oxidation or reduction reaction at the UME is enhanced or diminished, provides information about the electrical conductivity or inertness of the sample surface at the location of the UME. As a result a map showing insulating and conductive regions can be created. The second mode used here is the sample generation-tip collection (SG/TC) mode, during which electroactive molecules, e.g. oxygen and/or chlorine are formed at the sample surface which can be detected by the UME in close distance above the sample. This mode results in maps of the intensity and

distribution of electrode reactions. The SG/TC has already been used for the visualization of the chlorine evolution reaction (CER) [31,32] as well as the oxygen evolution reaction (OER) [33,34]. Both Raman microscopy and SECM provide complimentary information about the surface structure and the electrochemical behavior of the surface as already demonstrated before [35,36]. An instrument combining Raman microscopy and shearforce regulated SECM was reported as well [37].

The correlated information may also help to understand electrode processes in more detail and furthermore might help to improve the fabrication and properties of electrochemical antifouling coatings. More generally, it is shown how the combination of the used powerful surface characterization tools may help to gain insight into the structure and localized electrochemical properties of heterogeneous surfaces.

## 5.2 Experimental

### 5.2.1 Preparation of the conductive coating samples

Electrically conductive polymer graphite composites were deposited on planar and rectangular copper samples resulting in a precisely defined electrode area of 30 x 50 mm<sup>2</sup>. First the hybrid sol-gel components A: NTC 2K Et-Sil 110 Marine and B: NTC curing agent Et-Sil (both Nano Tech Coatings GmbH, Tholey) were mixed for 5 min in a double centrifuge (Speedmixer DAC 150 SP, Hauschild, Hamm) in a mass ratio of 3:1. Between 0 and 35 wt.% graphite flakes (cat. no. 282863, particle size < 20 µm, Sigma-Aldrich) were added as second constituent to the premixed lacquer followed by mixing for additional five minutes. The coating layers were applied to the substrate via a foam roll resulting in an average coating thickness between 100 to 300 µm determined by scanning electron microscopy (not displayed). After 48 hours of drying at air the samples were sandblasted and polished with a polishing machine (Saphir 320 instrument with SiC wet grinding paper 200/2400, both ATM GmbH, Mammelzen) to obtain a smooth surface. The roughness of the prepared electrode surface was determined by a profilometer (Dektak XT, Bruker) to  $R_a = 0.17 \mu\text{m}$  and a maximum height deviation of  $R_z = 1.01 \mu\text{m}$ . The samples were named after the lacquer supplier followed by the content of graphite, i.e. NTC-G20 is a coating sample containing 20 wt.% graphite. The rectangular sample area for probing was defined by fixing stripes of an adhesive tape (Tesa<sup>®</sup>, 50 µm thickness) enabling the relocation of the investigated area by Raman microscopy as well as by SECM. This finally allows for a comparison of the corresponding images.

### 5.2.2 Determination of conductivity

To directly determine the specific conductivity of polymer lacquer coatings the four point method of Valdes [38] was used in combination with a measurement of the coating layer thickness. To exclude the effect of the copper substrate the samples were prepared analogously as described above but on a plastic carrier. A measuring probe with four identical and spring-loaded gold contacts with ball shaped tips were connected to a source of a precisely defined current of 100 mA, the Source Measurement Unit SMU 236 and a 2010 multimeter (both from Keithley, Tektronix GmbH, Germering, Germany). The voltage drop was measured between the inner contact tips. The specific resistivity was calculated from the recorded voltage current line, the layer thickness and the equidistance of 10 mm between the contact points taking into consideration the geometric parameters according to Miccoli *et al.* [39], Valdes [38] and Lu *et al.* [40].

### 5.2.3 Scanning electrochemical microscopy

An SECM instrument (Sensolytics GmbH, Bochum, Germany) consisting of stepper motors for positioning in x, y and z direction with an Autolab bipotentiostat (PGSTAT128N, Metrohm) was used to perform SECM experiments. A four electrodes setup was employed with a 10  $\mu\text{m}$  platinum ultramicroelectrode (Sensolytics GmbH) as working electrode (UME), the sample as second working electrode (WE), a platinum mesh as counter electrode (CE) and a  $\text{Ag}|\text{AgCl}|\text{KCl}_{\text{sat}}$  (SE 21, Forschungsinstitut Meinsberg, Germany) as reference electrode (RE). An electrochemical cell (Sensolytics GmbH) was mounted on a selected sample (see below) where an O ring as gasket prevents leaking of the redox mediator solution containing 2 mM  $\text{K}_3[\text{Fe}(\text{CN})_6]$  in 100 mM KCl (both salts from Carl Roth, Karlsruhe, Germany) at pH = 7. All experiments were performed potentiostatically. For the feedback experiments a potential of  $E_{\text{UME}} = -0.15 \text{ V}$  vs.  $\text{Ag}|\text{AgCl}|\text{KCl}_{\text{sat}}$  was applied to the UME resulting in a constant feedback current while the sample (WE) was at open circuit potential (OCP). For height positioning, the ultramicroelectrode was approached to the sample until the current changed by 25 % from the current in bulk solution, irrespective of whether a positive or a negative feedback was observed. Approach curves were recorded at various positions of the sample. Prior to each experiment, the ultramicroelectrode was polished with 0.3  $\mu\text{m}$  polishing paper (Sensolytics) followed by rinsing several times with water and ethanol. To investigate the quality of the ultramicroelectrode several cyclic voltammograms in the potential range of 0.5 to -0.2 V vs.  $\text{Ag}|\text{AgCl}|\text{KCl}_{\text{sat}}$  with scan rates of 50 and 100  $\text{mV s}^{-1}$  were recorded in the bulk mediator solution until a stable response was observed. Typical SECM images were collected by moving the UME in a comb-like mode along the sample. Further parameters of the SECM images are given in the result section. For data visualization the open source software Gwyddion 2.31 was used.

For the determination of electrochemical activity of the sample surface towards oxygen and chlorine evolution a slightly basic 1 M KCl solution (pH = 8 via KOH addition) was used to roughly mimic sea water conditions. The SG/TC mode was chosen, in which evolved oxygen and/or chlorine at the substrate electrode were detected at the UME. To establish these SECM experiments, UME voltammograms were recorded to identify a suitable potential, at which chlorine can selectively be detected in the presence of oxygen, and the potential range, in which the sum of both can be determined. To do so, an electrolysis was carried out by applying 1.6 V vs.  $\text{Ag}|\text{AgCl}|\text{KCl}_{\text{sat}}$  for 10 min to the substrate. A strong chlorine smell could be noticed after a while indicating a successful electrolysis process. In subsequent CV experiments at the UME in the bulk the relevant potential for chlorine reduction was identified and separated from those

for oxygen reduction, resulting in the following conditions for SECM measurements: At the substrate (WE) potentials ( $E_S$ ) of 1.2 V and 1.3 V vs. Ag|AgCl|KCl<sub>sat.</sub> are applied to generate a potential-dependent oxygen and/or chlorine evolution. Both potentials were derived from substrate CVs between 0.0 and 1.5 V with 50 mV s<sup>-1</sup> in the 1 M KCl solution. At the UME ( $E_{UME}$ ) 0.4 V and -0.3 V vs. Ag|AgCl|KCl<sub>sat.</sub> were applied for the reduction of the evolved chlorine and oxygen molecules. It should be noted that for the subsequent SECM measurements a fresh substrate was used, since the strong electrolysis might have altered its properties.

Measurements in SG/TC mode were directly carried out after the feedback experiment in K<sub>3</sub>[Fe(CN)<sub>6</sub>]/KCl mediator solution without a second approximation of the UME to the substrate. Instead, the mediator solution was carefully exchanged three times by deionized water and then by 1 M KCl (pH = 8) solution keeping the UME position or height unchanged. During the experiments the solution was continuously saturated with N<sub>2</sub>.

#### **5.2.4 Raman spectroscopy**

A Raman microscope consisting of an InVia Raman spectrometer (Renishaw) with 1800 l mm<sup>-1</sup> grating, a 532 nm laser (Cobolt CW DPSS, 100 mW, Renishaw) and a light microscope (DMI2000, Leica, Wetzlar) with a x20 objective was used to perform Raman mappings. Mapping recordings were realized by means of the Streamline<sup>TM</sup> imagine mode (Renishaw) with a tunable stage (Prior) and a stage controller (Renishaw) allowing a position resolution of 100 nm. During these measurements more than 40 positions on the sample were measured in parallel. With an illumination time of 30 s for each position around 6000 spectra were recorded within 75 min resulting in a lateral resolution of 2.7 μm per single spectrum. Data evaluation of the mapping was performed with the WiRE 3.3 software (Renishaw).



## 5.3 Results and discussion

### 5.3.1 Specific conductivity and local conductivity

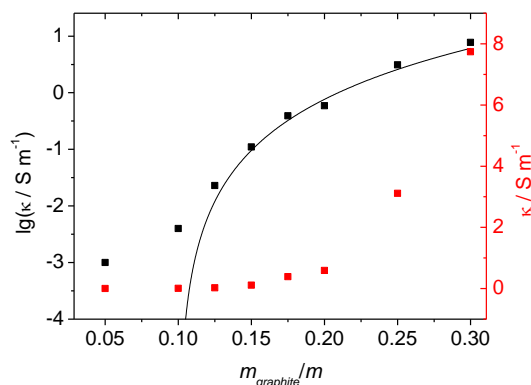


Figure 1: Logarithmic plot of the specific conductivity of the cured sol-gel layer in dependence of the graphite content  $m_{\text{graphite}}$  added to the mixture of the laqueur components including a fit to determine the percolation threshold (black line) as well as the obtained specific conductivity of all samples (red).

Figure 1 shows the logarithmic plot of specific conductivity of the coatings as a function of the graphite content. Starting at a graphite content of 15 wt.% graphite the conductivity is exponentially increasing to values  $> 0.1 \text{ S m}^{-1}$ , which we assume as a critical value for using 0.1 mm thick layers of graphite-sol-gel composites as electrodes for water electrolysis on a substrate with high conductivity, e.g. copper. A percolation threshold of 10 wt.% graphite can be derived (black line). The graphite content in the sol-gel coating may be increased to 30 wt.% achieving specific conductivities  $> 7 \text{ S m}^{-1}$  but this is accompanied with a too high roughness which leads to improved settlement of microorganisms at the surface [20]. Therefore, and because of a near optimum value of specific conductivity between 0.5 und  $1 \text{ S m}^{-1}$  the NTC-G20 lacquer with 20 wt.% graphite ( $0.6 \text{ S m}^{-1}$ ) was chosen for further investigations as a compromise between conductivity, mechanical stability and roughness.

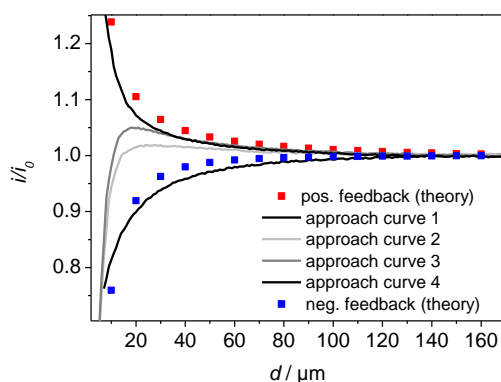


Figure 2: Approach curves performed at four different positions on the NTC-G20 sample. All currents are normalized to their values in bulk solution ( $E_{\text{UME}} = -0.15 \text{ V vs. Ag|AgCl|KCl}_{\text{sat.}}$ , in 2 mM  $[\text{Fe}(\text{CN})_6]^{3-}$ , 100 mM KCl) as well as theoretical approach curves of a  $10 \mu\text{m}$  UME to a conductive (red) and an insulating surface (blue).

In contrast to the specific conductivity measurements which probe the whole sample, SECM in feedback mode was used to gain insight into basic properties of the coating and in particular about the locally resolved electrochemistry and surface reactivity. Prior to this, it was necessary to analyze the UME response when approaching to the substrate surface of the NTC-G20 sample. In Figure 2 approach curves to different positions of the substrate are displayed together with the feedback responses of a microelectrode of 10  $\mu\text{m}$  in diameter as expected from theory [41–43]. At individual positions of the substrate, positive (curve 1) as well as negative feedback approach curves (curve 4) are obtained which closely fit to the theoretical ones. Such results are to be expected from a substrate which consists of conductive (graphite) and insulating (sol-gel lacquer) components and the curves can be associated with the respective pure components determining the UME feedback. At a conductive part of the surface,  $[\text{Fe}(\text{CN})_6]^{4-}$  produced at the microelectrode is oxidized back to  $[\text{Fe}(\text{CN})_6]^{3-}$ . Since electron transfer (ET) is considerably faster than diffusion into the bulk, the concentration of  $[\text{Fe}(\text{CN})_6]^{3-}$  is restored rapidly in the gap between substrate and UME upon approaching the surface which results in a positive current feedback. Approaching of the UME to insulating surface segments, a negative feedback is observed since hindered diffusion leads to a depletion of  $[\text{Fe}(\text{CN})_6]^{3-}$  in the vicinity of the UME. However, the portion of curves showing a positive feedback was relatively small reflecting the low amount of graphite (20 wt.%) in the sample. Some of the obtained approach curves showed a behavior comparable to curves 2 and 3 in Figure 2. While approaching from the bulk, the curve represents the behavior above a conductive substrate and a slight current increase is found. At a certain distance, the current turns into a negative feedback response. This behavior is common for conductive additives in an insulating matrix where heterogeneous kinetics is limited [43]. Here, the slow electron transfer (ET) rate of  $[\text{Fe}(\text{CN})_6]^{2-}$  at the graphite substrate together with the hindered diffusion into the gap leads to a turnaround in the current response when the UME is approaching the substrate. In addition, the used conductive additive may expose different surfaces structures (edge-plane and basal-plane sides of graphite). Considering the random distribution of micrometer graphite particles in the sol-gel matrix, it can be expected that graphite edge-plane sites are exposed to the surface which provide high electrochemical activity [44–46], also for the  $[\text{Fe}(\text{CN})_6]^{3-}/[\text{Fe}(\text{CN})_6]^{2-}$  redox couple [47]. The individual composition of the lacquer at the position where the UME is approached decides which is the apparent heterogeneous rate constant ( $k_{\text{eff}}$ ) and as a consequence which feedback responses is obtained [43].

Summarizing the above, SECM images of the NTC-G20 substrate should provide both negative and positive feedback. Given the low graphite content in the lacquer, negative feedback regions should dominate and would represent surfaces exposing insulating sol-gel lacquer containing no or very low amounts of graphite. Positive feedback regions will be observed at positions where mainly graphite particles are exposed to the surface realizing high conductivity at the respective positions.

However, the resulting SECM images are certainly strongly influenced by the resolution achieved with the experiment, which in turn is influenced by several factors. The most important one is the metal electrode diameter of the UME which limits the maximum achievable resolution [26]. Closely related to this, the tip to sample distance is strongly influencing the resolution as well as the distance and size of active spots or particles.

### **5.3.2 Comparison of the electrochemical topography and Raman microscopy**

SECM imaging was used to visualize the local reactivity distribution that is caused by the conductive graphite in the lacquer. The distribution of graphite in the NTC-G20 sample can also be observed by light microscopy (Figure 3a) showing graphite particles with higher light reflection, however the partly transparent sol-gel matrix prohibits distinction between parts that are actually electrochemically available and those which are fully sealed by lacquer, but still visible. Thus, to correlate composition with electrochemical reactivity Raman microscopy was used to distinguish between the respective components at the surface. The spectroscopic response of the lacquer matrix shows only weak peaks and fluorescence in the studied wavenumber region (not shown). As a result, the Raman microscopy focuses on the conductive additive, which provides strong spectroscopic features as shown in Figure 3b. The strong G-band at  $1584\text{ cm}^{-1}$  and the very weak D-band at  $1352\text{ cm}^{-1}$  are typical for the  $sp^2$  hybridization of graphite. Additionally, the D'-band can be found at  $1625\text{ cm}^{-1}$ . It can be assumed that the lacquer synthesis process may not harm the graphite material, however the abrasive polishing process could introduce some defects at the surface. Using this spectrum as a reference, information about the distribution of this component can be generated. At each position several Raman spectra were recorded in parallel to analyze the distribution of graphite. From the obtained data surface maps of the components were generated. As described in section 2.1, the sample was carefully defined to get a fitting overlay of Raman and electrochemical images. This allowed

to combine two independently obtained analytical results to improve the allocation, assignment and also the quantification of chemical components.

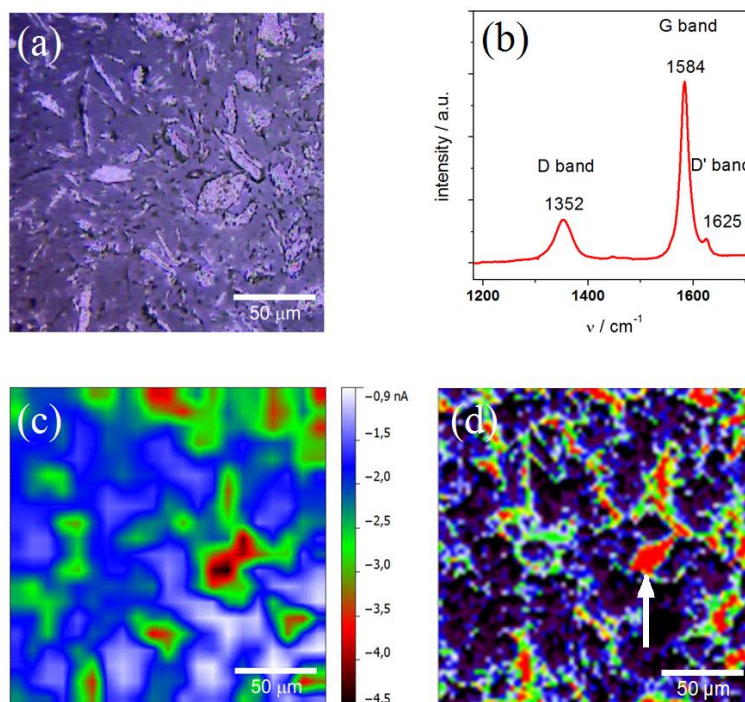


Figure 3: The surface of a NTC-G20 sample investigated by light microscopy (a), the Raman spectrum of graphite between 1200 and 1700  $\text{cm}^{-1}$  using 532 nm excitation (b), SECM image in feedback mode with 3  $\mu\text{m}$  tip to sample distance with  $E_{UME} = -0.15$  V vs.  $\text{Ag}|\text{AgCl}|\text{KCl}_{\text{sat.}}$  in 2 mM  $[\text{Fe}(\text{CN})_6]^{3-}$ , 100 mM KCl (parameters: x-/y-increment: 10  $\mu\text{m}$ , max. speed: 10  $\mu\text{m s}^{-1}$ , waiting time: 20 ms; red colors display high feedback currents and thus high conductivity) (c) and Raman microscopy image consisting of ca. 6000 evaluated single spectra showing the distribution of the spectrum shown in (b) where the red colored areas correlate > 90%, the white arrow indicates the position of a 20 x 20  $\mu\text{m}$  graphite particle (d).

Comparing the SECM image at 3  $\mu\text{m}$  tip to sample distance with the Raman image (Figures 3c and d), significant differences between the graphite particles shape and distribution and the mapping of the feedback current are visible. Not all graphite particles identified by Raman microscopy correspond to reactive areas indicated by the UME feedback current. It is assumed that some carbon particles or only parts of them are covered by a thin isolating layer of lacquer or are not linked to the conductive network in the lacquer matrix. It may also be that the amount of carbon at the position probed by the UME is too low. All these effects would result in a negative feedback. As discussed above, in case the probed position consists of graphite particles only, a pure positive feedback would be obtained, indicating high conductivity and fast electron transfer kinetics. As an example, a single  $\sim 20 \times 20 \mu\text{m}$  electrochemically available graphite particle or agglomerate is indicated in Figure 3d (white arrow) showing enhanced reactivity in the SECM feedback experiment, which can be clearly identified by Raman microscopy. From the obtained complementary results, it can be concluded that graphite particles are

homogeneously distributed within the insulating sol-gel matrix. Individual parts are exposed to the surface and can act as electrochemically reactive spots.

### 5.3.3 Correlating surface conductivity and electrocatalytic activity

To correlate distribution of active material and reactivity with electrochemical activity for antifouling purpose, laterally resolved SG/TC experiments were performed. Besides activity we were focusing also on the selectivity with respect to the anodic oxidation of water in the presence and in the absence of chloride (equations 1 and 2 and 4-6), since this selectivity and may have strong consequences for the technical application of the layers in electrochemical antifouling. Therefore, it was necessary to evaluate the UME response towards the respective reaction products (chlorine, oxygen) produced at the graphite-containing lacquer. Cyclic voltammograms were recorded at the UME in the absence and in the presence of chlorine and oxygen.

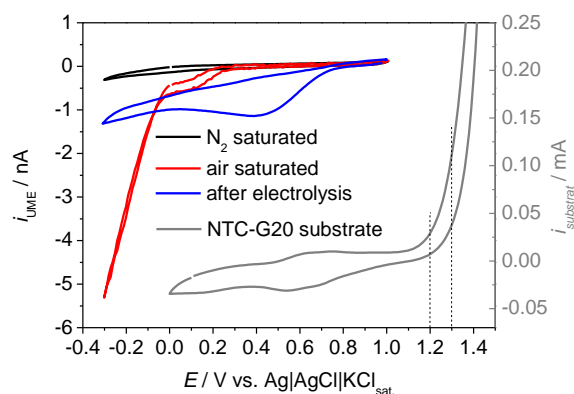


Figure 4: CVs obtained at a 10  $\mu\text{m}$  Pt UME in a 1 M KCl solution (pH = 8) purged with nitrogen (black) or air (red). The blue curve was obtained after 10 min of electrolytic chlorine evolution by polarizing the substrate to 1.6 V vs.  $\text{Ag}|\text{AgCl}|\text{KCl}_{\text{sat}}$ , the grey curve in the lower-right-hand corner shows a CV of the NTC-G20 substrate in the same solution. The potentials applied to the substrate in the following SG/TC experiments of SECM are marked with dashed lines. The scan rate was  $50 \text{ mV s}^{-1}$  in all cases.

Figure 4 shows cyclic voltammograms recorded in 1 M KCl (pH = 8) with the respective gas dissolved. The black curve shows the UME response in the solution purged with inert gas (nitrogen) and only double layer features can be found. After saturating the solution with air, reductive currents at potentials  $< 0.2 \text{ V}$  are observed (red line). These reductive currents are attributed to the oxygen reduction reaction. In the absence of oxygen (purging with nitrogen) and after 10 min of polarizing the sample electrode to 1.6 V vs.  $\text{Ag}|\text{AgCl}|\text{KCl}_{\text{sat}}$  for chlorine production, a voltammograms (blue line) was recorded at the Pt UME. Here, the cathodic reduction starts at a potential around 0.9 V indicating the presence of chlorine. A maximum of

the reductive current can be found at 0.4 V. Thus, the potential to detect chlorine was set to 0.4 V, which is still far away from the beginning oxygen reduction. Furthermore, the sum of oxygen and chlorine was detected at -0.3 V.

Suitable substrate potentials for the SG/TC experiments were chosen based on a substrate CV recorded between 0 and 1.5 V in the very same solution (Figure 4, grey curve). A strong anodic current dominates the CV beginning at potentials of 1.1 V beside double layer charging and features attributed to surface functional groups (~0.6 V). From this CV, 1.2 V and 1.3 V were chosen for the SG/TC experiments to study the beginning gas evolution and in particular to avoid gas bubble formation which would occur at higher potentials (~1.5 V).

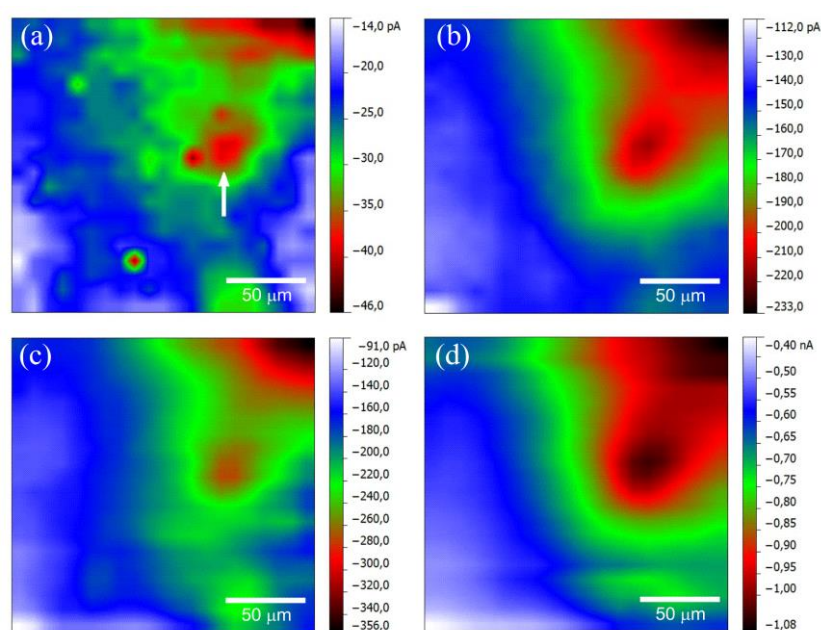


Figure 5: SECM measurements in SG/TC mode with 3  $\mu\text{m}$  tip to sample distance (parameters: X-/Y-increment: 10  $\mu\text{m}$ , max. speed: 10  $\mu\text{m s}^{-1}$ , waiting time: 20 ms,  $E_{\text{UME}}/E_{\text{S}}$ : 0.4 V/1.2 V (a); -0.3 V/1.2 V (b); 0.4 V/1.3 V (c); -0.3 V/1.3 V (d) all potentials vs.  $\text{Ag}|\text{AgCl}|\text{KCl}_{\text{sat}}$  reference electrode, the solution was saturated with  $\text{N}_2$  during the experiment and the white arrow in (a) shows the very same position as in Figure 3d. Please note the different tip current scales, which were chosen to clearly demonstrate distribution of activity.

SECM images of the SG/TC measurements with tip and substrate polarized to the above-mentioned potentials are shown in Figure 5. These measurements were carried out at exactly the same area as those shown in Figure 3. As described in the experimental part, the feedback mediator solution was carefully removed, the cell cleaned with water several times and again filled with 1 M KCl (pH = 8) whereby the UME remains at the same position and the same tip to sample distance as in Figure 3. In Figures 5a and b the substrate electrode potential ( $E_{\text{S}}$ ) was adjusted to 1.2 V and in 5c and d to 1.3 V, with the left figures (a and c) indicating chlorine formation at the substrate (UME polarized to 0.4 V), while the right figures indicate both chlorine and oxygen formation (UME polarized to -0.3 V). The much higher tip currents of

Figure 5b compared to Figure 5a as well as of 5d compared to 5c (please note the different current scales used in Figure) allows the conclusion that at -0.3 V both chlorine and oxygen are detected by the UME. Furthermore, the strong increase of the UME current is in accordance with the exponential increase of the substrate current (cf. Figure 4, grey curve) in this potential region. Since dissolve oxygen from air was eliminated by constant nitrogen flushing, the fact that the image representing chlorine evolution displays lower currents than that indicating both chlorine and oxygen evolution demonstrates that oxygen and chlorine were simultaneously generated both at 1.2 and 1.3 V at individual lateral positions at the sample electrode. Furthermore, the images show an inhomogeneous distributions of the UME currents (and conversely oxygen and chlorine generation) over the sample area with sharp contours. The contours of active spots seem to be reproducible even after changing the potential. For the sake of completeness, SECM images at OCP ( $\sim 0.6$  V) were obtained at both UME potentials (not displayed) and no structures or contours as in Figure 5 were found but rather a homogeneous surface with noise in the range of a few pA. In Figure 3a a single graphite particle or agglomerate ( $20 \times 20 \mu\text{m}$ ) is indicated (white arrow) which was identified as large graphite particle by Raman spectroscopy and which already showed high conductivity during the SECM feedback experiment. The position of the particle at the surface is also shown in the SG/TC experiment (Figure 5a) where in comparison to the surrounding area increased chlorine evolution can be found. Obviously, at the chosen potential the apparent beginning of the chlorine/oxygen evolution reaction can be observed. Increasing the potential, the UME current increases and the sharp contours start to fade due to diffusion of the chlorine molecules into the solution. Comparing Figure 5 with Figure 3c, the identified particle can be considered as an electrochemical active domain or “hot-spot” that is creating chlorine and oxygen and concomitantly a pH level change.

As reported elsewhere, the same graphite sol-gel lacquer was successfully applied in long-term seawater tests of an electrochemical antifouling procedure to prevent the growth of barnacles and mussels [48]. From this results and those of the present study, we can conclude that active domains in the size of several tens of micrometers providing combined redox and pH stress are obviously sufficient to avoid the settlement of marine organisms at the relevant areas.

## 5.4 Conclusion

This work demonstrates that scanning electrochemical microscopy can resolve the electrochemical activity and conductivity distribution of conductive particles in a non-

conductive matrix at the micrometer range. The conductive areas of the coating attributed to incorporated graphite particles correlate well with the component distribution found by Raman mapping and the chlorine/oxygen formation detected at various substrate potentials in the SG/TC mode. It can be assumed that these several micrometers large, electrocatalytically active hot spots, which are formed in the insulating matrix, constitute the electrodes where various electrochemical processes can hinder the settlement of organisms. However, to perform the electrochemical and spectroscopic correlation, a careful sample preparation is necessary to investigate the very same area.

From a more general point of view, this combination of Raman microscopy and scanning electrochemical microscopy is demonstrated to be a powerful tool in the investigation of heterogeneous electrode surfaces which might find further application e.g. in the investigation of chlorine electrolysis, oxygen reduction, and oxygen evolution electrodes, where a detailed knowledge of component, activity and conductivity distribution might help to improve the manufacturing processes of such electrodes.



## 5.5 References

- [1] H.-C. Flemming, *Biofouling bei Membranprozessen*, Springer, Berlin, 1995.
- [2] H.-C. Flemming, *Appl. Microbiol. Biotechnol.* 59 (2002) 629–640.
- [3] L.D. Renner, D.B. Weibel, *MRS bulletin* 36 (2011) 347–355.
- [4] H.-C. Flemming, in: H.-C. Flemming, J. Wingender, U. Szewzyk (Eds.), *Biofilm Highlights*, Springer, Berlin, 2011, pp. 81–109.
- [5] M. Wahl, *Mar. Ecol. Prog. Ser.* 58 (1989) 175–189.
- [6] S. Cao, J. Wang, H. Chen, D. Chen, *Chin. Sci. Bull.* 56 (2011) 598–612.
- [7] K. V. Passen, G. Van Meel, G. Thues, *Development of an integrated approach for the removal of tributyltin (TBT) from waterways and harbors: prevention, treatment and reuse of TBT contaminated sediments.: LIFE02 ENV/B/000341*, Antwerp Port Authority, 2008.
- [8] S. Nakasono, J.G. Burgess, K. Takahashi, M. Koike, C. Murayama, S. Nakamura, T. Matsunaga, *Appl. Environ. Microbiol.* 59 (1993) 3757–3762.
- [9] M. Okochi, T. Matsunaga, *Electrochim. Acta* 42 (1997) 3247–3250.
- [10] H. Wake, H. Takahashi, T. Takimoto, H. Takayanagi, K. Ozawa, H. Kadoi, M. Okochi, T. Matsunaga, *Biotechnol. Bioeng.* 95 (2006) 468–473.
- [11] M. Dargahi, Z. Hosseinidoust, N. Tufenkji, S. Omanovic, *Colloid. Surface. B* 117 (2014) 152–157.
- [12] T. Nakayama, H. Wake, K. Ozawa, H. Kodama, N. Nakamura, T. Matsunaga, *Environ. Sci. Technol.* 32 (1998) 798–801.
- [13] J. Guezennec, N.J.E. Dowling, J. Bullen, D.C. White, *Biofouling* 8 (1994) 133–146.
- [14] M. Eashwar, G. Subramanian, P. Chandrasekaran, S.T. Manickam, S. Maruthamuthu, K. Balakrishnan, *Biofouling* 8 (1995) 303–312.
- [15] R.E. Pérez-Roa, M.A. Anderson, D. Rittschof, C.G. Hunt, D.R. Noguera, *Biofouling* 25 (2009) 563–571.
- [16] P. Stoodley, D. de Beer, H.M. Lappin-Scott, *Antimicrob. Agents Chemother.* 41 (1997) 1876–1879.
- [17] S. Sandrock, E.-M. Scharf, K. Reiter, A. Franz, E. Günther, *European patent*, EP1570010 B1, 2003.
- [18] S. Sandrock, E.-M. Scharf, K. Reiter, A. Franz, E. Günther, *Schiff & Hafen* 10 (2002) 212–214.
- [19] U. Spohn, M. Rühl, S. Ackermann, M. Fütting, S. Sandrock, E.-M. Scharf, S. Kunsch, *European patent*, EP 14178516.1-1302, 2015.
- [20] U. Spohn, M. Rühl, S. Ackermann, N. Kamjunke, M. Altschner, S. Sandrock, G. Wagner, M. Fütting, *Gesteuertes Antifoulingschichtsystem aus Nanokompositen für die Schifffahrt (GANaS): Abschlußbericht zum Projekt IN7542 – GANAS*, Bundesministeriums für Wirtschaft und Technologie (BMWi), 2013.
- [21] S. Sandrock, E.-M. Scharf, H. Schubert, *German patent*, DE4109198C2, 1992.
- [22] T. Shimada, S. Kubota, T. Yanase, T. Nagahama, *Carbon* 67 (2014) 300–303.
- [23] F. Dubois, C. Mendibide, T. Pagnier, F. Perrard, C. Duret, *Corros. Sci.* 50 (2008) 3401–3409.
- [24] N. Kirkland, T. Schiller, N. Medhekar, N. Birbilis, *Corros. Sci.* 56 (2012) 1–4.
- [25] M.S. Amer, L. Durgam, M.M. El-Ashry, *Mater. Chem. Phys.* 98 (2006) 410–414.
- [26] A.J. Bard, F.-R. Fan, D.T. Pierce, P.R. Unwin, D.O. Wipf, F. Zhou, *Science* 254 (1991) 68–74.
- [27] A.J. Bard, M.V. Mirkin (Eds.), *Scanning electrochemical microscopy*, 2nd ed., CRC Press, Boca Raton, Fla, 2012.

- [28] S. González, J.J. Santana, Y. González-García, L. Fernández-Mérida, R.M. Souto, *Corros. Science* 53 (2011) 1910–1915.
- [29] S.S. Jamali, S.E. Moulton, D.E. Tallman, M. Forsyth, J. Weber, G.G. Wallace, *Corros. Science* 86 (2014) 93–100.
- [30] D. Sidane, M. Touzet, O. Devos, M. Puiggali, J. Larivière, J. Guitard, *Corros. Science* 87 (2014) 312–320.
- [31] A.R. Zeradjanin, T. Schilling, S. Seisel, M. Bron, W. Schuhmann, *Anal. Chem.* 83 (2011) 7645–7650.
- [32] A.R. Zeradjanin, N. Menzel, W. Schuhmann, P. Strasser, *Phys. Chem. Chem. Phys.* 16 (2014) 13741–13747.
- [33] A. Minguzzi, M.A. Alpuche-Aviles, J.R. López, S. Rondinini, A.J. Bard, *Anal. Chem.* 80 (2008) 4055–4064.
- [34] L.-Å. Näslund, C.M. Sánchez-Sánchez, Á.S. Ingason, J. Bäckström, E. Herrero, J. Rosen, S. Holmin, *J. Phys. Chem. C* 117 (2013) 6126–6135.
- [35] J.-H. Zhong, J. Zhang, X. Jin, J.-Y. Liu, Q. Li, M.-H. Li, W. Cai, D.-Y. Wu, D. Zhan, B. Ren, *J. Am. Chem. Soc.* 136 (2014) 16609–16617.
- [36] A.G. Guell, A.S. Cuharuc, Y.-R. Kim, G. Zhang, S.-y. Tan, N. Ebejer, P.R. Unwin, *ACS Nano* 9 (2015) 3558–3571.
- [37] M. Etienne, M. Dossot, J. Grausem, G. Herzog, *Anal. Chem.* 86 (2014) 11203–11210.
- [38] L. Valdes, *Proc. IRE* 42 (1954) 420–427.
- [39] I. Miccoli, F. Edler, H. Pfnür, C. Tegenkamp, *J. Phys.: Condens. Matter* 27 (2015) 223201.
- [40] Y. Lu, N. Bowler, J.R. Bowler, Y. Huang, *J. Phys. D: Appl. Phys.* 42 (2009) 135004.
- [41] M.V. Mirkin, F.-R.F. Fan, A.J. Bard, *J. Electroanal. Chemistry* 328 (1992) 47–62.
- [42] C. Wei, *J. Electrochem. Soc.* 142 (1995) 2523–2527.
- [43] K.B. Holt, A.J. Bard, Y. Show, G.M. Swain, *J. Phys. Chem. B* 108 (2004) 15117–15127.
- [44] C.E. Banks, R.R. Moore, T.J. Davies, R.G. Compton, *Chem. Commun.* (2004) 1804–1805.
- [45] C.E. Banks, T.J. Davies, G.G. Wildgoose, R.G. Compton, *Chem. Commun.* (2005) 829–841.
- [46] G. Wei, W. Su, Z. Wei, X. Fan, J. Liu, C. Yan, *Electrochimica Acta* 204 (2016) 263–269.
- [47] X. Ji, C.E. Banks, A. Crossley, R.G. Compton, *Chemphyschem* 7 (2006) 1337–1344.
- [48] U. Spohn, S. Ackermann, C. Morig, S. Sandrock, E.-M. Scharf, N. Kamjunke, S. Kunsch, M. Fütting, A. Heilmann, in: D. Beckmann, S. Kaufhold (Eds.), *Technische Systeme für die Lebenswissenschaften*, 17. Heiligenstädter Kolloquium, pp. 111–118.

## 6 SECM for the characterization of carbon materials

*The content of this part has been published as*

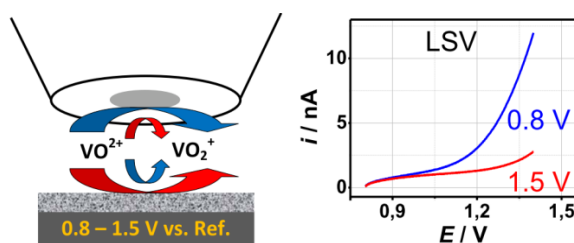
### **A linear sweep voltammetric procedure applied to scanning electrochemical microscopy for the characterization of carbon materials towards the vanadium(IV)/(V) redox system**

*Reproduced from M. Steimecke, S. Rümmler, M. Kühhirt, M. Bron, ChemElectroChem 2016, 3, 318-322 with permission from John Wiley and Sons, Copyright © 2016.*

**DOI: 10.1002/celec.201500386**

#### Abstract

A linear sweep voltammetric procedure applied to scanning electrochemical microscopy is presented to investigate carbon materials towards their activity for vanadium redox reactions of relevance for redox flow batteries. A linear sweep voltammetric experiment is performed at an ultramicroelectrode (UME) in close distance to an electrocatalytically active material, triggering a competition situation where both the UME and the material compete for the same molecule ( $\text{VO}^{2+}$ ). Depending on the redox activity of the catalytic material at the applied potential and thus the consumption of  $\text{VO}^{2+}$ , a decreased current in the detection sweep at the UME is observed. After evaluating relevant experimental parameters using a glassy carbon electrode as substrate, the mode is applied to a commercial carbon material where its redox behavior was examined and compared with results from cyclic voltammetry. Finally, it is shown that the presented linear sweep voltammetry–scanning electrochemical microscopy (LSV-SECM) method can be used as a mean of visualizing catalytic activity.



## 6.1 Introduction

With the aim of achieving the turnaround in energy policy renewable energies such as wind energy or photovoltaics received much attention over the last years. In Germany the share of renewable energies has increased up to 27.8 % of the overall power generation in 2014.<sup>[1]</sup> However, their fluctuating availability calls for efficient energy storage methods beside transportation and energy saving approaches. Redox flow batteries are a promising part of the solution for efficient energy storage because of their relatively low cost, large capacity and scalability.<sup>[2]</sup> In particular, the all vanadium redox flow battery (VRFB) working with the  $V^{2+}/V^{3+}$  redox pair at the negative electrode and the  $VO^{2+}/VO^{2+}$  redox pair at the positive electrode received much attention over the last years. Low cross contamination due to the presence of the same element at both sides, low cost, long lifetime and high energy efficiency<sup>[3]</sup> are the major advantages of these systems. In contrast to other electrocatalytic reactions, which require noble-metal catalysts, carbon-based electrode materials such as felts, fleeces, non-wovens or other three-dimensionally linked conductive carbon fibers can be used as comparably cheap catalytic electrodes at both electrode sides of the VRFB, realizing a wide operation potential range with minimal hydrogen and oxygen evolution.<sup>[4]</sup> A variety of carbon materials, including surface-modified carbons that could be used in combination with these electrodes, have been investigated towards their ability for the electrochemical conversion of the  $V^{IV}/V^V$  redox couple, such as hydroxylated carbon fibers,<sup>[5]</sup> nitrogen-doped graphene<sup>[6]</sup> as well as precious metal catalysts.<sup>[7]</sup>

Scanning electrochemical microscopy (SECM) has developed into a state-of-the-art method in electrocatalysis research where beside other topics much of academic research is done on the fuel cell technology.<sup>[8]</sup> For example, the oxygen reduction reaction (ORR) has been examined via redox-competition SECM over noble<sup>[9]</sup> and non-noble metal catalysts<sup>[10]</sup> to determine their activities as well as to monitor intermediates, that is, hydrogen peroxide.

In this study, we present a voltammetric procedure operating in a competition mode which is designed for the characterization of carbon-based electrode materials towards the  $V^{IV}/V^V$  redox couple, which is known to be slower and more difficult to understand than the redox reaction at the negative electrode.<sup>[4,11]</sup> SECM tip voltammetry over conductive substrates has previously been used to study processes occurring at interfaces<sup>[12]</sup> and can provide information about products, reactants and kinetics.<sup>[13]</sup> Voltammetric procedures in combination with SECM have furthermore been used for studying fast changes in concentration profiles<sup>[14]</sup> or as an imaging

technique.<sup>[15]</sup> Similar to these methods we use a voltammetric experiment at the microelectrode to characterize the substrate electrode decorated with a catalyst film. To evaluate the suggested method, experiments were carried out with a bare glassy carbon (GC) electrode as proof of principle and to determine the influence of the scan rate. Afterwards, a porous carbon was examined for its potential dependent ability of oxidizing  $V^{IV}$  to  $V^V$ . Finally, it is shown that the suggested procedure applied to SECM can be used for visualizing the activity of a catalyst spot on a non-carbon electrode material as well.

## 6.2 Results and discussion

In order to enable characterization of carbon materials towards their ability of oxidizing  $\text{VO}^{2+}$  using SECM a number of experiments with different methods and conditions, such as constant potentials or pulse profiles, pH values, UME materials and so forth, were carried out by us. All of them resulted in unreliable or unreproducible results. In particular, applying a constant potential leads to a fast decay of the current at the UME. It turned out, however, that a voltammetric method is well-suited to investigate the catalytic activity of carbon electrodes and films.

To monitor the behavior of the UME and to determine a suitable potential range for the SECM investigations, cyclic voltammograms were recorded with and without the addition of  $\text{VO}\text{SO}_4$  (Figure 1). In contrast to technical applications the concentration of the redox active molecule  $\text{VO}\text{SO}_4$  was reduced to 10 mM due to the use of an UME and a  $\text{HSO}_4^-/\text{SO}_4^{2-}$  buffer (pH 2) was used to avoid pH changes during the LSV experiments.

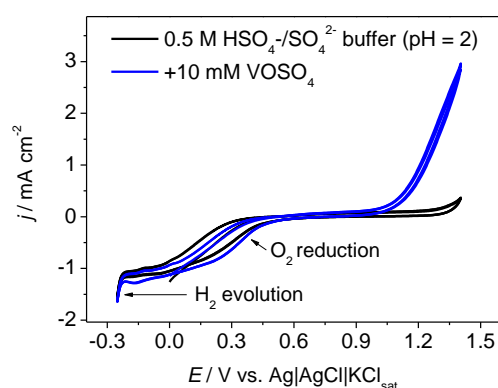


**Figure 1.** Cyclic voltammograms between -0.25 and 1.4 V vs.  $\text{Ag|AgCl|KCl}_{\text{sat.}}$  at  $10 \text{ mV s}^{-1}$  of the  $25 \mu\text{m}$  Pt UME in buffer solution (pH = 2) and after adding 10 mM  $\text{VO}\text{SO}_4$ .

In both CVs the reduction of oxygen from air ( $< 0.5 \text{ V vs. Ag|AgCl|KCl}_{\text{sat.}}$ ), which displays a well-pronounced diffusion limitation below ca.  $-0.1 \text{ V vs. Ag|AgCl|KCl}_{\text{sat.}}$  and which could be used to perform approach curves, as well as the evolution of hydrogen in the acid solution at the Pt UME ( $< -0.25 \text{ V vs. Ag|AgCl|KCl}_{\text{sat.}}$ ), can be observed. An additional increasing oxidation current is observed at potentials  $> 0.9 \text{ V vs. Ag|AgCl|KCl}_{\text{sat.}}$  in the solution containing 10 mM  $\text{VO}\text{SO}_4$ , which corresponds with prior studies at bulk Pt electrodes.<sup>[16]</sup> However, a diffusion limitation of this current, which would be quite typical for an UME response, cannot be observed even at more positive potentials and might be due to the oxygen evolution that is happening in competition to the  $\text{V}^{\text{IV}}$  oxidation at the Pt UME at  $E_{\text{UME}} > 1.3 \text{ V}$  or due to formed

adsorbates consisting of  $\text{SO}_4^{2-}$  and  $\text{HSO}_4^-$ -coordinated  $\text{V}^{\text{IV}}$  and  $\text{V}^{\text{V}}$  molecules.<sup>[16]</sup> Obviously, it is possible to detect  $\text{V}^{\text{IV}}$  species at the UME in solution using a potentiodynamic approach.

With the information from Figure 1 a competition experiment based on a linear sweep voltammetric (LSV) procedure at the UME was devised to characterize carbon electrode materials for their ability to oxidize  $\text{V}^{\text{IV}}$  to  $\text{V}^{\text{V}}$  in an indirect way. A single sweep from 0.8 to 1.4 V vs.  $\text{Ag}|\text{AgCl}|\text{KCl}_{\text{sat.}}$  was applied to the 25  $\mu\text{m}$  Pt UME as  $\text{VO}^{2+}$  detection sweep. Such linear sweep voltammograms were performed with different scan rates while the UME was placed 20  $\mu\text{m}$  above a GC plate electrode as substrate. To invoke the competition situation, different discrete values of constant potentials were applied to this GC electrode. It should be noted that between 75 – 100 LSVs (pretreatment) under the same conditions are necessary to be performed at the start of the experiment in order to create a reproducible response of the UME. During the pretreatment procedure (not shown) the linear sweeps are quite similar to those displayed later with the only difference of a decay in the maximum oxidation current with increasing sweep number. A strong decrease during the first 10 sweeps finally approaching a constant, stationary response is observed. In general, a pretreatment of the UME is always beneficial to equilibrate the electrode surface and to stabilize appearing adsorbates.<sup>[9]</sup>

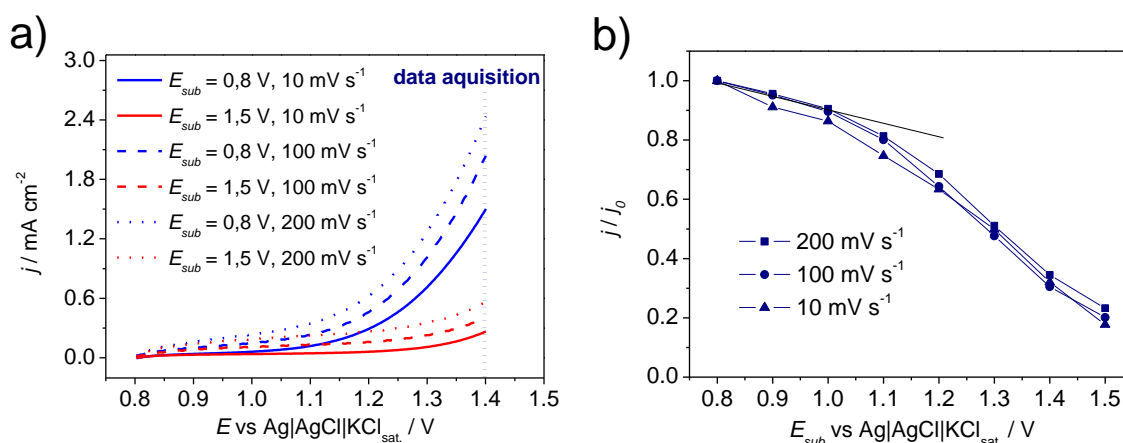


**Figure 2.** a) Linear sweeps voltammograms with different scan rates (10, 100 and 200  $\text{mV s}^{-1}$ ) in 10 mM  $\text{VO}_2^+$  buffer solution (pH = 2) performed at the UME, which was placed in 20  $\mu\text{m}$  distance above a GC electrode that was polarized to different potentials  $E_{\text{sub}}$  and b) the normalized current densities obtained at the last data point of the LSV (1.4 V vs.  $\text{Ag}|\text{AgCl}|\text{KCl}_{\text{sat.}}$ ) at different scan rates for all applied substrate potentials  $E_{\text{sub}}$ .

Afterwards the potential at the GC electrode is changed stepwise in positive direction while one detection sweep at the UME is performed for each substrate potential. The LSVs with scan rates of 10, 100 and 200  $\text{mV s}^{-1}$  at the UME while the substrate GC electrode is polarized to  $E_{\text{sub}} = 0.8$  and 1.5 V vs.  $\text{Ag}|\text{AgCl}|\text{KCl}_{\text{sat.}}$  are shown in Figure 2a.

The higher potential at the GC electrode results in lower oxidation currents during the LSV at the UME, which is attributed to the decreased concentration of  $V^{IV}$  in the UME diffusion field due to the consumption by the GC plate electrode. Based on Figure 2a the UME current at  $E = 1.4$  V was used for further evaluation as shown for different potentials of the GC electrode between  $E_{\text{sub}} = 0.8$  and 1.5 V in Figure 2b where the current densities were normalized to the value at 0.8 V ( $j_0$ ) for comparison. For the scan rates used ( $10 - 200 \text{ mV s}^{-1}$ ) at the UME the detection efficiency is scan-rate-independent. In summary, it is possible to use LSV experiments at the UME with constant potential at the substrate to invoke a competition suitable to investigate redox activity of the substrate for  $V^{IV}$  oxidation. All following experiments were performed with LSV scan rates of  $200 \text{ mV s}^{-1}$  to speed up the measurements. As mentioned above and shown in Figure 2 the GC itself seems to be active for the oxidation of  $V^{IV}$ , as during the detection sweep at the UME the current decreases with increasing potential applied to the GC electrode, resulting in a decrease of the concentration of  $V^{IV}$  in the diffusion field of the UME. The curve in Figure 2b seems to form a broad transition region with slow increase in catalytic activity with an ill-defined *onset* and  $V^{IV}$  still being detectable at 1.5 V. Nevertheless, an *onset* potential about 1.1 V can be determined for the GC electrode.

The thus established experimental procedure is applied in the following to a commercially available carbon material (HG3, see experimental section), and the results compared with those of cyclic voltammetry. Figure 3a shows the CVs of the bare cylindrical GC electrode (black) and the HG3 carbon in 0.1 M  $VOSO_4/3$  M  $H_2SO_4$  (blue), which is close to the technical requirements and in the 10 mM  $VOSO_4$ -buffer (pH 2) solution (red dashed), as used for the SECM experiments. The  $V^{IV}/V^V$  redox couple at the HG3 carbon film can be found at 0.98 for the oxidation and 0.90 for the reduction, which leads to a reversible potential of 0.94 V vs.  $Ag|AgCl|KCl_{\text{sat}}$  at pH  $\sim 0$ . The mechanism of the conversion of  $V^{IV}/V^V$  at carbon-based electrodes can be explained with covalent bond formation of the vanadium ions with surface groups, such as carboxyl groups, and a subsequent electron transfer.<sup>[17]</sup> Different contributions of the carbon structures as edges and basal plains are discussed.<sup>[18]</sup>



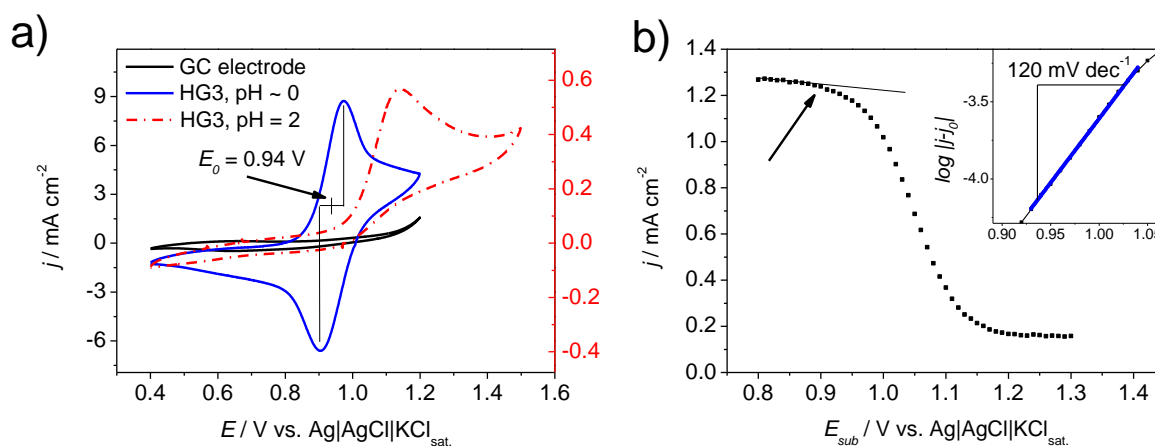


**Figure 3.** a) CVs of bare GC and HG3 carbon on a GC electrode in 0.1 M  $\text{VOSO}_4/3 \text{ M H}_2\text{SO}_4$  (pH  $\sim 0$ ) and in 10 mM  $\text{VOSO}_4$ -buffer solution (pH = 2) solution, scan rate  $50 \text{ mV s}^{-1}$  and b) current densities of the UME at 1.4 V vs.  $\text{Ag|AgCl|KCl}_{\text{sat.}}$  obtained via LSV above the HG3 sample on an ITO electrode ( $E_{\text{sub}}$ : 0.8 – 1.3 V vs.  $\text{Ag|AgCl|KCl}_{\text{sat.}}$ , increment 10 mV); inset: logarithmic normalized current densities of the transition region between 0.9 and 1.05 V.

The peak difference of 80 mV is an indicator of a good reversibility of the redox reaction catalyzed by the carbon material. In contrast, in the buffer solution (pH 2) only the oxidation of  $\text{V}^{\text{IV}}$  could be observed whereas the reduction peak is nearly absent. The peak potential of the oxidation could be determined as 1.14 V vs.  $\text{Ag|AgCl|KCl}_{\text{sat.}}$ , which is much higher than the expected change to more negative potentials. It can be concluded that under the chosen experimental conditions the redox behavior is deteriorated considerably when changing the pH to higher values as already described for  $\text{pH} > 1$ .<sup>[4]</sup>

To compare the results with the devised LSV-SECM procedure it was decided that, due to its own catalytic activity towards the  $\text{V}^{\text{IV}}/\text{V}^{\text{V}}$  redox reaction, GC electrodes should be avoided as substrate material for the LSV-SECM characterization of carbon materials towards this reaction. Another well-known electrode material, indium-doped tin oxide (ITO) on quartz glass, was therefore chosen as substrate to investigate the redox activity of the deposited carbon material. For an easier examination of the HG3 catalyst film and for positioning of the UME the electrochemical cell with the transparent electrode was mounted on an inverted microscope equipped with an SECM.

Figure 3b shows the current values from the linear sweeps at the UME (last data point at 1.4 V from LSV, similar to Figure 2) obtained at various potentials of the HG3 sample prepared on an ITO substrate ( $E_{\text{sub}}$ ). An S-shaped and nearly symmetric course with comparably well-pronounced *onset* and end are observed in contrast to the GC electrode experiments. In the beginning the current at the UME is only slightly decreasing until a certain *onset* potential

( $E_{\text{sub}} \sim 0.91$  V vs. Ag|AgCl|KCl<sub>sat.</sub>) is reached. Thereafter the current rapidly decreases as caused by the increasingly positive potential applied to the HG3 catalyst spot in 20  $\mu\text{m}$  distance of the UME and the resulting consumption of  $\text{VO}^{2+}$  ions. In the inset of Figure 3b a logarithmic plot of the normalized absolute current densities (initial current density at the UME  $j_0$  of 0.8 V vs. Ag|AgCl|KCl<sub>sat.</sub> was subtracted from all data) can be found for the transition region of the obtained data. The resulting plot shows linear behavior in the range of 0.9 – 1.05 V vs. Ag|AgCl|KCl<sub>sat.</sub> and the slope could be determined as 120 mV dec<sup>-1</sup>. This value may be used as a kinetic parameter that reflects the relative consumption of  $\text{V}^{\text{IV}}$  at the carbon-based material determined in an indirect way. Hence, the parameter provided by this method supplies a comparative value that can be used for analyzing and comparing different catalyst material. This method thus complements CV measurements, which, although providing valuable information about the system, suffer from the difficulty to determine the onset potential due to overlap with the capacitive currents. Furthermore, when going to practical catalysts investigated in thin-film configurations, peak separation in CV, which is often used as a parameter, in our experience strongly depends on film quality and thickness and thus might lead to erroneous results

The linear sweep voltammetric procedure applied to SECM allows a comparably simple way to determine the *onset* potential, which has been previously described for other catalytic reactions such as the oxygen evolution reaction (OER).<sup>[19]</sup> Furthermore it is demonstrated that the HG3 sample, which has been designed for electrochemical purposes, is a catalyst material with excellent features to be used as positive electrode in VRFB.

As demonstrated above, the suggested procedure combined with SECM may be used to characterize electrocatalysts towards their activity in the  $\text{VO}^{2+}$  redox reaction. However, certainly one strength of SECM is the possibility to perform spatially resolved experiments, for example, to investigate and visualize active site distribution over a planar electrode. As a proof of principle, the evaluated method was used as an imaging technique to visualize the activity of a spot of HG3 carbon deposited on an ITO electrode. After the pretreatment procedure, line scans of 1000  $\mu\text{m}$  with a step size of 25  $\mu\text{m}$  were performed and are displayed in Figure 4. In the regime of 0.8 – 1.10 V vs. Ag|AgCl|KCl<sub>sat.</sub> a good contrast between the catalyst film and the electrode material is visible as well as the increasing activity of the carbon spot. By approaching the UME to the catalyst spot the current decreases even before reaching the spot which is a result of already occurring conversation at the catalyst film and a hindered diffusion to the

center of the UME. The curve at 0.8 V even shows only minor contribution of the topography of the catalyst thin film ( $< 1 \mu\text{m}$ ). The current above the blank ITO electrode also decreases in the chosen potential range, possibly attributed to the consumption of  $\text{VO}^{2+}$  at the neighboring catalyst spot or the ITO electrode itself. In future studies this imaging method will allow to analyze and compare several catalyst spots or even arrays very quickly for their ability of oxidizing  $\text{VO}^{2+}$  to  $\text{VO}_2^+$ . Other applications might include monitoring activity distribution and degradation behavior over carbon-based electrodes.

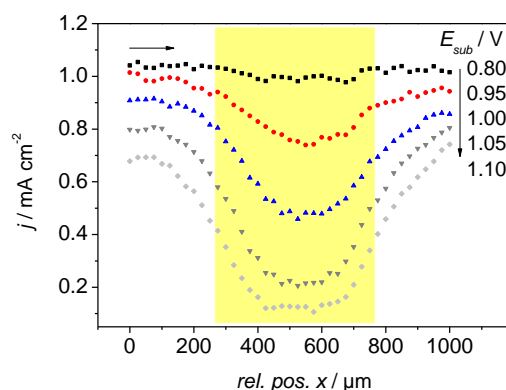


**Figure 4.** LSV-SECM line scans of a  $500 \mu\text{m}$  HG3 sample spot on ITO electrode at the very same position with different substrate potentials applied,  $E_{\text{sub}}$ : 0.80, 0.95, 1.00, 1.05 and 1.10 V vs.  $\text{Ag}|\text{AgCl}|\text{KCl}_{\text{sat.}}$ , the region highlighted in yellow represents the position of the catalyst spot determined from the optical image of the microscope, the arrow in the left corner indicates the scan direction.

### 6.3 Conclusion

The described LSV-SECM method expands the possibilities of characterizing materials for the  $\text{V}^{\text{IV}}/\text{V}^{\text{V}}$  redox reaction by using model experimental conditions. It allows analyzing catalytic activity and *on-set* potentials as well as activity distribution of catalyst spots by performing a LSV experiment at an ultramicroelectrode positioned close to the active materials. Initial data on kinetic parameters may also be obtained, although this method has to be evaluated further. The presented method is useful for imaging purposes and may finally help to identify materials which may be utilized as electrode in VRFB and to understand the redox process in more detail.

## 6.4 Experimental Section

### 6.4.1 Preparation of catalyst suspension

For thin film electrode preparation, 20 mg of Porocarb HG3 carbon (Hereaus AG, Germany) and 10  $\mu\text{L}$  Nafion 119 solution (5 % in lower aliphatic alcohols, DuPont, USA) were mixed with 2 mL acetone (Roth GmbH, Germany) and suspended in an ultrasonification bath for 4 h to create an ink. In case of the CV measurements in 0.1 M  $\text{VO}_2\text{SO}_4/3 \text{ M H}_2\text{SO}_4$  (see below) a similar ink but with 5  $\mu\text{l}$  Nafion was used.

### 6.4.2 Electrochemical experiments

A cylindrical GC electrode (4 mm diameter embedded in a PTFE cylinder) was used as substrate to investigate the porous carbon in a thin film configuration with cyclic voltammetry. Prior to thin film deposition it was cleaned with alumina oxide paste (1.0 and 0.3  $\mu\text{m}$ ) and water on a polishing cloth until a mirror finish was obtained. A 5  $\mu\text{l}$  aliquot of the catalyst ink was pipetted onto the GC electrode and slowly dried in an acetone atmosphere. Cyclic voltammetry of the carbon sample deposited onto the cylindrical GC electrode was performed with a Gamrypotentiostat PGI4 controlled by the Gamry Framework 2.67 software in a one compartment glass cell employing the catalyst-coated GC electrode as working electrode (WE), a Pt wire as counter electrode (CE) and an  $\text{Ag}|\text{AgCl}|\text{KCl}_{\text{sat}}$  reference electrode. Cyclic voltammograms (CV) were obtained in 0.1 M  $\text{VO}_2\text{SO}_4/3 \text{ M H}_2\text{SO}_4$  solution between 0.4 and 1.2 V vs  $\text{Ag}|\text{AgCl}|\text{KCl}_{\text{sat}}$ . and in 10 mM  $\text{VO}_2\text{SO}_4/0.5 \text{ M HSO}_4^-/\text{SO}_4^{2-}$  buffer between 0.40 and 1.55 V vs.  $\text{Ag}|\text{AgCl}|\text{KCl}_{\text{sat}}$ . with scan rates of 100  $\text{mV s}^{-1}$ . All electrochemical and SECM experiments were carried out at room temperature.

### 6.4.3 Scanning electrochemical microscopy

All SECM experiments were performed in a 0.5 M  $\text{HSO}_4^-/\text{SO}_4^{2-}$  buffer prepared with a 1:1 molar mixture of the potassium salt solutions creating a pH of 2. As vanadium(IV) source  $\text{VO}_2\text{SO}_4$  (Roth GmbH, Germany) was added to give a concentration of 10 mM. All solutions were handled in air and prepared with MilliQ water ( $< 0.055 \mu\text{S cm}^{-1}$ ).

For SECM measurements, two different materials were used as substrate electrodes: a glassy carbon plate (GC, Sigradur G, 1x1 cm, HTW Hochtemperatur Werkstoffe, Thierhaupten, Germany) and ITO on quartz glass (indium-doped tin oxide, 2x2 cm, pgo GmbH, Iserlohn, Germany). The GC was polished with 1  $\mu\text{m}$  and 0.3  $\mu\text{m}$  alumina paste and afterwards with

distilled water. The ITO electrode was pretreated with acetone, ethanol and water in an ultrasonification bath for several minutes and dried in air afterwards. For the preparation of catalyst spots on the ITO electrode 0.4  $\mu\text{L}$  of the catalyst ink was pipetted with a HPLC syringe into a perforated household tape (Tesa<sup>®</sup> with stamped hole  $\sim 500 \mu\text{m}$  in diameter) which was glued on the ITO electrode prepared earlier. After drying of the catalyst film the tape was carefully removed.

A scanning electrochemical microscope with software (Sensolytics GmbH, Bochum, Germany) and an Autolab bipotentiostat (Metrohm B. V., Netherlands) controlled by the Nova 1.9 software were used to perform the experiments employing the GC plate electrode as substrate. For investigation of the ITO electrode decorated with HG3 carbon a modified SECM instrument (Sensolytics GmbH, Bochum, Germany) mounted on an inverted optical microscope (DM 2500, Leica, Wetzlar, Germany) with a 3D-stage (Prior, UK, 0.5  $\mu\text{m}$  position resolution) and software control for x, y positioning was used, similar to a setup described by Oyamatsu.<sup>[20]</sup> A self-written script was realizing the execution of each LSV experiment, exporting and saving the data and the position change of the microelectrode in the imaging experiment. In all experiments a 25  $\mu\text{m}$  Pt ultramicroelectrode (UME, RG=10, Sensolytics GmbH, Bochum, Germany) was used as working (WE 1), a miniaturized Ag|AgCl|KCl<sub>sat</sub> (Metrohm, B. V., Netherlands) as reference and a coiled Pt wire as counter electrode. Either the GC electrode or the ITO electrode decorated with HG3 carbon was connected as second working electrode (WE 2). For all experiments, the UME was lowered to touch the electrode surface and then lifted up 20  $\mu\text{m}$ . In case of the ITO electrode the positioning of the UME above the HG3 sample could be easily controlled via the inverted microscope, however UME positioning was carried out in the same way before moving above the sample spot. Unless otherwise specified, LSV experiments at the UME were performed between 0.8 and 1.4 V vs. Ag|AgCl|KCl<sub>sat</sub> with 200  $\text{mV s}^{-1}$  after a 5 s quiet time while discrete values of substrate potentials ( $E_{\text{sub}}$ ) were applied to the GC plate or the catalyst coated ITO electrode and modulated in positive potential direction with either 100  $\text{mV step}^{-1}$  (GC) or 10  $\text{mV step}^{-1}$  (HG3 on ITO). To equilibrate the UME response 75–100 LSVs were carried out before the experiment started and again a resting time of 5 s was applied before each LSV. Line scans with a step size of 25  $\mu\text{m}$  were performed at different substrate potentials.

## 6.5 References

- [1] Bundesministerium für Wirtschaft und Energie (BMWi), *Anteil erneuerbarer Energien am Stromverbrauch bei 27,8 Prozent*, Berlin, **2015**.
- [2] C. Ponce de León, A. Frías-Ferrer, J. González-García, D. Szánto, F. Walsh, J. Power Sources **2006**, 160, 716–732.
- [3] a) M. Skyllas-Kazacos, J. Electrochem. Soc. **1986**, 133, 1057–1058. b) A. Parasuraman, T. M. Lim, C. Menictas, M. Skyllas-Kazacos, Electrochim. Acta **2013**, 101, 27–40.
- [4] M. Gattrell, J. Park, B. MacDougall, J. Apte, S. McCarthy, C. W. Wu, J. Electrochem. Soc. **2004**, 151, A123–A130.
- [5] L. Yue, W. Li, F. Sun, L. Zhao, L. Xing, Carbon **2010**, 48, 3079–3090.
- [6] L. Shi, S. Liu, Z. He, J. Shen, Electrochim. Acta **2014**, 138, 93–100.
- [7] S. Jeong, S. Kim, Y. Kwon, Electrochim. Acta **2013**, 114, 439–447.
- [8] W. Schuhmann, M. Bron in *In situ characterisation techniques for low temperature fuel cells* (Eds.: C. Hartnig, C. Roth), Woodhead Pub, Cambridge, **2012**.
- [9] K. Eckhard, X. Chen, F. Turcu, W. Schuhmann, Phys. Chem. Chem. Phys. **2006**, 8, 5359–5365.
- [10] a) A. O. Okunola, T. C. Nagaiah, X. Chen, K. Eckhard, W. Schuhmann, M. Bron, Electrochim. Acta **2009**, 54, 4971–4978. b) A. Dobrzeniecka, A. Zeradjanin, J. Masa, A. Puschhof, J. Stroka, P. J. Kulesza, W. Schuhmann, Catal. Today **2013**, 202, 55–62.
- [11] G. Orijji, Y. Katayama, T. Miura, J. Power Sources **2005**, 139, 321–324.
- [12] D. S. Schrock, D. O. Wipf, J. E. Baur, Anal. Chem. **2007**, 79, 4931–4941.
- [13] C. G. Zoski, C. R. Luman, J. L. Fernández, A. J. Bard, Anal. Chem. **2007**, 79, 4957–4966.
- [14] C. Hsueh, R. Bravo, A. J. Jaramillo, A. Brajter-Toth, Anal. Chim. Acta **1997**, 349, 67–76.
- [15] a) D. S. Schrock, J. E. Baur, Anal. Chem. **2007**, 79, 7053–7061. b) L. Díaz-Ballote, M. Alpuche-Aviles, D. O. Wipf, J. Electroanal. Chem. **2007**, 604, 17–25. c) M. A. Alpuche-Aviles, J. E. Baur, D. O. Wipf, Anal. Chem. **2008**, 80, 3612–3621.
- [16] G. Orijji, Y. Katayama, T. Miura, Electrochim. Acta **2004**, 49, 3091–3095.
- [17] a) B. Sun, M. Skyllas-Kazacos, Electrochim. Acta **1992**, 37, 1253–1260. b) M. Park, I.-Y. Jeon, J. Ryu, J.-B. Baek, J. Cho, Adv. Energy Mater. **2015**, 5, 1401550.
- [18] N. Pour, D. G. Kwabi, T. Carney, R. M. Darling, M. L. Perry, Y. Shao-Horn, J. Phys. Chem. C **2015**, 119, 5311–5318.
- [19] A. Maljusch, E. Ventosa, R. A. Rincón, A. S. Bandarenka, W. Schuhmann, Electrochem. Commun. **2014**, 38, 142–145.
- [20] D. Oyamatsu, N. Kanaya, H. Shiku, M. Nishizawa, T. Matsue, Sens. Actuators B **2003**, 91, 199–204.

## 7 Microwave-assisted functionalization of high-purity carbon nanotubes

*The content of this part has been published as*

### **The effect of rapid functionalization on the structural and electrochemical properties of high-purity carbon nanotubes**

*Reprinted from M. Steimecke, S. Rümmler, M. Bron, Electrochimica Acta 2015, 163, 1-8 with permission from Elsevier, Copyright © 2015.*

**DOI: 10.1016/j.electacta.2015.02.142**

#### Abstract

In this study the microwave-assisted functionalization of high purity carbon nanotubes (BayTubes<sup>®</sup>) with well-known oxidation agents such as 5 and 10 M nitric acid, 10 % hydrogen peroxide solution, a mixture of both, or 0.2 M potassium permanganate, is investigated and compared to CNTs treated by conventional oil bath heating. The obtained CNT materials are characterized with a variety of bulk and surface characterization techniques (XPS, Raman, TGA, TEM) and the obtained results could be correlated successfully with the severity of the treatment and the electrochemical properties of the CNTs. Depending on the oxidation agent oxygen containing functional groups are introduced into the CNTs where the chemical constitution of the functional groups in a hydrogen peroxide treated sample is significantly different from those by all other treatments. As a result the electrochemical behavior is strongly influenced which is clearly demonstrated by the absence of the quinone-type redox couple in this sample, which is found in all other samples. Finally, the time dependence of a nitric acid treatment is investigated and the obtained results allow setting up tailored procedures for functionalization of high purity carbon nanotubes resulting in materials with a controlled amount of oxygen containing functional groups that can be used for a variety of further synthesis steps.

## 7.1 Introduction

Commercially available carbon nanotubes like BayTubes<sup>®</sup>, which are characterized by small diameters and diameter distributions, a highly ordered structure and high purity (for BayTubes<sup>®</sup> >95 %) [1] have been studied in several fields of research and application such as (bio)polymer science [2,3] as conducting adhesive, energy storage materials [4] and catalyst supports [5]. Due to their high conductivity and improved stability resulting from the highly extended graphitic planes, high purity CNTs like BayTubes<sup>®</sup> are also of interest in electrocatalysis as support for precious [6] or as non-precious metal catalysts [7], e.g. for the oxygen reduction reaction in PEM fuel cells. However, when used as catalysts or catalyst supports the inert surface of CNTs is an obstacle and surface functionalization has to be carried out to introduce functional surface groups.

Modification of high surface area carbon materials has been studied over the last years [8,9] with the aim of creating in a controlled way surface functional groups. Oxidation in liquid phase with agents such as nitric acid, hydrogen peroxide, sulfuric acid, potassium permanganate and mixtures of them is the most common way of functionalizing carbon materials and leads to oxygen containing surface groups like alcohols/phenols, ketones, carboxylic acids and their derivatives [10]. These groups may serve as reactive sites for further synthesis steps (e.g. “grafting” of diamines [11,12]), however may also help in stabilizing active metal nanoparticles deposited onto the surface of these carbon materials. The thus prepared carbon supported metal particles may then serve as catalysts in a variety of catalytic applications, e.g. in proton exchange membrane (PEM) or direct methanol fuel cells (DMFC) [13] where they demonstrate enhanced activity and stability [14–16].

Beside functionalization, reactants such as nitric acid, hydrochloric acid or others are also often used in lower concentration as a mean of purifying the carbon nanotube synthesized via a CVD process. This treatment is often necessary to remove transition metals (Fe, Co, Ni) as well as support residuals (MgO, Al<sub>2</sub>O<sub>3</sub>), which result from the catalyst used in the CVD process [17,18]. By choosing a high purity CNT material this purification is no longer necessary. As it is our aim to introduce functional groups to the CNT material, non-oxidizing agents such as diluted hydrochloric acid are not considered in this work.

Typically, the above mentioned oxygen functionalization steps are carried out in liquid phase at elevated temperatures (e.g. under reflux) using conventional oil bath heating. The aim of the present contribution is to investigate microwave-assisted functionalization as a fast functionalization method for carbon nanotubes [19] with well-known oxidation agents and to



compare the results with the conventional method employing various characterization techniques such as thermogravimetric analysis for the amount of oxygen containing groups, XPS and BET for surface composition and morphology, Raman spectroscopy for defect analysis of the carbon structure, TEM for morphological information and finally electrochemical investigations. Of particular interest is the connection between the amount and type of introduced surface groups and their contribution to electrochemical and electrocatalytical behavior.

## 7.2 Experimental

### 7.2.1 CNT functionalization

Carbon nanotubes (BayTubes<sup>®</sup> C 150 P, Bayer Material Science AG, Leverkusen) were pretreated at 800 °C in Ar atmosphere for 30 min to obtain homogeneous starting material labeled CNT\_800. Afterwards, 500 mg CNT\_800 were suspended in 200 ml aqueous solutions of either nitric acid (“NA”), hydrogen peroxide (“HP”), mixtures of both (“NAHP”) or potassium permanganate (“PP”), respectively. The suspensions were placed in an ultrasonification bath for 15 min and finally treated under reflux (100 - 110 °C) either in a microwave oven (“Start”, MLS GmbH, Leutkirch) at a continuous irradiation power of 800 W (“MW”) or under conventional heating (“CH”) in an oil bath. After cooling down all prepared samples were washed with distilled water until pH = 7 using a centrifuge (5804, Eppendorf) for separation and dried at 100 °C in an oven in air, the sample treated with potassium permanganate was additionally treated with concentrated hydrochloric acid several times to remove remaining manganese oxides. Sample names reflecting the oxidizing agent and its concentration (e.g. “NA” – nitric acid, ”5” – 5 M), the treatment procedure and the resulting mass loss caused by treatment procedure and washing can be found in Table 1. In addition, treatments with nitric acid (5 and 10 M) were performed with different exposure times ranging from 15 to 120 min. The time in minutes is added to the sample name, e.g. samples NA\_5\_15 and NA\_10\_60 have been treated in 5 M nitric acid under microwave irradiation for 15 min or in 10 M nitric acid under microwave irradiation for 60 min, respectively.

### 7.2.2 Physical characterization

#### Thermogravimetric analysis (TGA)

Thermogravimetric analysis was carried out in an alumina crucible with a Netzsch STA449 F1 Jupiter<sup>®</sup> thermobalance. The heating chamber containing the sample was evacuated and flushed with Argon (Air Liquide, 99.999 %) several times to remove oxygen impurities. The measurements were performed under Argon flow (50 ml min<sup>-1</sup>) from room temperature to 1000 °C with a heating rate of 10 K min<sup>-1</sup>.

#### X-ray photoelectron spectroscopy (XPS)

Surface elemental analysis of all CNT samples was performed by XPS using a Kratos AXIS Ultra instrument with Al K<sub>α</sub> line (15 kV) as the X-ray source. The pass energy was 160 eV for survey spectra and 5 eV for spectra of selected binding energy regions. Photoelectron spectra

were recorded for the C1s, O1s states and additionally Mn 2p<sub>3/2</sub> for the PP\_02 sample. The quantification of the detected elements and the fitting of the oxygen species was performed using the Casa XPS software.

### **Surface area determination**

Surface area measurements by nitrogen adsorption were performed for selected CNT samples with a Sorptomatic 1990 (ThermoFinnigan). Prior to analysis the samples were heated under vacuum ( $10^{-5}$  mbar) to 120 °C for 24 h. Adsorption and desorption isotherms were measured at 77 K with N<sub>2</sub> as adsorbate at relative pressures P/P<sub>0</sub> of 0.05 to 0.3. The adsorption data was analyzed with the Brunauer–Emmett–Teller (BET) theory.

### **Electrochemical characterization**

Electrochemical measurements were carried out employing thin film electrodes. Electrode fabrication was done using CNT inks that were prepared by mixing 2.5 mg of CNTs with 150 µl of distilled water and 150 µl of isopropanol (Roth) containing Nafion<sup>®</sup> 117 solution (5 wt.% in lower aliphatic alcohols, Aldrich) (48:2, V<sub>isopropanol</sub>:V<sub>Nafion sol.</sub>). These mixtures were placed in a thermostated (20 °C) ultrasonic bath (Sonorex) for 1 h. During this time the samples were shaken manually several times to avoid aggregation of solid material at the bottom of the vessel. Afterwards a 5 µl aliquot of the ink was piped on a glassy carbon (GC) tip electrode (4 mm diameter embedded in a PTFE cylinder) resulting in a loading of 330 µg cm<sup>-2</sup>. Prior to use the GC tip was cleaned with alumina oxide polishing paste (1.0 and 0.3 µm) and water on a polishing cloth until a mirror finish was obtained.

Electrochemical measurements were performed with a Gamry potentiostat PGI4 controlled by the Gamry Framework 2.67 software in an one compartment glass cell employing the glassy carbon (GC) tip electrode coated with the sample (see above) as working electrode (WE), a Pt wire as counter electrode (CE) and a reversible hydrogen electrode (RHE) as reference electrode (RE). Cyclic voltammograms (CV) were obtained in N<sub>2</sub> flushed 0.1 M HClO<sub>4</sub> between 0.0 and 1.1 V vs. RHE. Linear sweep voltammetry with rotating disk electrode (RDE, OrigaTrod, France) was performed in O<sub>2</sub> saturated 0.1 M HClO<sub>4</sub> at room temperature. Prior to this, linear sweep voltammetry/RDE experiments were carried out in N<sub>2</sub> flushed 0.1 M HClO<sub>4</sub> and subtracted from those obtained in O<sub>2</sub> for double layer correction. Before recording CV and RDE curves, 50 cycles between 0.0 and 1.1 V vs. RHE were performed with 200 mV s<sup>-1</sup> to obtain stable voltammograms.

### **Raman spectroscopy**

An InVia Raman spectrometer setup (Renishaw) with a microscope, a Cobolt CW DPSS Laser (532 nm excitation wavelength), a 1800 l mm<sup>-1</sup> grating and a CCD camera detecting the Raman scattering was used for Raman spectroscopy. A thin layer of the samples was deposited on a glass slide and spectra were recorded with a x100 objective creating a laser spot size of ~1 μm on the sample surface.

### **Transmission electron microscopy**

A LEO 912 OMEGA microscope operating at 120 kV was used for Transmission Electron Microscopy (TEM). A spatula tip's worth of sample was suspended in ~1 ml isopropanol and placed in an ultrasonic bath for a few minutes. Afterwards a drop of the solution was deposited on a 3.05 mm copper grid (300 mesh).

## 7.3 Results and discussion

### 7.3.1 Comparison of different oxidation agents

The mass loss of the differently functionalized CNTs during functionalization was determined by weighing the samples before and after in order to estimate to which extent oxidative decomposition of the samples occurs. Table 1 shows that the samples treated under the different procedures show comparably small mass losses between 2.6 and 5.2% of the initial CNT amount after the functionalization and washing process, suggesting that the major part of the commercial CNTs is stable against total oxidation in these media. Weight loss might probably be attributed to total oxidation of amorphous carbon and to sample handling, which may be partially compensated by a weight increase due to the introduction of functional groups (see below). An exception is the sample treated in 0.2 M potassium permanganate (PP\_02) with a mass loss of 42%. Since the additional washing with concentrated hydrochloric acid that was performed in this case in order to remove manganese oxide residuals cannot be the reason for this high loss, likely the total oxidation of larger parts of the CNT carbon to CO/CO<sub>2</sub> occurs besides surface functionalization with oxygen containing groups.

Table 1. Sample names with corresponding treatment agent and resulting mass losses.

sample name*	treatment procedure**	time / h	mass loss / %
NA_5	MW, 5 M HNO <sub>3</sub>	1	5.2
NA_10	MW, 10 M HNO <sub>3</sub>	1	4.2
NAHP_10	MW, 10 M HNO <sub>3</sub> + 10% H <sub>2</sub> O <sub>2</sub>	1	4.8
HP_10	MW, 10% H <sub>2</sub> O <sub>2</sub>	1	2.6
PP_02	MW, 0.2 M KMnO <sub>4</sub>	1	42.0
Ref_5	CH, oil bath, 5 M HNO <sub>3</sub>	6	4.0

\* NA – nitric acid, HP – hydrogen peroxide, PP – potassium permanganate, the number added to the sample name is dedicated to the concentration of the respective agent.

\*\* MW – microwave oven, CH – conventional heating (oil bath).

### Thermogravimetric analysis (TGA)

In order to estimate the amount of surface functional groups introduced by the oxidizing treatment TGA analysis was performed for all samples in inert gas up to 1000 °C. Under such high temperatures, oxygen containing functional groups decompose according to the following (or similar) equations:





Thus, the mass loss during TGA refers to the amount of oxygen containing groups and the TGA curve provides hints about the process of decomposition. Figure 1 shows decomposition curves of samples treated with different oxidation agents during TGA measurement from room temperature to 1000 °C. In all cases several decomposition steps of the surface functionalized carbon nanotubes are found, albeit poorly resolved, indicating different kinds of oxygen containing groups on the surface. However, for the sample treated with 10 % H<sub>2</sub>O<sub>2</sub> only (HP\_10), the individual decomposition steps are significantly less pronounced. In the literature, the mass loss in the region from room temperature up to 150 °C is described as the release of physisorbed water [20]. XPS investigations of CNT materials treated at different temperatures were reported, showing that the decomposition of carboxylic acids and the dehydration of phenolic groups can be observed in the range from 150 to 300 °C followed by the decomposition of aldehydes, anhydrides and esters up to 600 °C and finally ethers and quinones [10]. Further mass loss can be attributed to the decomposition of carbonyl groups observed at temperatures higher 700 °C, however the determination of decomposition products is more difficult at higher temperatures [21].

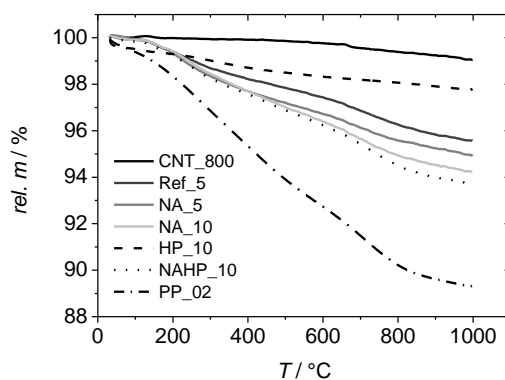


Figure 1. Decomposition curves of all samples, explanation of all names can be found in Table 1.

All residual masses after TGA measurement are summarized in Table 2. The CNTs pretreated at 800 °C, but not oxidized (CNT\_800) show only little mass loss (~1 %), indicating that there is a small amount of functional groups which either cannot be removed by the pretreatment step, or which form after the pretreatment during sample handling in air. The mass losses of the samples increase depending on the oxidizing agent beginning from 2.3 % in the HP\_10 sample (10% hydrogen peroxide) up to 10.7 % in the PP\_02 sample (0.2 M potassium permanganate).

This clearly demonstrates that the various oxidizing treatments lead to different degrees of surface modification.

Table 2. Mass loss during TGA measurements up to 1000 °C and mass specific surface area (SSA) from BET analysis for all samples.

sample	TGA	BET
	$\Delta m/\%$	SSA/m <sup>2</sup> g <sup>-1</sup>
CNT_800	0.9	169
HP_10	2.3	169
NA_5	5.1	188
NA_10	5.8	207
NAHP_10	6.3	227
PP_02	10.7	194
Ref_5	4.4	183

### Surface characterization (XPS, BET)

Surface characterization of the materials of this study was carried out with X-ray photoelectron spectroscopy (XPS), providing quantitative information on the surface composition of the samples.

Table 3. Surface atomic composition of the CNTs derived from XPS for characteristic binding energies of C 1 s (284 eV) and O 1 s (532 eV) (columns 2 and 3) and the contributing functional groups of the O 1s region (columns 4 and 5).

sample	XPS		C-O*	C=O**
	C 1 s (at%)	O 1 s (at%)	(532.8–533.8 eV)	(531.5–532.5 eV)
CNT_800	99.6	0.4	–	0.4
HP_10	98.4	1.6	1.1	0.5
NA_5	96.8	3.2	1.2	2.0
NA_10	95.8	4.2	1.6	2.6
NAHP_10	95.9	4.1	1.4	2.7
PP_02	93.3	6.7	1.9	4.8
Ref_5	97.2	2.8	1.1	1.7

\*(alcohols, ether), \*\*(ketones, aldehydes, carboxylic acids and their derivatives)

The XPS analysis results in Table 3 (3<sup>rd</sup> column) clearly show an incorporation of oxygen into the carbon material, whereby also in the pretreated sample (CNT\_800) some oxygen can be found, in agreement with TG measurements. The amount of oxygen strictly depends on the oxidation agent and its concentration, and correlates very well with the order derived from results of TGA analysis (Figure 1). The lowest amount of oxygen can be found in the HP\_10

and the highest in the PP\_02 sample. In the latter, no further manganese signal was observed. In order to analyze the nature and composition of the surface oxygen functional groups, the O 1s region (531.5 – 533.8 eV) was studied in more detail (Figure 2). All functionalized samples contain singly and doubly bound oxygen contributed by the different functional groups (Table 3, columns 4 and 5). The sample pretreated at 800 °C in Ar (CNT\_800) shows functional groups with doubly bound oxygen, e.g. ketones (Figure 2a) indicating their high stability [10], however their formation during handling in air cannot be excluded.

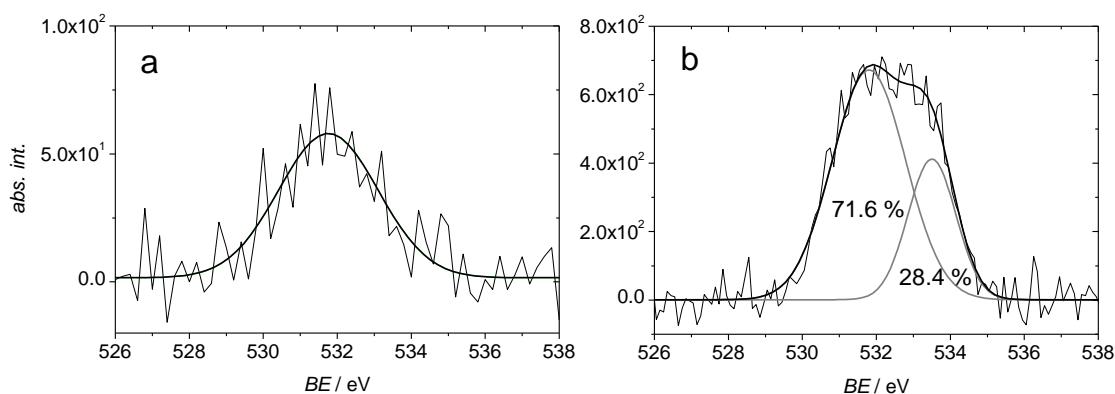


Figure 2. XPS O 1s region scans of the CNT\_800 (a) and PP\_02 sample where the fit contributing areas are given in % (b), both spectra are baseline corrected.

In contrast to all other functionalized samples the O 1s region of HP\_10 sample (10% hydrogen peroxide) is dominated by C–O single bonds (532.8 – 533.8 eV) which are due to the presence of alcohols and/or ethers at the surface of the CNT material. This would be in agreement with TG results, where the weight loss was more pronounced at lower temperatures. The amount of C=O-functionalities in HP\_10 is not higher than in CNT\_800 (heat treated starting material), suggesting that the hydrogen peroxide treatment does not lead to the introduction of further C=O-functional groups. In all other samples amount doubly bound oxygen (531.5 – 532.5 eV), as it can be found in aldehydes, ketones, carboxylic acids and their derivatives, is dominating the O 1s region from 60.7% in Ref\_5 (5 M nitric acid, 6 h conventional heating) up to 71.2% in PP\_02 (Figure 2b), in agreement with the observed mass loss of these samples at higher temperature [10]. The amount of C–O single bonds is also increased in these samples however, much less pronounced than the C=O double bonds.

The results of BET analysis show an increasing surface area depending on the oxidation agent and its concentration evoked by the oxidation process, which has also been described for other carbon materials [22]. The surface area (Table 2) correlates with the amount of oxygen functional groups from TGA and XPS with one important exception: the PP\_02 sample shows



lower surface area although the oxygen amount is higher than in all the other samples which could be due to the presence of groups containing more oxygen (e.g. carboxyl groups) [23] or remaining manganese compounds increasing the sample weight and thus suggesting lower SSA. However, this manganese could not be detected with the XPS measurements.

### Morphological characterization

To evaluate the influence of the comparably harsh treatments used in this study onto the morphology and tubular structure, TEM images and Raman spectra were recorded. The Raman spectra of all samples display very similar scattering patterns showing characteristic carbon features such as the D ( $\sim 1340\text{ cm}^{-1}$ ) that is due to the presence of disorder in the C–C lattice and the G band ( $\sim 1585\text{ cm}^{-1}$ ) that is strictly connected to  $sp^2$  hybridized carbon, as well as second order bands at higher wavenumbers [24]. Comparing the CNT\_800 and PP\_02 samples in the region from 1000 to 3000  $\text{cm}^{-1}$  (Figure 3) evident differences can be found in the decreased G band with an associated increase of the  $I_D/I_G$  ratio from 1.20 to 1.31, which can be taken as evidence for graphitic layer destruction. It can be concluded that even in the starting material the number of defects is already high and further incorporation of functional groups does not influence the spectra that much. Anyhow, the possibility to quantify structural defects on multi-walled CNTs is limited [25]. It can be assumed that most of the D and G band-intensities observed in the Raman spectra of the functionalized samples is contributed by the unchanged CNT structure of the inner layers of the multi-walled CNTs, which are possibly not affected by any of the treatment processes.

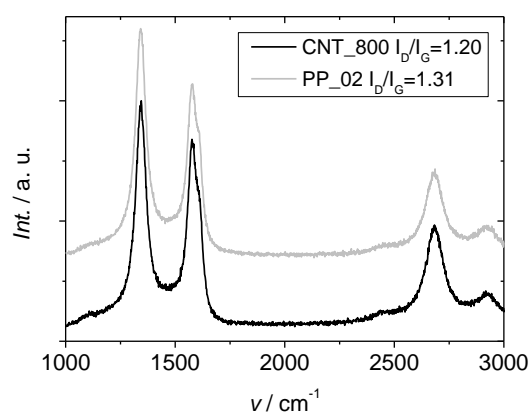


Figure 3. Raman spectra of CNT\_800 and PP\_02 sample obtained by 532 nm laser excitation (for an improved clarity an offset was applied to the PP\_02 sample curve).

TEM images were recorded in order to characterize the CNT structure after the different treatment processes. In the pretreated sample (CNT\_800) multi-wall carbon nanotubes with

outer diameters between 5 and 30 nm can be found (Figure 4a). Depending on the oxidation agent, in all functionalized samples homogeneously distributed layers of amorphous carbon [26] or carbonaceous coating [27] can be observed surrounding the hollow nanotube (Figure 4b and c) and sometimes also in the gaps between several nanotubes (Figure 4d). The material accumulated between the nanotubes might be similar to graphene oxide, which is usually prepared from graphite using potassium permanganate, and results from the oxidative destruction and exfoliation of the CNT structure. In all samples the tubular carbon nanotube structure is still present, in agreement with the Raman measurements (Figure 3). However, it can be concluded that due to the formation of amorphous material an oxidative treatment under the studied conditions cannot be used as purification step as described in other cases [28,29].

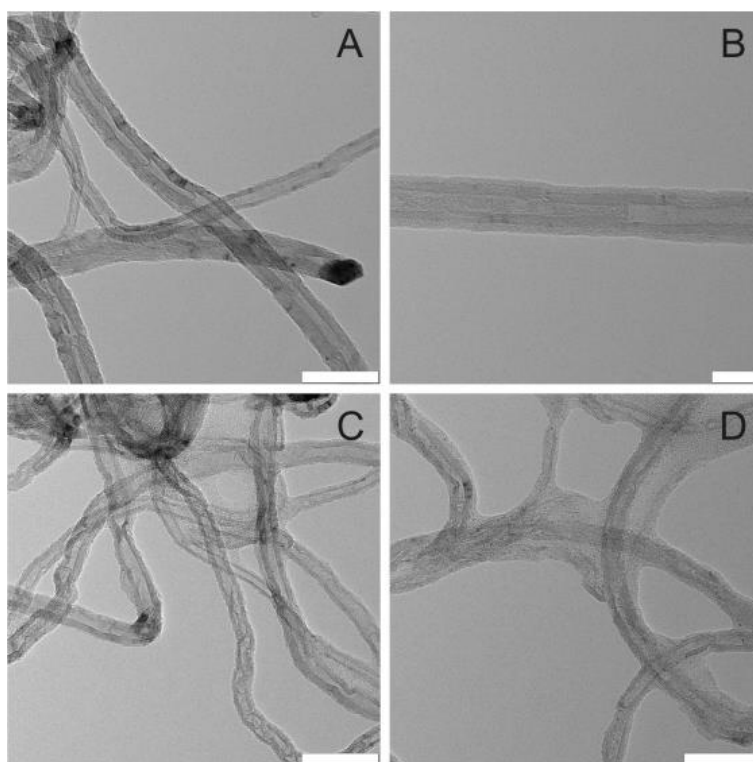


Figure 4. TEM images of CNT\_800 (a), NA\_10 (b), NAHP\_10 (c) and PP\_02 (d) samples, scale bars represent 50 nm (a, c, d) and 20 nm (b).

### **Electrochemical characterization (CV, RDE)**

Electrochemical characterization of the samples was carried out in order to gain insight into the surface properties and the electrochemical behavior of the CNTs. CVs of all samples except for the untreated (CNT\_800) and 10 % hydrogen peroxide treated (HP\_10) CNTs show an oxidation and reduction peak pair attributed to the presents of oxygen containing functional groups (quinone-type proposed) [30] between 0.5 and 0.7 V vs. RHE (Figure 5a), indicating successful functionalization. These peaks are considerably broad, indicating a multitude of

chemical surface states with different redox potentials. Additional redox peaks in the lower potential region can be found in the PP\_02 sample resulting from remaining manganese ions which obviously are present despite washing with concentrated hydrochloric acid [31]. XPS analysis did not show manganese signal, indicating that the amount of manganese species is very low or manganese is incorporated into the porous material but still electrochemically available.

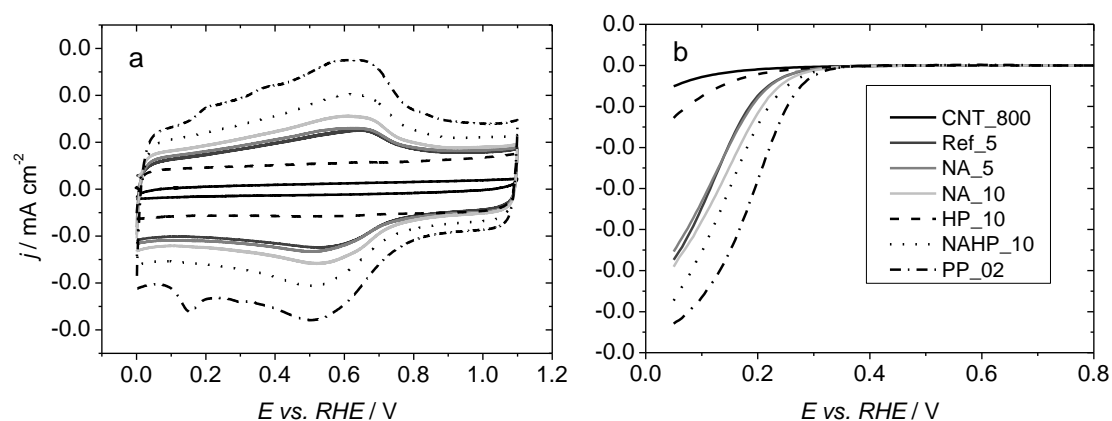


Figure 5. CVs of the differently modified CNTs in N<sub>2</sub> flushed 0.1 M HClO<sub>4</sub> at 100 mV s<sup>-1</sup> (a) and double layer corrected RDE polarization curves of all samples in O<sub>2</sub> sat. 0.1 M HClO<sub>4</sub> at 1600 RPM and 5 mV s<sup>-1</sup> (b).

The electrochemical results from Figure 5 shall now be correlated with the XPS data of Table 3. The latter suggests that the chemical nature of the surface functional groups formed by treatment with H<sub>2</sub>O<sub>2</sub> is different to those of the HNO<sub>3</sub> and KMnO<sub>4</sub> treatment. In agreement with this, the absence of the redox pair peaks in the HP\_10 sample indicates that this sample does not contain any quinone-type functional groups. On the other hand, this sample as well as the heat treated sample CNT\_800 contain small amounts of C=O double bonds, which do obviously not contribute to surface redox processes. However, the presence of a significant number of C=O double bonds as in all other samples leads to redox behavior to the carbon nanotube material as visible in the CVs of Figure 5a. Importantly, the intensity of the redox peak strongly correlates to amount of C=O double bonds as displayed in Table 4.

Thus, a clear correlation between XPS results and electrochemical behavior can be drawn. A quantification of this correlation however appears difficult, since the separation of the intensity of the redox peaks from the enhanced double layer capacity (DLC) is difficult due to difficulties in baseline determination (see also below).

Table 4. Maximum peak current densities extracted from the positive-going sweep of CV, the *onset* potentials at specific current density of all samples and the results of the bonding evaluation of the O 1 s region scan taken from Table 3 (n.d. – not determined).

<b>sample</b>	<b>CV (positive-going sweep)</b>	<b>RDE</b>	<b>C=O</b>
	<b>maximum peak current density/mA cm<sup>-2</sup></b>	<b>onset potential (at 1 mA cm<sup>-2</sup>)/V</b>	<b>(531.5 – 532.5 eV)/at%</b>
CNT_800	n. d.	n. d.	0.4
HP_10	only increased DLC	n. d.	0.5
NA_5	1.03	0.13	2.0
NA_10	1.24	0.15	2.6
NAHP_10	1.60	0.17	2.7
PP_02	2.19	0.21	4.8
Ref_5	1.01	0.13	1.7

Beside the intensity of the quinone-pair redox peaks, the current associated to the charging of the electrical double layer, the so-called double layer capacity (DLC) also strongly depends on the means of functionalization, as most clearly visible in the potential region around 1.0 V vs. RHE in Figure 5a. This double layer capacity, although strongly depending on surface chemical composition, for samples of similar chemical nature can be taken as a measure of surface area. The double layer capacities at 1.0 V vs. RHE for all samples are at least one magnitude higher than the untreated CNT\_800 sample (Figure 5a). For all other samples a connection between DLC and surface area can be drawn, as displayed in Figure 6 (empty triangles), with the exception of the sample PP\_02, which is attributed to possible disturbance in SSA determination (see above). A similar correlation can be found for the amount of oxygen (in functional groups) derived from XPS analysis and the DLC (Figure 6, black squares). Obviously, the higher the amount of functional groups the higher is the electrochemical DLC. We assume that that functional groups like –OH and –C=O significantly contribute to double layer capacitance. It is important to note that a strong correlation between nitrogen functionalization and DLC have even be reported for nitrogen-containing CNTs [32].

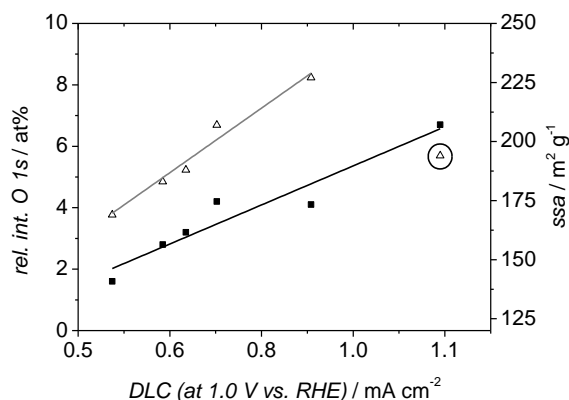


Figure 6. Relative intensity of the O 1s peak from XPS results (black squares) and mass specific surface areas (empty triangles) of all modified samples plotted against the double layer capacity (DLC) taken at 1.0 V vs. RHE; the circled triangle was excluded from the linearization.

Equal values for the surface area can be observed in the CNT\_800 and HP\_10 sample (Table 2) which is due to the obviously non-destructive treatment conditions: the introduction of singly bound oxygen requires the change from  $sp^2$  to  $sp^3$  hybridized carbon which is, although introducing some strain, not harming the C–C lattice that much. The surface area of all other samples increases in dependence of oxidation agent and/or concentration which can be explained by further C–C bonding cleavage during the functionalization process that is necessary for C=O double bond formation. This process harms the C–C ring structure and may finally lead to the total oxidation or the cleavage of CNTs under formation of graphene oxide-like sheets (see morphological characterization). The introduced defects in the outer walls of the CNTs will contribute to the increasing surface area.

Beside CVs, the oxygen reduction reaction (ORR) activity of the materials has been determined by rotating disk electrode experiments (Figure 5b) using linear sweep voltammetry (LSV). The aim of this study is to gain additional insight into the surface properties and the behavior of the materials in electrochemical systems. We are however not aiming at high activity since it is well known that oxygen-functionalized CNTs do not provide exceptional activity in acid solutions [30], but rather in alkaline media [33]. Double layer capacity, amount of oxygen functional groups and ORR activity (Figure 5b) are obviously related to each other and depend on the oxidation agent. The increase of oxygen containing functional groups leads to more reactive sites in the carbon material improving the ORR activity whereby the HP\_10 (10% hydrogen peroxide) samples is again markedly different. It can be assumed that the presents of functional groups with double bonded oxygen are much more active towards the ORR in acid solution than others. Comparing NA\_5, NA\_10 (5 and 10 M nitric acid) and NAHP\_10 (mixture of 10 M nitric acid and 10% hydrogen peroxide) also some contribution of the increasing

surface area (Table 2) can be assumed. The *onset* potential in the ORR polarization curves shifts to higher values (Table 4).

The highest one can be found again in the PP\_02 (0.2 M potassium permanganate) sample. Obviously the oxidation process forms catalytically active surface sites whose number increases with increasing oxygen content. This is in contrast to observations at non-high purity carbon nanotubes, where the *onset* potential shifts to more negative values after nitric acid treatment [30]. These differences are clearly attributed to the different starting materials and show again the influence of the quality of the used starting material. To evaluate on the necessity of purification steps in the CNTs used by us a CNT sample was pretreated in 5 M hydrochloric acid in the microwave oven for one hour as a reference which showed the same ORR activity as the pretreated CNT\_800 sample (data not shown). This additional experiment emphasizes again the high quality of the used starting material as it is known that the ORR activity is easily influenced by transition metal traces or other impurities. However, the complete removal of metal impurities (< 5%) from carbon materials is difficult and limited even with “super washing” methods [34]. Thus, our applied conditions of the electrochemical experiments were chosen deliberately to minimize the possible influence of introduced Mn impurities because it is known that electrocatalytic activity for oxygen reduction reaction is not enhanced by manganese oxide-based catalysts at pH = 1, opposite in alkaline solutions [35,36]. As a result it is assumed that the observed ORR activity of the PP\_02 sample is mainly caused by the introduced functional groups.

### **7.3.2 Time and concentration dependence of nitric acid treatment**

The above studies demonstrated that the microwave-assisted functionalization is a fast and straightforward tool to functionalize the surface of CNTs. By choosing different agents various degrees of functionalization, i.e. oxygen surface content can be induced, which relates to different electrochemical properties. However, similar to the results in literature a too strong oxidation of the CNTs surface leads to the destruction of the outer CNT layers and formation of amorphous layers. To further explore the possibilities of tuning the degree of surface functionalization, time dependence of nitric acid treatment, which is one of the most common methods for carbon modification and purification [37] has been investigated using microwave-assisted heat treatment.

## Thermogravimetric analysis

In addition to the one hour 5 and 10 M nitric acid treatment with microwave (NA\_5, NA\_10), the treatment time has been varied between 15 and 120 min. Decomposition curves of selected samples after 30 and 120 min treatment time and the Ref\_5 sample (5 M nitric acid, 6 h conventional oil bath heating) are displayed in Figure 7 where particularly the 120 min treated samples (NA\_5\_120, NA\_10\_120) show typical two step decomposition as described for the different oxidation agents before.

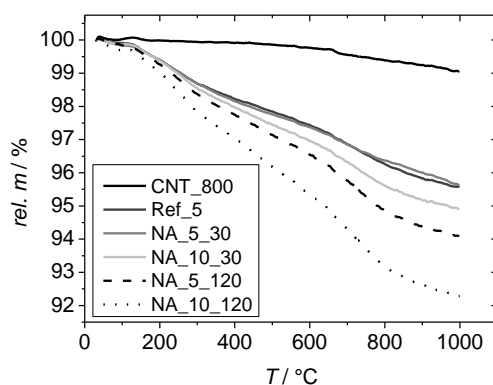


Figure 7. Selected decomposition curves of functionalized CNT samples; treatment time is added to the sample name “NA”, e.g. the NA\_5\_30 sample is treated with 5 M nitric acid for 30 min.

The time dependence of the corresponding mass loss can be found in Figure 8. With higher acid concentration and longer treatment time the amount of oxygen containing groups which can decompose during temperature treatment increases. The difference between 5 and 10 M nitric acid increases with longer treatment time and no plateau is reached for the sample treated with 10 M treated even after two hours of treatment. It can be noticed that 30 min microwave treatment lead to the same results as 6 h of conventional oil bath heating.

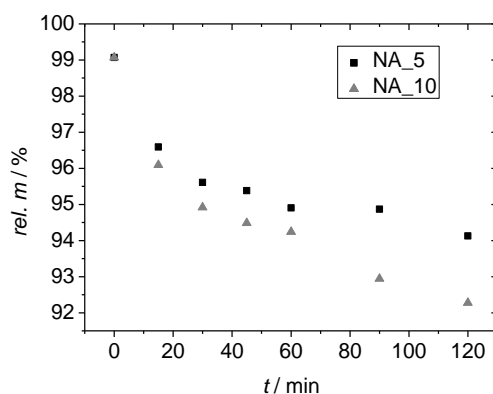


Figure 8. Residual masses after TGA measurement in argon of all CNT samples treated with 5 and 10 M HNO<sub>3</sub> depending on treatment time.

## Electrochemical characterization

Electrochemical characterization shows differences between 5 and 10 M acid treatment as already seen in the first part of this paper, where different oxidation agents have been used. Double layer capacity as well as the quinone-type redox peak maximum increase with longer treatment time and both are slightly higher in the 10 M samples (Figure 9). Redox peaks can already be observed after only 15 min treatment. The peak current density increases more strongly than the DLC indicating an increasing amount of introduced functional groups with treatment time. In the positive sweep of the CV the peak potential maximum slightly shifts with longer treatment time to lower potentials (~50 mV) indicating redox contribution of different functional groups and/or changing chemical surface composition. RDE curves (not displayed) show a similar dependency on treatment time, the longer the time the higher the maximum current density, which results from the increasing formation of active site introduced by the nitric acid. Samples of 90 and 120 min of 10 M nitric acid show the highest current densities, whereas in all samples the *onset* potential is hardly affected.

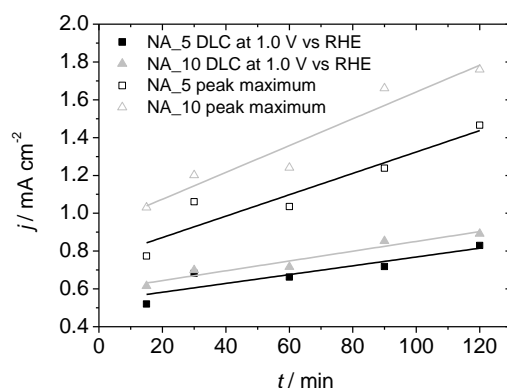


Figure 9. Current densities extracted from the positive sweep of CV for the DLC and the redox peak maximum in dependence of the time for 5 and 10 M nitric acid treatment.



## 7.4 Conclusion

High purity carbon nanotubes (BayTubes<sup>®</sup> C 150 P) were treated with different oxidation agents and procedures in a microwave oven where in all cases surface modification of the CNTs could be observed. The amount of surface functional groups introduced by microwave assisted functionalization and characterized by means of TGA, XPS analysis correlates with the electrochemical and electrocatalytic results however the number of oxygen containing surface groups on the carbon material is obviously limited due to the process of total combustion. The introduction of oxygen containing functional groups can be controlled by varying concentration of the agent and/or the microwave treatment time resulting in tailored procedures for predictable oxygen content. The results of Raman and TEM measurements showed that the nanotube structure itself can still be observed even after strong functionalization, while depending on the conditions used surrounding amorphous layers or even graphene oxide like sheets could be observed. Oxidation efficiency for one hour microwave treatment can be described as:

$0.2 \text{ M KMnO}_4 \gg 10 \text{ M HNO}_3/\text{H}_2\text{O}_2 \sim 10 \text{ M HNO}_3 > 5 \text{ M HNO}_3 > 10 \% \text{ H}_2\text{O}_2$  .

It can be highlighted here that the functionalization process using hydrogen peroxide is obviously different from all other means resulting in a domination of singly bound oxygen and related with it a different electrochemical behavior. Finally, microwave assisted functionalization in acidic media was at least ten times faster than functionalization under conventional heating and led to similar results.

It is assumed that these methods and their results can be adapted to other high purity carbon nanotube materials or even other carbons.

## 7.5 References

- [1] M. Bierdel, S. Buchholz, V. Michele, L. Mleczko, R. Rudolf, M. Voetz, A. Wolf, *Phys. Stat. Sol. (b)* 244 (2007) 3939–3943.
- [2] M. Sanchez-Garcia, J. Lagaron, S. Hoa, *Comp. Science Techn.* 70 (2010) 1095–1105.
- [3] M. Lahelin, M. Annala, A. Nykänen, J. Ruokolainen, J. Seppälä, *Comp. Sci. Techn.* 71 (2011) 900–907.
- [4] F. Markoulidis, C. Lei, C. Lekakou, E. Figgemeier, D. Duff, S. Khalil, B. Martorana, I. Cannavaro, *IOP Conf. Ser.: Mater. Sci. Eng.* 40 (2012) 12021.
- [5] A. Villa, D. Wang, P. Spontoni, R. Arrigo, D. Su, L. Prati, *Catal.Today* 157 (2010) 89–93.
- [6] F. Hasché, M. Oezaslan, P. Strasser, *Phys. Chem. Chem. Phys.* 12 (2010) 15251.
- [7] A. Zhao, J. Masa, M. Muhler, W. Schuhmann, W. Xia, *Electrochim. Acta* 98 (2013) 139–145.
- [8] K. Balasubramanian, M. Burghard, *Small* 1 (2005) 180–192.
- [9] W. Shen, Z. Li, Y. Liu, *Rec. Pat. Chem. Eng.* 1 (2008) 27–40.
- [10] S. Kundu, Y. Wang, W. Xia, M. Muhler, *J. Phys. Chem. C* 112 (2008) 16869–16878.
- [11] L. Yang, J. Chen, X. Wei, B. Liu, Y. Kuang, *Electrochim. Acta* 53 (2007) 777–784.
- [12] N. Li, Q. Xu, M. Zhou, W. Xia, X. Chen, M. Bron, W. Schuhmann, M. Muhler, *Electrochem. Commun.* 12 (2010) 939–943.
- [13] H.A. Gasteiger, S.S. Kocha, B. Sompalli, F.T. Wagner, *Appl. Cat.* 56 (2005) 9–35.
- [14] D.Z. Mezalira, M. Bron, *J. Power Sourc.* 231 (2013) 113–121.
- [15] A.B.A.A. Nassr, A. Quetschke, E. Koslowski, M. Bron, *Electrochim. Acta* 102 (2013) 202–211.
- [16] A.B.A.A. Nassr, I. Sinev, M.-M. Pohl, W. Grünert, M. Bron, *ACS Catal.* (2014) 2449–2462.
- [17] W. Li, J. Wen, M. Sennett, Z. Ren, *Chem. Phys. Lett.* 368 (2003) 299–306.
- [18] C.-M. Chen, M. Chen, F.-C. Leu, S.-Y. Hsu, S.-C. Wang, S.-C. Shi, C.-F. Chen, *Diamond Rel. Mater.* 13 (2004) 1182–1186.
- [19] Y. Wang, Z. Iqbal, S. Mitra, *J. Am. Chem. Soc.* 128 (2006) 95–99.
- [20] V. Datsyuk, M. Kalyva, K. Papagelis, J. Parthenios, D. Tasis, A. Siokou, I. Kallitsis, C. Galiotis, *Carbon* 46 (2008) 833–840.
- [21] S. Haydar, C. Moreno-Castilla, M. Ferro-García, F. Carrasco-Marín, J. Rivera-Utrilla, A. Perrard, J. Joly, *Carbon* 38 (2000) 1297–1308.
- [22] T.G. Ros, A.J. van Dillen, J.W. Geus, D.C. Koningsberger, *Chem. Eur. J.* 8 (2002) 1151–1162.
- [23] T. Aitchison, M. Ginic-Markovic, J. Matison, G. Simon, P. Fredericks, *J. Phys. Chem. C* 111 (2007) 2440–2446.
- [24] A.C. Ferrari, J. Robertson, *Phys. Rev. B* 61 (2000) 14095–14107.
- [25] H.M. Heise, R. Kuckuk, A. Srivastava, B.P. Asthana, *J. Raman Spectros.* 42 (2011) 294–303.
- [26] T. Schilling, M. Bron, *Electrochim. Acta* 53 (2008) 5379–5385.
- [27] Y.-R. Shin, I.-Y. Jeon, J.-B. Baek, *Carbon* 50 (2012) 1465–1476.
- [28] F.-H. Ko, C.-Y. Lee, C.-J. Ko, T.-C. Chu, *Carbon* 43 (2005) 727–733.
- [29] G. Cravotto, D. Garella, E.C. Gaudino, F. Turci, S. Bertarione, G. Agostini, F. Cesano, D. Scarano, *New J. Chem.* 35 (2011) 915–919.
- [30] N. Alexeyeva, K. Tammeveski, *Electrochem. Solid-State Lett.* 10 (2007) F18–F21.
- [31] S. Nijjer, J. Thonstad, G. Haarberg, *Electrochim. Acta* 46 (2000) 395–399.
- [32] O. Ornelas, J.M. Sieben, R. Ruiz-Rosas, E. Morallón, D. Cazorla-Amorós, J. Geng, N. Soin, E. Siores, B.F.G. Johnson, *Chem. Commun.* 50 (2014) 11343–11346.

- [33] I. Kruusenberg, N. Alexeyeva, K. Tammeveski, *Carbon* 47 (2009) 651–658.
- [34] C.E. Banks, A. Crossley, C. Salter, S.J. Wilkins, R.G. Compton, *Angew. Chem. Int. Ed.* 45 (2006) 2533–2537.
- [35] F.H. Lima, M.L. Calegari, E.A. Ticianelli, *J. Electroanal. Chem.* 590 (2006) 152–160.
- [36] I. Roche, E. Chaînet, M. Chatenet, J. Vondrák, *J. Phys. Chem. C* 111 (2007) 1434–1443.
- [37] Z. Wang, M.D. Shirley, S.T. Meikle, R.L. Whitby, S.V. Mikhalovsky, *Carbon* 47 (2009) 73–79.

## 8 SECM investigation of carbon nanotubes for the application in redox flow batteries

*The content of this part has been published as*

**A comparative study of functionalized high-purity carbon nanotubes towards the V(IV)/V(V) redox reaction using cyclic voltammetry and scanning electrochemical microscopy**

*Reproduced from M. Steimecke, S. Rümmler, N.-F. Schuhmacher, T. Lindenberg, M. Hartmann, M. Bron, Electroanalysis 2017, 29, 1056-1061 with permission of John Wiley and Sons, Copyright © 2017.*

**DOI: 10.1002/elan.201600614**

Abstract

Functionalized high purity carbon nanotubes (CNTs) with various amounts of oxygen containing surface groups were investigated towards the relevant redox reactions of the all-vanadium redox flow battery. The quinone/hydroquinone redox peaks between 0.0 and 0.7 V vs. Ag|AgCl|KCl<sub>sat.</sub> were used to quantifying the degree of functionalization and correlated to XPS results. Cyclic voltammetry in vanadyl sulfate-containing 3 M H<sub>2</sub>SO<sub>4</sub> as a common supporting electrolyte showed no influence of the amount of surface groups on the V(IV)/V(V) redox system. In contrast, the reactions occurring at the negative electrode (V(II)/V(III) and V(III)/V(IV)) are strongly affected by oxygen surface groups. However, under modified experimental conditions, SECM experiments detecting the consumption of VO<sup>2+</sup> molecules by CNT thin films in pH = 2 solution show improved *onset* potentials with increased surface oxygen content up to ~ 3 at%. The dissimilar results under different experimental conditions are rationalized by suggesting that oxygen functional groups do not form the active site for the V(IV)/V(V) reaction but wetting of the catalyst layer is of high importance.

## 8.1 Introduction

Carbon-based materials widely used as cheap electrode components in all-vanadium redox flow batteries (VRFB) were studied intensely over the last years to gain information about structural properties as well as the related electrocatalytic activity towards vanadium redox reactions. In most cases an improved catalytic activity towards the V(IV)/V(V) redox system, which is often considered as the more crucial of the two half-cell reactions, was found after carbon surface modification [1] including carbon nanotubes [2,3]. However controversial to these results, for CNTs it was also reported that functionalization does not lead to enhanced activity [4]. The mechanism of how the surface groups in graphite and the vanadium molecules at the respective electrode of the battery may interact was suggested some time ago [5,6] and was newly proposed for other materials, i.e. graphene [7]. Beside functionalization defects like edges in the graphite structure are reported to enhance the kinetics of both reactions [8].

Cyclic voltammetry (CV) as one of the most common electrochemical characterization technique is widely used for basic investigations of carbon materials to obtain information about their electrochemical properties and in particular activity. However, from literature as well as from the experience of our own lab it becomes obvious that the results from CV, i.e. peak position and peak separation of different catalysts, are not straightforward to study kinetics [9] or to identify and characterize changes within materials [10] even in case of vanadium redox reactions, which is mainly a result of the strong influence of porosity [11]. Beside porosity, CV results are demonstrated to be influenced by the surface oxygen content not only in terms of the studied redox reaction but also due to secondary effects like electrode wetting [10]. Punckt *et al.* studied the porosity of carbon films with different oxygen content using an electrochemical method and concluded that increased hydrophobicity affects the dispersion stability and in consequence the electrochemical results [12].

As an alternative to the common CV analysis, we recently proposed an advanced method of characterizing carbon materials towards the V(IV)/V(V) reaction using scanning electrochemical microscopy (SECM) [13]. In this method, an ultramicroelectrode (UME) is positioned in close distance to the catalyst film that is stepwise polarized to more positive potentials and thus consumes  $\text{VO}^{2+}$ . During continuous potential sweeps at the UME  $\text{VO}^{2+}$  species remaining in the gap between catalyst film and UME are detected. As a result, a curve showing consumption of  $\text{VO}^{2+}$  by the film can be derived and the *onset* potential as one of the important parameters can be obtained and compared for different materials.

In this work, the influence of surface oxygen functional groups (0.4 – 8.0 at%) in high-purity carbon nanotubes on the performance towards the V(IV)/V(V) redox system under different experimental conditions is studied using CV and SECM.

## 8.2 Experimental

### 8.2.1 Sample preparation

High-purity carbon nanotubes (Baytubes<sup>®</sup> C 150P) [14] were functionalized using a microwave oven and different oxidation reagents, such as nitric acid (NA), hydrogen peroxide (HP), mixtures of both (NAHP), mixture of nitric and sulfuric acid (NASA) and potassium permanganate solution (PP), respectively. Except for the NASA sample, the detailed preparation procedures can be found in a previous work [15]. The NASA sample was prepared analogously to the other samples using a mixture containing 5.1 M nitric and 9 M sulfuric acid applied for one hour of continuous microwave heating (800 W) and the same washing and drying procedures as described previously. Before functionalization, the starting material was even pretreated at 800 °C in Ar atmosphere (CNT-800).

### 8.2.2 X-ray photoelectron spectroscopy (XPS)

For X-ray photoelectron spectroscopy an Omicron DAR 400 X-ray source with Al K $\alpha$  line (15 kV) and an EA 125X Hemispherical Energy Analyser (Omicron) were used. Overview scans were performed with a pass energy of 100 eV and detail scans of the O 1s region with 30 eV. Elemental compositions as well as bond characteristics were obtained by data evaluation using the Casa XPS software.

### 8.2.3 Electrochemical characterization (CV, SECM)

To investigate the samples in a thin film configuration with cyclic voltammetry a glassy carbon electrode (GC, 4 mm in diameter embedded in a PTFE cylinder) was employed as substrate. Prior to use, the bare electrode was cleaned with alumina paste (1.0 and 0.3  $\mu\text{m}$ ) and water on a polishing cloth until a mirror finish was obtained. For thin film electrode fabrication, an ink was prepared by mixing 10 mg of the respective sample and 2.5  $\mu\text{L}$  Nafion<sup>®</sup> 119 solution (5% in lower aliphatic alcohols, DuPont, USA) with 1 mL acetone (Roth GmbH, Germany). Afterwards, the sample was suspended in an ultrasonification bath for 2 h until a homogeneous ink was obtained. 10  $\mu\text{L}$  of the respective sample ink was drop coated onto the cleaned GC electrode resulting a loading of 51  $\mu\text{g cm}^{-2}$  and dried in air. Acetone was chosen since it proved a suitable solvent for fast and homogenous film formation. Cyclic voltammetry (CV) of the carbon nanotube samples was performed with a Gamry potentiostat PGI4 and the Gamry Framework 2.67 software in a one compartment glass cell where the catalyst-coated GC

electrode was used as working electrode (WE), a Pt wire as counter (CE) and an Ag|AgCl|KCl<sub>sat.</sub> system as reference electrode (RE). All CV experiments were performed in a solution containing 0.1 M VOSO<sub>4</sub>/3 M H<sub>2</sub>SO<sub>4</sub> between -0.55 and 1.2 V vs. Ag|AgCl|KCl<sub>sat.</sub> with scan rates of 50 mV s<sup>-1</sup> as well as in 10 mM VOSO<sub>4</sub>/buffer solution between 0.0 and 1.2 V vs. Ag|AgCl|KCl<sub>sat.</sub>

SECM instrumentation, UME positioning, sample preparation and the experimental procedure were previously described [13]. Briefly, 10 mM VOSO<sub>4</sub> (Roth GmbH, Germany) were dissolved in a 0.5 M HSO<sub>4</sub><sup>-</sup>/SO<sub>4</sub><sup>2-</sup> buffer solution (1:1 molar mixture of the potassium salt solutions creating a pH of ~2). As substrate material ITO on quartz glass (indium-doped tin oxide, 2x2 cm, pgo GmbH, Iserlohn, Germany) was cleaned with acetone, ethanol and water in an ultrasonification bath for several minutes and dried in air. For the preparation of all sample spots on the ITO electrode 0.4 μL of the catalyst ink (see above) was pipetted using an HPLC syringe pump into a perforated tape (Tesa<sup>®</sup> with a stamped hole of ~500 μm in diameter) which was glued onto the ITO electrode before. After drying the tape was carefully removed. For SECM experiments, a 25 μm Pt ultramicroelectrode (UME, RG=10, Sensolytics GmbH, Bochum, Germany) was used as working (UME), the respective catalyst spot on the ITO electrode as second working (WE), a miniaturized Ag|AgCl|KCl<sub>sat.</sub> (Metrohm, B. V., Netherlands) as reference and a coiled Pt wire as counter electrode. The positioning of the UME was realized by lowering it to touch the ITO surface next to the spot and then lifting up for 20 μm and manually positioning above the spot using an optical microscope. Linear sweep voltammetric (LSV) experiments at the UME were performed between 0.8 and 1.4 V vs. Ag|AgCl|KCl<sub>sat.</sub> with 200 mV s<sup>-1</sup> after a 5 s quiet time while discrete potentials were applied to the catalyst spots at the ITO electrode and modulated in positive potential direction with 10 mV step<sup>-1</sup> (staircase voltammetry). A LSV scan is performed at each individual potential applied to the ITO electrode and the UME current value at 1.4 V is used to create the consumption curve. To create a reproducible UME response 75 – 100 LSV scans were carried out before the respective experiment started. Again a quiet time of 5 s was applied before each LSV. In all experiments solutions were handled in air and prepared with MilliQ water (< 0.055 μS cm<sup>-1</sup>). Experiments were carried out at room temperature.



### 8.3 Results and discussion

XPS analysis of carbon nanotubes functionalized with different oxidation agents showed the incorporation of oxygen containing functional groups, such as alcohol, keton, carboxylic acid and ester groups ranging from 0.4 at% in the starting material (CNT-800) up to 8.0 at% oxygen in the nitric acid/sulfuric acid treated sample (NASA). The details of the oxidative treatment procedures as well as further morphological and electrochemical characterization can be found in the reference [15]. XPS results of all samples are summarized in Table 1.

Table 1. Sample names and surface atomic composition derived from XPS for characteristic binding energies of O1s (532 eV) (columns 2 and 3) and the contributing functional groups of the O 1 s region (col. 4 and 5), except for the NASA sample all data is taken from reference [15] and even discussed there more in detail.

sample	O1s (at%)	C–O [a]	C=O [b]
CNT_800 [c]	0.4	–	0.4
HP_10	1.6	1.1	0.5
NA_5	3.2	1.2	2.0
NA_10	4.2	1.6	2.6
NAHP_10	4.1	1.4	2.7
PP_02	6.7	1.9	4.8
NASA	8.0	3.9	4.1

[a] 532.8–533.8 eV, [b] 531.5–532.5 eV, [c] This sample was used as starting material for the preparation of all other samples.

Figure 1a displays cyclic voltammograms of all samples in 0.1 M VOSO<sub>4</sub>/3 M H<sub>2</sub>SO<sub>4</sub>. Between 0.0 V and 0.7 V samples with higher oxygen content (i.e. NASA, PP\_02) show broad, ill-defined redox peaks which are attributed to a pseudocapacity caused by quinone-type functional groups [16]. These features get less pronounced with decreasing oxygen content until they vanish in the HP\_10 and CNT\_800 samples, which is in accordance to prior CV measurements of the same samples in 0.1 M HClO<sub>4</sub> [15]. This quinone-type redox peak is a good measure of the degree of functionalization and may be used for quantification as displayed in Figure 1b, black squares. Here, a correlation between the amount of surface functional groups found by XPS and the transferred charge is clearly visible.

In CV (Figure 1a), at more positive potentials the V(IV)/V(V) redox pair between 0.7 and 1.1 V vs. Ag|AgCl|KCl<sub>sat.</sub> can be found. Current maxima of the oxidation peak are located between 0.95 and 0.99 V as well as between 0.83 and 0.88 V for the reduction peak, with the detailed peak positions summarized in Table 2. There is obviously no dependence on the amount of oxygen functional groups. The same holds true for peak currents, and it is assumed that these slight changes are rather an effect of different film quality. In contrast to these results on CNTs,

prior studies on electrodes made from pyrolytic graphite showed that quinone-type pseudocapacity decreases when V(IV)/V(V) redox reaction appears [17]. However, the positive impact on the V(IV)/V(V) redox pair as previously described for functionalized multi-walled CNTs [3] cannot be verified. These differences may be attributed to the quality of the used CNT material [18]. Friedl *et al.* [4] studied high-purity CNTs using impedance spectroscopy without finding any positive impact.

From the above results one may get the impression that it is rather straightforward to investigate carbon materials towards the V(IV)/V(V) redox pair using CV. However, as there is an overlap between quinone-type redox peaks and the V(IV)/V(V) redox pair, the determination of further kinetic data (e.g., *onset* potentials, Tafel slopes) is impeded. Furthermore, it has been claimed that peak separation in CVs is a poor indicator to conclude on reversibility of a system in the particular case of redox reactions at porous electrodes [11].

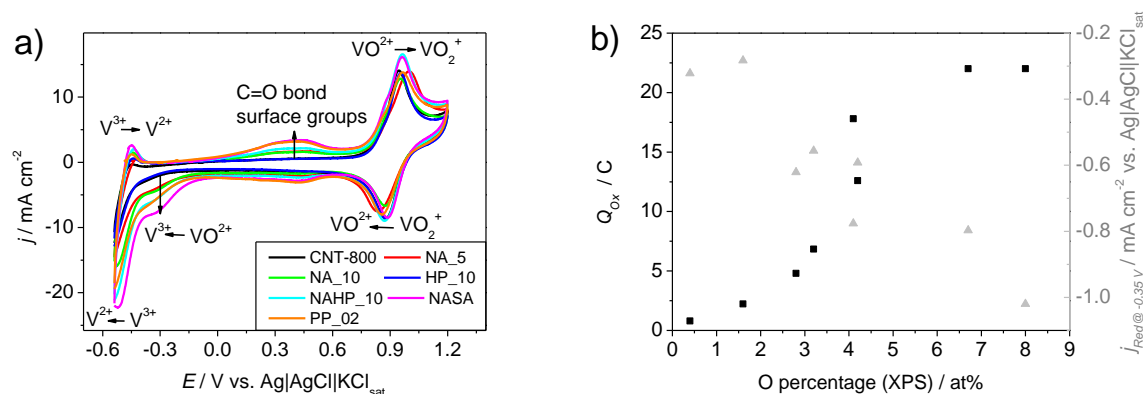


Fig. 1. Cyclic voltammograms of all functionalized carbon nanotube samples in 0.1 M  $\text{VOSO}_4/3 \text{ M H}_2\text{SO}_4$ , scan rate:  $50 \text{ mV s}^{-1}$ , with an assignment of all observed features (a) and the transferred charge  $Q$  (black squares) derived from the integrated area of the positive going sweep of the CV between 0.0 and 0.66 V vs.  $\text{Ag|AgCl|KCl}_{\text{sat}}$ , as well as the maximum current densities at -0.35 V in the negative going sweep (grey triangles) plotted against the surface concentration of oxygen found in the XPS analysis (b).

Anyhow, although quantitative data may not be obtained, a qualitative investigation of changes introduced by functionalization seems to be still possible. Going to potentials negative of the quinone-hydroquinone pairs in Figure 1a, a strong influence of the surface oxygen content on the V(IV) to V(III) reduction between -0.1 and -0.4 V  $\text{Ag|AgCl|KCl}_{\text{sat}}$  can be found. The reduction current is clearly enhanced with increasing oxygen content. This reduction peak is followed by the reduction of V(III) to V(II) at potentials  $< -0.4 \text{ V}$  that is in the same way enhanced by oxygen containing surface groups as the previous reduction peak. This enhancement has been attributed to the presence of phenolic groups [6] in graphite or to carboxylic groups as in graphene material [7]. We excluded that the enhancement in V(III) to

V(II) reduction is an effect of enhanced availability of V(III) by repeating the measurements in 0.1 M V(III)/V(IV) solution, which resulted in identical CVs (not displayed). Plotting the maximum current density at -0.35 V against the surface oxygen amount a clear correlation can be found (Figure 1b, grey triangles). At even more negative potentials in the CV (not displayed), hydrogen evolution can be observed, which is suppressed with increasing oxygen content, probably due to a competition between V(III) reduction and hydrogen evolution.

Table 2. Peak potentials of the oxidation ( $E_{ox}$ ) and reduction ( $E_{red}$ ) from CV measurement in Figure 1a in 0.1 M  $\text{VOSO}_4/3 \text{ M H}_2\text{SO}_4$  (columns 2 and 3), *onset* potentials as well as kinetic parameter derived from LSV-SECM analysis of all samples in 0.5 M  $\text{HSO}_4^-/\text{SO}_4^{2-}$  buffer solution (columns 4 and 5), all potentials are referred to a  $\text{Ag}|\text{AgCl}|\text{KCl}_{\text{sat}}$  reference electrode.

sample	$E_{ox}/\text{V}$	$E_{red}/\text{V}$	$E_{onset}/\text{V}$	$k / \text{mV dec}^{-1}$
HG3 [a]	0.98	0.9	0.91	120
CNT_800	0.95	0.88	0.79	187
HP_10	0.96	0.88	0.66	158
NA_5	0.99	0.83	0.61	99
NA_10	0.96	0.88	0.6	94
NAHP_10	0.96	0.87	0.6	89
PP_02	0.96	0.86	0.59	79
NASA	0.96	0.88	0.58	96

[a] Data is taken from the reference [13].

As already stated, cyclic voltammetry seems not to be a suitable method for a quantitative characterization of carbon materials towards the V(IV)/V(V) redox reaction. In diluted solution (10 mM  $\text{VO}^{2+}$ ) this is even more the case because capacitive currents from the double layer are relatively stronger compare to the Faradaic ones (Figure 2a). Reducing the CV scan rate attenuates this disadvantage but may enhance uncertainties due to diffusion in porous structures. Thus, the linear sweep voltammetric procedure applied to scanning electrochemical microscopy (LSV-SECM) is used to characterize the samples in more detail by creating a consumption curve of  $\text{VO}^{2+}$  in an indirect way using an ultramicroelectrode providing the *onset* potential and an additional kinetic parameter.

Cyclic voltammograms of selected samples, namely CNT-800 (0.4 at% O) and PP\_02 (6.7 at% O) are displayed in Figure 2a and compared to the results of a carbon material of different nature, (HG3, a graphitic mesoporous carbon [19]). It is obvious that based on CV analysis (Figure 2a, grey background) it is almost impossible to compare the different materials because of the significant differences in background currents originating from different double layer

charging, quinone-type surface groups and the electrochemically available surface. Even the comparison of the two modified CNTs appears to be difficult. However, applying LSV-SECM, a clear differentiation of the materials is possible. The resulting consumption curves (Figure 2a) allow to characterize and to compare the very different materials.

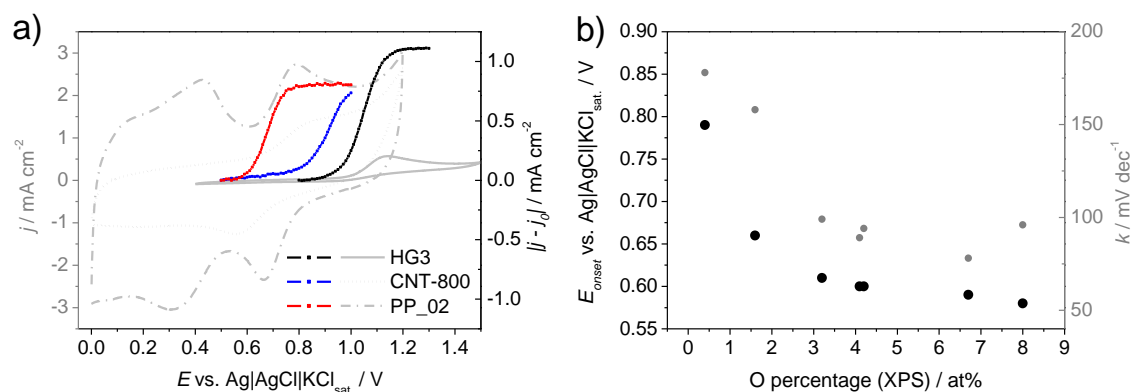


Fig. 2. Cyclic voltammograms of HG3, CNT-800 and PP\_02 carbon samples (grey) in 0.5 M  $\text{HSO}_4^-/\text{SO}_4^{2-}$  buffer solution, scan rate  $50 \text{ mV s}^{-1}$  and the normalized current densities derived from LSV-SECM measurements in the same solution,  $25 \mu\text{m}$  Pt UME,  $10 \text{ mV step}^{-1}$  (a) and the *onset* potential (black circles) and kinetic parameter (grey triangles) plotted against the oxygen content derived from XPS (b), data of the HG3 sample is taken from the reference [13].

As already reported [13], the HG3 sample (from CV analysis the V(IV)/V(V) redox peak potentials,  $E_{\text{ox}} = 0.98 \text{ V}$  and  $E_{\text{red}} = 0.90 \text{ V}$  vs.  $\text{Ag|AgCl|KCl}_{\text{sat}}$ , in  $0.1 \text{ M VO}_2\text{SO}_4/3 \text{ M H}_2\text{SO}_4$  are quiet similar to the CNT samples, cf. Table 2) showed inferior properties at higher pH with a positive shift in oxidation peak potential and the disappearance of the reduction peak. The *onset* potential of the conversion of V(IV) was found at  $0.91 \text{ V}$  and a kinetic parameter of  $120 \text{ mV dec}^{-1}$  (from the slope of the linear part of the logarithmic plot of the respective curves in Figure 2a) could be determined. The non-treated CNT sample (CNT-800) showed an improved *onset* potential at  $0.79 \text{ V}$  but a decreased kinetic parameter ( $187 \text{ mV dec}^{-1}$ ). The best performance among all functionalized CNT samples can be found for the NASA sample. Here, the *onset* potential ( $0.58 \text{ V}$ ) as well as the kinetic parameter ( $96 \text{ mV dec}^{-1}$ ) have drastically improved. However, as displayed in Figure 2b, the most significant change in both values can be found by increasing the surface oxygen content from ca. 0.4 to ca. 3.2 at% followed by a moderate improvement of the *onset* potential ( $\sim 30 \text{ mV}$ ) between 3.2 and 8.0 at% O. In the same region the kinetic parameter seems to be more or less constant.

Obviously only a certain amount of oxygen is necessary to improve the  $\text{VO}^{2+}$  conversion in this experimental setup. This leads to the conclusion that oxygen surface functional groups are not the active sites in this case and other influences might be at work here. It was reported, that the

stability of a colloidal suspension of CNTs is an easy way to prove oxygen functionalization where in most cases 3 – 5 at% O are necessary to achieve stability in polar solvents [20]. In this regard, we suggest that the wetting of the sample and connected to it the electrochemically available surface area, which is enhanced by introducing polar surface groups seems to be of high importance for the electrochemical activity in the V(IV)/V(V) system as recently described for carbon paper [10]. Thus, a connection between available surface functional groups and the activity towards V(IV) oxidation cannot be found when a certain amount (~ 3 at% in our case) of functional groups is already present. The missing dependency on the degree of oxygen functionalization for CV analysis in 0.1 M VOSO<sub>4</sub>/3 M H<sub>2</sub>SO<sub>4</sub> (Figure 1a) might thus be a consequence of a better wetting behavior in this strong acid compared to a pH = 2 buffer solution.

## 8.4 Conclusion

Cyclic voltammetry and scanning electrochemical microscopy were used to characterize high-purity carbon nanotubes with different amounts of surface oxygen groups (0.4 to 8.0 at%) and no positive effect on the V(IV)/V(V) redox behavior could be found. CVs in strong acid solution as a common electrolyte in VRFB showed slight differences resulting from the film quality of the prepared thin film electrodes. Under modified experimental conditions, the LSV-SECM method that was applied to analyze the V(IV)/V(V) conversion at higher pH level (pH 2) resulted in a strong shift of the *onset* potential (180 mV), but only until a certain limit was reached (~3.2 at% surface oxygen). Further increase up to 8.0 at% results in minor improvement (30 mV). We assume that a certain amount of oxygen is necessary to render the carbon surface electrochemically available which might result from improved wetting and which may not be necessary in strong acid solution. Thus, as a general conclusion for the V(IV)/V(V) conversion the positive influence of oxygen functional groups is rather an effect of improved wetting and those groups do not form the active sites.

On the other hand, a significant impact on the V(IV) to V(III) and the V(III) to V(II) reduction with increased surface oxygen could be found. It thus might be favorable to use highly functionalized CNTs in the negative half cell of VRFBs; also for removing V(IV) ions from cross contamination. In general, it can be concluded that both half cell reactions in VRFB respond differently to oxygen functionalization, which should be taken into account for future studies.

## 8.5 References

- [1] a) L. Yue, W. Li, F. Sun, L. Zhao, L. Xing, *Carbon* **2010**, *48*, 3079–3090; b) W. Zhang, J. Xi, Z. Li, H. Zhou, L. Liu, Z. Wu, X. Qiu, *Electrochim. Acta* **2013**, *89*, 429–435.
- [2] Z. González, P. Álvarez, C. Blanco, S. Vega-Díaz, F. Tristán-López, L. P. Rajukumar, R. Cruz-Silva, A. L. Elías, M. Terrones, R. Menéndez, *Sus. Ener. Tech. Assess.* **2015**, *9*, 105–110.
- [3] W. Li, J. Liu, C. Yan, *Carbon* **2011**, *49*, 3463–3470.
- [4] J. Friedl, C. M. Bauer, A. Rinaldi, U. Stimming, *Carbon* **2013**, *63*, 228–239.
- [5] B. Sun, M. Skyllas-Kazacos, *Electrochim. Acta* **1992**, *37*, 1253–1260.
- [6] B. Sun, M. Skyllas-Kazacos, *Electrochim. Acta* **1992**, *37*, 2459–2465.
- [7] M. Park, I.-Y. Jeon, J. Ryu, J.-B. Baek, J. Cho, *Adv. Energy Mater.* **2015**, *5*, 1401550.
- [8] N. Pour, D. G. Kwabi, T. Carney, R. M. Darling, M. L. Perry, Y. Shao-Horn, *J. Phys. Chem. C* **2015**, *119*, 5311–5318.
- [9] I. Streeter, G. G. Wildgoose, L. Shao, R. G. Compton, *Sens. Act. B* **2008**, *133*, 462–466.
- [10] M.-A. Goulet, M. Skyllas-Kazacos, E. Kjeang, *Carbon* **2016**, *101*, 390–398.
- [11] C. Punckt, M. A. Pope, I. A. Aksay, *J. Phys. Chem. C* **2013**, *117*, 16076–16086.
- [12] C. Punckt, M. A. Pope, J. Liu, Y. Lin, I. A. Aksay, *Electroanalysis* **2010**, *22*, 2834–2841.
- [13] M. Steimecke, S. Rümmler, M. Kühhirt, M. Bron, *ChemElectroChem* **2016**, *3*, 318–322.
- [14] M. Bierdel, S. Buchholz, V. Michele, L. Mleczko, R. Rudolf, M. Voetz, A. Wolf, *Phys. Stat. Sol. (B)* **2007**, *244*, 3939–3943.
- [15] M. Steimecke, S. Rümmler, M. Bron, *Electrochim. Acta* **2015**, *163*, 1–8.
- [16] a) N. Alexeyeva, K. Tammeveski, *Electrochem. Solid-State Lett.* **2007**, *10*, F18–F21; b) R. L. McCreery in *Electroanalytical chemistry. A series of advances* (Ed.: A. J. Bard), M. Dekker, New York, **1991**.
- [17] M. Gattrell, J. Qian, C. Stewart, P. Graham, B. MacDougall, *Electrochim. Acta* **2005**, *51*, 395–407.
- [18] M. Pumera, *Chem. Eur. J.* **2009**, *15*, 4970–4978.
- [19] Heraeus Quarzglas GmbH & Co. KG, Germany, *Porocarb® HG3 Graphitic Porous Carbon for Electrochemistry Applications*, **2013**.
- [20] a) F. Avilés, J. Cauich-Rodríguez, L. Moo-Tah, A. May-Pat, R. Vargas-Coronado, *Carbon* **2009**, *47*, 2970–2975; b) V. Datsyuk, M. Kalyva, K. Papagelis, J. Parthenios, D. Tasis, A. Siokou, I. Kallitsis, C. Galiotis, *Carbon* **2008**, *46*, 833–840.